Impacts of High-Depth of Wind Power Penetration on Interconnected Power Systems Dynamics

by

Ahmed Mostafa Mohammed Mohammed

A thesis submitted in conformity with the requirements
for the degree of Doctor of Philosophy
Graduate Department of Electrical and Computer Engineering
University of Toronto

Abstract

Impacts of High-Depth of Wind Power Penetration on Interconnected Power Systems Dynamics

Ahmed Mostafa Mohammed Mohammed
Doctor of Philosophy
Graduate Department of Electrical and Computer Engineering
University of Toronto
2016

The main objective of this work is to investigate the impact of the high-depth, e.g., 35%, of penetration of the wind power, as Wind Power Plants (WPPs), on the low-frequency (0.1-2Hz) dynamics of interconnected power systems. Due to the lack and/or inadequacy of the analytical and the digital time-domain simulation tools for this class of studies, this undertaking

1. Develops enhanced nonlinear dynamic models of Type-3[1] and Type-4[2] WPPs for transient stability studies.

2. Develops a MATLAB-based transient stability time-domain simulation tool and integrates the WPP models in the tool.

3. Develops small-signal (linearized) models of Type-3 and Type-4 WPPs from their corresponding enhanced nonlinear models.

4. Develops a MATLAB-based linear platform for eigen analysis of large power systems including linearized models of Type-3 and Type-4 WPPs.

5. Introduces and develops a measurement-based coherency identification method for power system coherency identification in the presence of WPPs.

[1]Type-3 WPPs refers to WPPs with doubly-fed asynchronous generators wind turbine generator units.

[2]Type-4 WPPs refers to WPPs with full-converter interfaced wind turbine generator units.

Based on the develops of items 1-5 above, this thesis investigates the impacts of the (i) depth of wind power penetration, (ii) locations of WPPs and (iii) types of WPPs on transient stability, damping ratios of electromechanical modes and coherency phenomena of the New York/New England power system. The studies conclude that:

i. Addition of WPPs do not introduce new inter-area oscillatory modes however it can affect existing ones.

ii. Impact of WPPs on the damping ratio of an inter-area mode is determined based on the location(s) of the added WPP(s) with respect to the areas. If the WPPs increase the power exchange between two areas, the damping of the inter-area mode decreases.

iii. Addition of WPPs close to synchronous generators equipped with DC exciters results in the reduction of the damping ratio of the corresponding local modes due to interactions among the fast reactive power controllers of the WPPs and the slow excitation systems of the generators.

iv. As the depth of penetration of wind power increases, the power system exhibits higher degree of nonlinearity and the impact of wind power on the system transient stability can be determined only from the time-domain simulation of the system nonlinear model. This indicates that the results of the transient stability assessment of the power system for lower depth of penetration of wind power cannot be extrapolated to higher levels.

v. Addition of WPPs to a power system results in altering the coherency structure. Based on the WPPs allocation patterns, the impact of wind power on the system coherency is limited to the formation of new areas that are totally dominated by the added WPPs and the base case coherency structure of the synchronous generators is preserved.

To my dear mother, and my late father

To Amal, Mariam and Zaineldeen who always lighten up my life and bring joy in it

Acknowledgments

I would like to express my sincere gratitude to my supervisor, Professor Reza Iravani, for his invaluable supervision, encouragement, and financial support throughout my Ph.D.studies. The experience of having him as my supervisor, specially on the personal level, has enriched my vision regarding the different aspects of life and research. Throughout the course of my Ph.D., I have learned a lot from him through our numerous discussions and weekly meetings. His door is always open. I will always be grateful for his continuous patience and support on both the academic and the personal levels and will always remain honored that I have worked under his supervision.

I would like also to thank the Ph.D. examination committee: Professor Peter Lehn, Professor Zeb Tate, Professor Josh Taylor, and Professor Bala Venkatesh for their review of the thesis and their constructive comments.

Special and cordial thanks go to my dear mother who supported me in ways no one ever could have provided. The least I can do is to dedicate this work to her. I would like to express my gratitude to my wife Amal whom without her support and unconditioned dedication, the completion of this thesis would not be a reality.

Finally, I would like to acknowledge the financial support of the Department of Electrical and Computer Engineering at the University of Toronto.

Contents

1 Introduction **1**

1.1 Statement of the Problem 1

1.2 Wind Power Plant Models 3

1.3 Coherency Identification 5

1.4 Impacts on Low-Frequency Dynamics 6

1.5 Methodology 7

1.6 Thesis Layout 7

2 Study System **9**

2.1 Introduction 9

2.2 Study System Description 9

2.3 Nonlinear Dynamic Model (Transient Stability Model) 10

2.3.1 Synchronous Machine Model 11

2.3.2 Excitation Systems Models 12

2.3.3 Power System Stabilizer Model 13

2.3.4 AC Network Model 14

2.4 Implementation and Validation of the Benchmark System Non-Linear Model in MATLAB/Simulink 15

2.5 Small-Signal Dynamical Stability Analysis of the Benchmark System . . 16

2.5.1 Model Development 16

2.5.2 Eigenstructure and Oscillatory Modes of System-1 18

2.6 Wind Power in System-1 19

2.6.1 Depth of Wind Power Penetration 20

2.6.2 WPP Locations 20

2.6.3 Study Cases 21

2.7 Conclusions 24

3 Wind Power Plant Models **26**
3.1 Introduction . . . 26
3.2 Enhanced Type-3 WPP Model . . . 27
3.2.1 WT3G2 - Generator/Converter Model . . . 27
3.2.2 WT3E1 - Converter Control Model . . . 30
3.2.3 WT3T1 - Wind Turbine-Generator Mechanical Model . . . 33
3.2.4 WT3P1 - Pitch Angle Control Model . . . 33
3.3 Enhanced Type-4 WPP Model . . . 35
3.3.1 WT4G1 - Generator/Converter Model . . . 35
3.3.2 WT4E1 - Converter Control Model . . . 36
3.4 WPP Linearized Models . . . 37
3.4.1 Operating Point Determination for Type-3 WPP Model . . . 39
3.4.2 Type-3 WPP Small-Signal Dynamic (Linearized) Model . . . 40
3.4.3 Type-4 WPP Small-Signal Dynamic (Linearized) Model . . . 42
3.5 Conclusions . . . 42

4 Wind Power Plant Model Validation **44**
4.1 Introduction . . . 44
4.2 Large-Signal Dynamics - Type-3 WPP . . . 45
4.2.1 Fault close to the WPP terminal . . . 45
4.2.2 Fault at a remote bus . . . 45
4.3 Comparisons with Other Type-3 WPP Models . . . 47
4.3.1 Comparison with Type-3-H . . . 47
4.3.2 Comparison with Type-3-PSSE2 . . . 49
4.4 Large-Signal Dynamics Type-4 WPP . . . 49
4.4.1 Developed Enhanced Model Validation . . . 51
4.4.2 Comparison with Type-4-PSSE2 . . . 53
4.5 Linearized Model Validation . . . 55
4.5.1 Type-3 WPP linearized model validation . . . 56
4.5.2 Type-4 WPP linearized model . . . 57
4.6 Conclusions . . . 58

5 Impacts of Wind Power on Power System Low-Frequency Dynamics **60**
5.1 Introduction . . . 60
5.2 Wind Power Impacts on Oscillatory Modes . . . 61
5.2.1 Control Modes . . . 62
5.2.2 Local Plant Modes . . . 65

5.2.3 Inter-area Modes . . . 66
5.3 New Oscillatory Modes . . . 69
5.3.1 Type-3 Modes . . . 70
5.3.2 Common Modes . . . 70
5.3.3 Mutual Modes . . . 70
5.4 Wind Power Impacts on Nonlinear Time-Response . . . 71
5.4.1 Base Case Nonlinear Time-Response . . . 71
5.4.2 Nonlinear Time-Response Corresponding to Wind Power Levels . . . 72
5.5 Conclusions . . . 75

6 Impacts of Wind Power on Power System Coherency 77
6.1 Introduction . . . 77
6.2 Dynamic Coherency Determination (DCD) Method . . . 78
6.2.1 Identification of Coherent Generators . . . 80
6.2.2 Association of Non-generator Buses . . . 83
6.3 DCD Method Study Results for the Base Case Conditions . . . 83
6.3.1 Case I - Fault at Bus-27 . . . 84
6.3.2 Case II - Fault at Bus-33 . . . 84
6.3.3 Case III - Fault at Bus-53 . . . 87
6.4 Wind Power Impacts on System Coherency . . . 89
6.4.1 Fault at Bus-25 . . . 89
6.4.2 Fault at Bus-56 . . . 94
6.4.3 Fault at Bus-39 . . . 95
6.5 Conclusions . . . 99

7 Conclusions, Contributions and Future Work 100
7.1 Thesis Summary . . . 100
7.2 Conclusions . . . 101
7.3 Original Contributions . . . 103
7.4 Future Work . . . 103

A Non-zero Elements of the Linearized Model of Type-3 WPP 104

B Type-3 and Type-4 WPPs Enhanced Equivalent Models Data 105

C System-2 Data 107

D Comparisons of the DCD Method with Other Coherency Determination Methods **108**

D.1 Comparison with the Slow-Coherency Method 108

D.2 Comparison with Measurements-Based Methods 109

D.3 Performance under Noise 110

Bibliography **112**

List of Tables

2.1 Oscillatory Modes of System-1 (Base Case) 19
2.2 Study cases for 5% WPPL 23
2.3 Study cases for 15% WPPL 23
2.4 Study cases for 30% WPPL 24

3.1 Truth Table for the Discrete Blocking Signals y_p and y_c 34
3.2 Initial Values of Type-3 WPP Model Variables 40

5.1 Most affected local plant modes for different WPPLs 66
5.2 Damping ratio of mode 24 for study cases proposed in Chapter 2 68
5.3 Damping ratios of mode 24 and mode 26 for the modified study cases . . 69
5.4 Transient stability assessment for fault at Bus-26 with 30% WPPL 73

6.1 Coherent groups and the associated buses (Case I) 84
6.2 Coherent groups and areas (Case II) 86
6.3 Coherent groups and areas (Case III) 88
6.4 Coherency Coefficients of the separated non-generator buses (Case III) . 88

B.1 Type-3-E Generator/Converter Data 105
B.2 Type-3-E Pitch Angle Control Data 105
B.3 Type-3-E Converter Control Data 105
B.4 Type-3-E Generated Active power – Reference Speed Piece-Wise Linear Characteristics ($f(P_{gen})$) 106
B.5 Type-3-E Wind Turbine Data 106
B.6 Type-4-E Generator/Converter Data 106
B.7 Type-4-E Converter Control Data 106

C.1 System-2 Bus Data 107
C.2 System-2 Line Data 107
C.3 Power Flow Data of Type-3 and Type-4 WTG units 107

D.1 Coherent groups and areas (Slow-Coherency method [1,2]) 109
D.2 Coherent groups and areas (method of [3]) 110
D.3 Coherent groups and areas (DCD method) 110

List of Figures

2.1 A schematic diagram of the New York Power System (NYPS) – New England Test System (NETS) – System-1 10
2.2 Block diagram for voltage-controlled current source representation of GEN 11
2.3 Block diagram of the PSS installed at GEN-9 14
2.4 System-1 time-response to a three-phase, 5-cycle fault at Bus-27 15
2.5 Projection of the detailed representation of the NPCC system on its geographical map 22
2.6 Schematic diagram of System-1 that identifies locations of WPPs 22

3.1 Type-3 WPP functional blocks 27
3.2 Type-3 WPP Generator/Converter Model 28
3.3 Type-3 WPP Converter Control Model—Active Power Control 30
3.4 Type-3 WPP Converter Control Model—Reactive Power Control 32
3.5 Type-3 WPP Wind Turbine Model 33
3.6 Type-3 WPP Pitch Angle Control Model 34
3.7 Type-3 WPP Blocking Logic Realization 34
3.8 Type-4 WPP functional blocks 35
3.9 Type-4 WPP Generator/Converter Model 36
3.10 Type-4 WPP Converter Control Model 38
3.11 Type-4 WPP Converter Current Limiter Logic 38
3.12 Generated Active Power - Reference Speed characteristics ($f(P_{gen})$) of Type-3 WPP 42

4.1 Type-3 WPP response to a fault close to the terminal bus for developed enhanced model (Type-3-E) and PSS/E platform built-in model (Type-3-PSSE1) 46
4.2 Type-3 WPP response to a fault at a remote bus for developed enhanced model (Type-3-E) and PSS/E platform built-in model (Type-3-PSSE1) . 48

4.3 Type-3 WPP response to a fault close to the terminal bus for developed enhanced model (Type-3-E) and WPP model presented in [4] (Type-3-H) 50
4.4 Type-3 WPP response to a fault at a remote bus for developed enhanced model (Type-3-E) and WPP model presented in [4] (Type-3-H) 51
4.5 Type-3 WPP response to a fault close to the terminal bus for developed enhanced model (Type-3-E) and PSS/E and WECC documented model (Type-3-PSSE2) 52
4.6 Type-4 WPP response to a fault close to the terminal bus for developed enhanced model (Type-4-E) and PSS/E platform built-in model (Type-4-PSSE1) 53
4.7 Type-4 WPP response to a fault at a remote bus for developed enhanced model (Type-4-E) and PSS/E platform built-in model (Type-4-PSSE1) . 54
4.8 Type-4 WPP response to a fault close to the terminal bus for developed enhanced model (Type-4-E) and PSS/E and WECC documented model (Type-4-PSSE2) 55
4.9 A schematic diagram of System-2 56
4.10 Type-3 WPP linearized model response 57
4.11 Type-4 WPP linearized model response 58

5.1 The eigenvalues corresponding to control modes 3 and 4 for different WPPLs and participation percentages of Type-3 WPPs 63
5.2 The eigenvalues corresponding to control modes 6 and 11 for different WPPLs and participation percentages of Type-3 WPPs 64
5.3 Impact of WPP type on the damping ratios of local plant modes 67
5.4 GEN-9 speed deviation for fault at Bus-26 for the base case 72
5.5 GEN-9 speed deviation for fault at Bus-26 corresponding to 100% Type-4 WPP (a) 5% WPPL and (b) 15% WPPL 73
5.6 GEN-9 speed deviation for fault at Bus-26 corresponding to 75% Type-4 WPP (a) CD pattern (Stable) and (b) UD pattern (Unstable) WPPL . . 74

6.1 Definition of related/unrelated frequency deviation vectors in terms of coherency 81
6.2 Simulated frequency deviation signals of the generator buses for case I . . 85
6.3 Areas corresponding to Case I 86
6.4 Areas corresponding to Case II 87
6.5 Areas corresponding to Case III 88
6.6 Coherency structure due to fault at Bus-25 for the base case 90

6.7 Coherency structure due to fault at Bus-25 for 5% WPPL case 91
6.8 Coherency structures due to fault at Bus-25 for 15% WPPL case 93
6.9 Coherency structure due to fault at Bus-56 for the base case 94
6.10 Coherency structures due to fault at Bus-56 for 5% WPPL case 96
6.11 Coherency structures due to fault at Bus-56 for 15% WPPL case 97
6.12 Coherency structures due to fault at Bus-39 different WPPLs cases . . . 98
6.13 Coherency structures due to fault at Bus-39 for the base case 98

Chapter 1

Introduction

1.1 Statement of the Problem

Environmental issues associated with the conventional power plants, volatility of the cost of energy and technical/economical feasibility of power electronic converters for power system applications have made wind power as an integral part of the power generation portfolio, almost globally [5, 6]. The wind power proliferation in the electric power grid is realized based on:

- Grid integration of small- to medium-size (up to 1500-kW) Wind Turbine-Generator (WTG) units or an aggregate of a few WTG units, at the power distribution-class voltage (up to 45-kV), and are treated as distributed generation units.

- Grid integration of an aggregate that includes a large number medium- to large-size (up to 8-MW) WTG units, at the transmission voltage level. Such an aggregate operates as a single, unified entity with respect to the host grid at the point of common coupling, and treated as a Wind Power Plant (WPP). The installed capacity of a WPP can be comparable or even more than those of the conventional thermal/hydro power plants, e.g., 1200-MW [7]. A WPP can be an on-shore or an off-shore WPP. The existing trend is towards development of off-shore WPPs with higher capacity. The focus of this thesis is on grid integration of wind power based on WPPs.

The distinguishing characteristic of a WPP as compared with that of a conventional power plant is its intermittency, i.e., the output power from a WPP is at the mercy of the wind. At low-depth of wind power penetration, i.e., 5%, the intermittency can be addressed by the power grid existing controls, i.e., Automatic Generation Control (AGC)

system. As the depth of penetration of wind power increases, the impact of the WPP on the control/operation/protection of the grid becomes more pronounced.

This thesis is concerned with the transient instability issues due to presence of WPPs. For the medium-depth of wind power penetration, i.e., 5%-15%, the impact of intermittency can be partially or largely mitigated by active participation of WPPs in the control of the host grid, i.e., each WPP or a selected group of WPPs contributes to [8]:

- voltage control,
- power system stabilization function,
- inertia function,
- reserve margin, and
- frequency control and restoration.

Beyond the wind power depth-of-penetration of 15%, i.e., at high-depth of penetration, the conventional power system controls and the existing operational strategies are unlikely to address the impact of WPPs on the grid dynamic behavior [9].

The global wind power installation in 2014 was 51-GW and the trend is expected to continue in the foreseeable future [5,6]. The forecast is that up to 2030, the depth of wind power penetration in many interconnected power systems will be much higher than 15% and more likely within 35-50%. This increase in the depth of wind power penetration is to (i) address the load increase, (ii) substitute the decommissioning of polluting power plants (coal-generation) and (iii) substitute conventional thermal plants which reach to the end of their life-expectancy. However, the core problems are that:

- The impacts of such a high-depth of wind power penetration on the steady-state power flow, transient stability (0.1-2 Hz) and the electromagnetic transients (up to about 50 kHz) phenomena of power systems have neither been fully understood nor comprehensively investigated.
- The required mathematical models of WPPs to conduct the required studies have been neither fully developed nor verified.

The purpose of this thesis is to address the above problems with respect to transient stability of the interconnected power systems. This thesis considers both Type-3 and Type-4 WPPs and:

- Develops a nonlinear, state-space model of the WPP for time-domain simulation of the transient stability. In contrast to the existing WPP models, the developed models can be implemented in a general purpose simulation platform, e.g., MATLAB/Simulink, and not restricted by the vendor-specific platform limitations, e.g., PSS/E software. The nonlinear model is used to extract the linearized (small-signal) dynamic model of the WPP for a systematic evaluation of the eigenstructure of a power system including multiple WPPs.

- Introduces and develops a measurement-based coherency identification technique to quantify the impact of WPPs on the formation of coherent areas.

- Investigates, based on the above models, the impacts of (i) the type of WPP, (ii) the depth of penetration of wind power and (iii) the pattern of the distribution of WPPs on the damping of low-frequency oscillations, stability of the modes and the coherency phenomena.

A brief overview of the above three items will follow.

1.2 Wind Power Plant Models

Reported WPP models in the technical literature [10] are divided into the detailed models and the equivalent generic (standard) models. The former [11–21] represents all components within each WPP based on their relatively detailed models. This result in a model with a frequency-bandwidth wider than the one required for transient stability studies and impose prohibitive computational burden when used for transient stability studies of realistic size power systems. The equivalent generic models [22–26] are (i) not vendor specific, (ii) intended only for transient stability studies, and (iii) represent Type-3 and Type-4 WPPs in the range of 0.1–2 Hz. The description of the generic models are mainly given in the (i) WECC related documents [22, 23, 27], (ii) PSS/E documents [28], and (iii) [4] which only addresses the Type-3 WPP. The outstanding issues of the generic models based on these three groups of documents are:

- They cannot replicate the dynamic responses of the PSS/E-software built-in generic models [27] which have been verified based on field measurements. The PSS/E-software built-in models can be used if all the analyses are based on time-domain simulations. However, the PSS/E-software does not provide any means to systematically evaluate the eigenstructure of a power system including multiple WPPs. In

addition, the PSS/E-software imposes restrictions for the implementation of user-defined controllers. Moreover, the systematic design and development of any control structure necessitates the availability of either nonlinear or linearized models that are representative of the WPPs in the required frequency range. The PSS/E software built-in models and the generic models reported in the technical literature do not provide a means for such systematic approaches.

- They do not address the hybrid nature of the generic models, i.e., considering both continuous-time states and logic-controlled discrete variables associated with the controllers limits. The notion of hybrid representation is not described in the WECC and the PSS/E-software documents although the signature of the discrete logics [27] is observable in the response of PSS/E-software built-in model (not discussed in the PSS/E related documents). Reference [4] addresses the hybrid characteristics of Type-3 WPP model and shows that the hybrid nature is responsible of the convergence of the system to a different steady-state other than the pre-disturbance one, even if the pre- and post-disturbance system parameters are the same. However, the model described in [4] lacks the representation of the generator/converter and the reactive power control path.

References [16, 29] provide a basis for the development of the small-signal (linearized) dynamic models of Type-3 and Type-4 WPPs from the detailed nonlinear models. However, this class of models does not represent the equivalent generic WPP models and not applicable to transient stability analysis. Reference [4] deduces a Type-3 WPP linearized model from the corresponding nonlinear generic model. However, it exhibits limitations due to:

i. neglecting the generator/converter model, which results in two zero eigenvalues and thus the eigenstructure is not a full representation of the system dynamics,

ii. not considering the reactive power control path, and

iii. lack of agreement between the results of the nonlinear generic model and the PSS/E-software built-in model.

Thus, accurate Type-3 and Type-4 WPP nonlinear equivalent models and their corresponding linearized ones are not available in the technical literature and this thesis aims to address this issue.

1.3 Coherency Identification

The dynamic response of a multi-machine, large, interconnected power system to a disturbance includes multiple electromechanical oscillatory modes, approximately in the frequency range of 0.1–2 Hz. The generators within an electrical area exhibit unison dynamic behavior, i.e., the frequencies and phase-angles of their inter-area oscillations are almost the same. Such units are referred to as coherent generators [30]. The technical literature reports two types of methods [31–36] for coherency identification, i.e., model-based and measurement-based methods. An extensive review of different coherency identification methods is presented in [37, 38].

- Model-based Methods: In this category the system eigenstructure, based on a linearized dynamic model of the system, is used for the identification.

- Measurement-based Methods: This category utilizes signals, e.g., generator speeds, for coherency identification. These signals are either measured or deduced from time-domain simulation of a nonlinear dynamic model of the system.

Identifying the impacts of high-depth of penetration of wind power on power system coherency requires an appropriate coherency identification method which should (i) be capable of considering the effect of added WPPs on the coherency phenomenon and (ii) account for the hybrid nature of the equivalent WPP models. However, the reported coherency identification methods (model-based and measurements-based) exhibit limitations/drawbacks when WPPs are considered. These limitations/drawbacks are:

- Model-based methods inherently cannot account for the hybrid nature of the WPPs generic models since they neglect (i) changes in the system operating conditions, (ii) changes in the system configuration, and (iii) discrete operational modes of subsystems, e.g., HVDC links and WPPs. Moreover, they assume that coherency is independent of (i) disturbance severity and (ii) details of the generator model [39]. Therefore, they neglect the electrical dynamics of the generators and consider linearized swing equation of synchronous generators to determine the coherent groups. Such approach cannot be extended to include WPPs in identifying the coherent groups.

- Measurement-based Methods largely overcome the above limitations of the model-based methods. They use the turbine speed deviation signals of the synchronous generators for coherency identification. Such signals, in case of WPPs, are not representative of the dynamical responses of the WPPs with respect to the host grid side, due to the fast action of the converters and their controllers.

Therefore the development of an appropriate coherency identification method is a precursor to the investigation of the impacts of high-depth of penetration of wind power on the system coherency. This thesis addresses this issue and to the best of our knowledge is the first study to investigate the impacts of wind power on power system coherency phenomena.

1.4 Impacts on Low-Frequency Dynamics

Although there have been studies on the identification of the impacts of high-depth of wind power penetration on the transient stability and low-frequency oscillatory modes of power systems, the results of such studies are not definite and in several cases contradictory. One group of studies, [40–45], claims that at high penetration levels of Type-3 WPPs, the damping ratios of the low-frequency oscillatory modes increase, thus improving the overall system small-signal dynamical stability. However, a second group of studies, [46–51], contradicts this conclusion and suggest that (i) increasing the penetration level of wind power affects the total system inertia and results in decreasing the system damping and (ii) instability may be experienced not at high penetration levels. Moreover, another set of studies [52–58] adopts a different view where the system response is dependent on the fault location, WPPs locations, and the operating conditions of the system. For example the analysis of sensitivity to inertia [57] demonstrates that the integration of Type-3 WPP has both favorable and negative impacts on small-signal dynamical stability. Such contradictory conclusions are the results of limitations of the specific scenarios of the conducted studies, i.e.,

i. Decreasing the capacity of the conventional power plants or eliminating them from the power system as wind power is integrated in the power system [40, 42, 44, 47, 52, 53].

ii. Neglecting the impact of load increase at the high penetrations of wind power. Reference [46] proposes that the increased wind penetration at heavy loading conditions has a de-stabilizing effect on the system.

iii. Random choice of WPP locations and lack of co-relation with the resource locations [59].

iv. Conducting the studies on relatively small power systems [40–43, 45, 47–49, 53, 54] that are not suitable/realistic for high-depth integration of wind power.

v. Identifying the impacts due to a single type of WPPs [43, 44, 46, 48, 52–54] and not considering the cases where different types of WPPs exist in the system. This overlooks the impacts due to interactions between WPP types at different participation percentages.

1.5 Methodology

To achieve the thesis objectives, the following methodology is employed:

- Selection of a benchmark system that (i) is representative of an actual system with the potential of wind power integration, (ii) spans over a wide geographical area and allows integration of multiple WPPs with different distribution patterns, and (iii) experiences low-frequency oscillatory modes in its base case and thus the impact of WPPs on the low-frequency dynamics can be identified.

- Analytical development of linearized state-space model for the benchmark system base case. This model can be extended to account for the added WPPs.

- Identification of the locations of the WPPs for the different proposed scenarios in agreement with the system potential of wind power integration.

- Implementation of the developed Type-3 and Type-4 WPPs nonlinear equivalent models in MATLAB/Simulink platform and validating their time-response against the corresponding built-in models of the PSS/E software.

- Analysis of the eigenstructure of the linearized system with the added WPPs to determine the impacts of high-depth penetration of wind power on the low frequency-oscillatory modes of the benchmark system.

- Performing non-linear time-domain simulations to quantitatively identify the impacts of high-depth penetration of wind power on the system transient stability and coherency phenomena.

1.6 Thesis Layout

The rest of the thesis is organized as follows:

- Chapter 2 (i) introduces the New York/New England power system as the selected benchmark system for wind power integration, (ii) develops a non-linear

time-domain simulation of the benchmark system in the MATLAB/Simulink platform and validates the results against the results obtained from the PSS/E software, and (iii) tabulates the scenarios that are used for WPP impact studies.

- Chapter 3 develops the enhanced, non-linear, equivalent models of Type-3 and Type-4 WPPs and extracts the linearized models of both WPP types. This chapter also addresses the multiple eigenstructures of the linearized model of Type-3 WPP.

- Chapter 4 validates the developed enhanced models of Type-3 and Type-4 WPPs against the field-verified built-in models of PSS/E software tool. This chapter also compares the time-responses of the developed models with all the documented versions of the generic models available in the technical literature. Finally, this chapter validates the extracted linear models of Type-3 and Type-4 WPPs against the time-response of their corresponding non-linear models when subjected to small-signal disturbances.

- Chapter 5 presents the impacts of high-depth of penetration of wind power on the low-frequency oscillatory modes and the nonlinear transient response of the benchmark system. These analyses are based on the study cases presented in Chapter 2 and the developed nonlinear and linearized WPP models in Chapter 3.

- Chapter 6 proposes new measurement-based method for the dynamic identification of coherent generators of the study system including WPPs. This chapter also investigates the impacts of high-depth of wind power penetration on system coherency using the developed method.

- Chapter 7 summarizes the conclusions of the thesis, highlights its main contributions, and provides future research directions.

Chapter 2

Study System

2.1 Introduction

This chapter introduces a study power system that is used in the subsequent chapters to investigate the impact of high-depth of penetration of wind power integration on the power system low-frequency dynamics, i.e., transient stability. This chapter also develops a dynamic model of the test system in the MATLAB/Simulink software platforms and verifies its accuracy by comparing its transient time-response with the corresponding waveforms that are obtained based on the system time-domain simulation in the PSS/E platform. The dynamic model is linearized about an operating point to deduce a small-signal dynamic (linear) model of the study system. The results from the dynamic nonlinear model and the linearized model of the study system are used as the base cases to quantify the impact of wind power integration on the transient behavior and eigenstructure of the study system in the subsequent chapters.

This chapter also presents a strategy to identify the locations of wind power plants and the depth of penetration of wind power in the study, and on that basis specifies the investigations and the corresponding test scenarios that are presented in the subsequent chapters.

2.2 Study System Description

Figure 2.1 shows a schematic diagram of the adopted study system and hereafter referred to as System-1. System-1 is a version of the New York Power System (NYPS) New England Test System (NETS) [60] and represents an equivalent of the Northeast Power Coordinating Council (NPCC) system also including Ontario, Michigan, Pennsylvania,

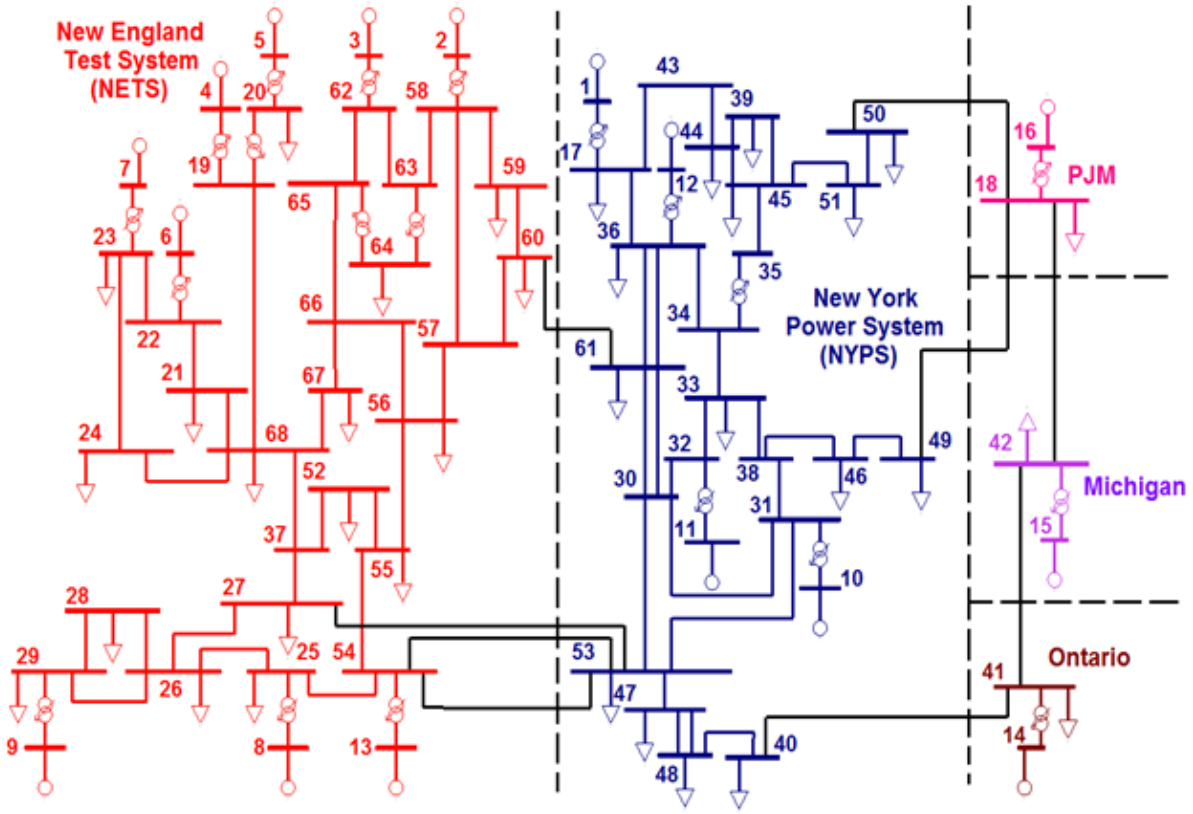

Figure 2.1: A schematic diagram of the New York Power System (NYPS) – New England Test System (NETS) – System-1

Maryland, and New Jersey power systems. System-1 includes 16 conventional power plants, 68 high-voltage buses, 66 transmission lines, and 35 loads. The power exchange between NETS and NYPS is 700 MW and NYPS imports 1500 MW from Pennsylvania, New Jersey and Maryland (PJM). The System-1 details and general data/parameters are given in [60]. The reasons for selection of System-1 as the test-bed for the investigation in this thesis are (i) it is a representation of a real, existing system, (ii) it provides realistic and extensive parameters and operational data, (iii) it exhibits well-understood and extensively investigated lightly-damped oscillatory modes, and (iv) it has realistic potential for large-scale on-shore and off-shore wind power integration.

2.3 Nonlinear Dynamic Model (Transient Stability Model)

This section describes models of the apparatus/components and the overall system of Figure 2.1 for the investigation of the system low-frequency dynamics.

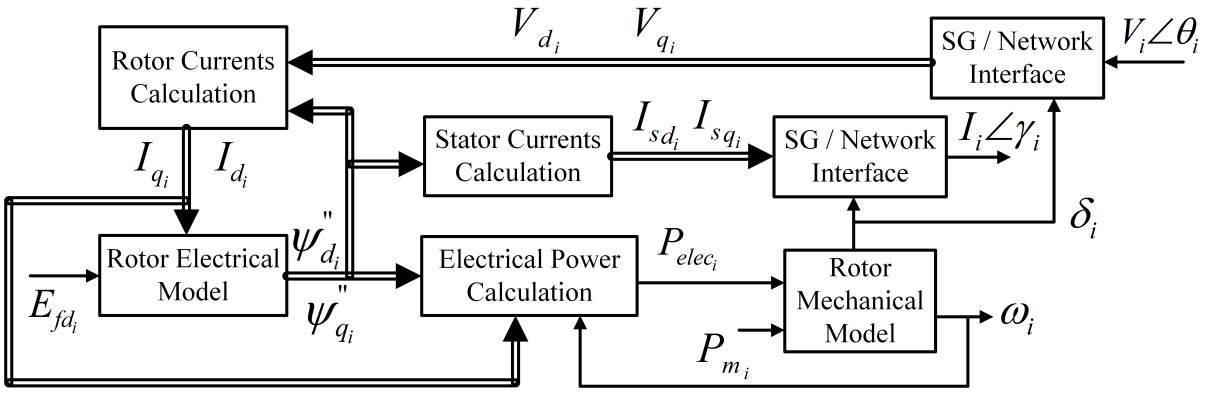

Figure 2.2: Block diagram for voltage-controlled current source representation of GEN

2.3.1 Synchronous Machine Model

Each conventional power plant of System-1 is represented by one equivalent turbine-generator unit, comprising of one synchronous generator (GEN) and one turbine section. The rotor electrical system of each GEN is represented in a *qdo* reference frame which rotates at the corresponding rotor speed. The rotor d-axis electrical system is represented by one field winding and one damper winding and rotor q-axis electrical system is modeled by two damper windings [61]. The magnetic saturation of both axes is also included in the model. The stator dynamics of each GEN are neglected and the stator electrical circuit is expressed by algebraic equations as part of the network model. The mechanical turbine-generator shaft system of each GEN is represented by a single equivalent rigid mass. The input mechanical power to each GEN is assumed to remain constant and the governor dynamics are not represented. Figure 2.2 provides a representative block diagram for each GEN model [62] and the equations expressing the electromechanical dynamical model of the i^{th} GEN are given by [62]:

$$T''_{doi}\frac{d\psi_{1di}}{dt} = E'_{qi} - \psi_{1di} - (X'_{di} - X_{lsi})\, I_{di}, \tag{2.1}$$

$$T'_{doi}\frac{dE'_{qi}}{dt} = E_{fdi} - E'_{qi} - S_{fdi} - (X_{di} - X'_{di})\left[I_{di} + \frac{(X'_{di} - X''_{di})}{(X'_{di} - X_{lsi})^2}\left(E'_{qi} - \psi_{1di} - (X'_{di} - X_{lsi})\, I_{di}\right)\right], \tag{2.2}$$

$$T''_{qoi}\frac{d\psi_{2qi}}{dt} = E'_{di} - \psi_{2qi} - (X'_{qi} - X_{lsi})\, I_{qi}, \tag{2.3}$$

$$T'_{qoi}\frac{dE'_{di}}{dt} = S_{1qi} - E'_{di} + (X_{qi} - X'_{qi})\left[I_{qi} - \frac{(X'_{qi} - X''_{qi})}{(X'_{qi} - X_{lsi})^2}\left(E'_{di} - \psi_{2qi} + (X'_{qi} - X_{lsi})\, I_{qi}\right)\right], \tag{2.4}$$

$$\psi''_{di} = \frac{(X''_{di} - X_{lsi})}{(X'_{di} - X_{lsi})} E'_{qi} + \frac{(X'_{di} - X''_{di})}{(X'_{di} - X_{lsi})} \psi_{1di}, \tag{2.5}$$

$$\psi''_{qi} = -\frac{(X''_{qi} - X_{lsi})}{(X'_{qi} - X_{lsi})} E'_{di} - \frac{(X'_{qi} - X''_{qi})}{(X'_{qi} - X_{lsi})} \psi_{2qi}, \tag{2.6}$$

$$|\psi''_i| = \sqrt{{\psi''_{qi}}^2 + {\psi''_{di}}^2}, \tag{2.7}$$

$$S_{fdi} = \frac{\psi''_{di}}{|\psi''_i|} \times S\left(|\psi''_i|\right), \tag{2.8}$$

$$S_{1q} = \frac{\psi''_{qi}\left(X_{qi} - X_{lsi}\right)}{|\psi''_i|\left(X_{di} - X_{lsi}\right)} \times S\left(|\psi''_i|\right), \tag{2.9}$$

$$S\left(|\psi''_i|\right) = \begin{cases} \dfrac{B_i(|\psi''_i| - A_i)^2}{|\psi''_i|}; & |\psi''_i| \geq A_i \\ 0; & |\psi''_i| < A_i \end{cases}, \tag{2.10}$$

$$\frac{d\delta_i}{dt} = \omega_o\left(\omega_i - \omega_s\right), \tag{2.11}$$

$$2H_i \frac{d\omega_i}{dt} = \frac{P_{m_i} - D_i\left(\omega_i - \omega_s\right) - P_{elec_i}}{\omega_i}, \tag{2.12}$$

$$\omega_o = 2\pi f_s, \tag{2.13}$$

$$P_{elec_i} = \left(\psi''_{di} I_{q_i} - \psi''_{qi} I_{di}\right) \frac{\omega_i}{\omega_s}, \tag{2.14}$$

$$I_{d_i} = \frac{\psi''_{di} - V_{q_i}}{X''_{di}}, \tag{2.15}$$

$$I_{q_i} = \frac{\psi''_{qi} + V_{d_i}}{X''_{di}}, \tag{2.16}$$

$$V_{d_i} = -V_i \sin\left(\theta_i - \delta_i\right), \tag{2.17}$$

$$V_{q_i} = V_i \cos\left(\theta_i - \delta_i\right), \tag{2.18}$$

$$I_i = \frac{\sqrt{{\psi''_{qi}}^2 + {\psi''_{di}}^2}}{X''_{di}}, \tag{2.19}$$

$$\gamma_i = \tan^{-1}\left(\frac{\psi''_{qi}}{\psi''_{di}}\right) + \delta_i - \frac{\pi}{2}. \tag{2.20}$$

where (2.1)-(2.10) define the rotor electrical model, (2.11)-(2.14) provide the rotor mechanical model, and (2.19)-(2.20) identify GEN injected current to the system.

2.3.2 Excitation Systems Models

The GENs connected to buses 2-8 and 13 are equipped with DC excitation systems and the GEN connected at Bus-9 (GEN-9) is equipped with a static exciter. It should be noted that the numbering of GEN-1 and GEN-13 are interchanged from the data given

in [60]. The rest of the synchronous generators are under constant excitation. GEN-i with a constant field voltage retain its constant internal voltage E_{fdi} during transients and E_{fdi} is determined from the pre-disturbance operating conditions. The dynamic models of different excitation systems are as follows. For the synchronous generators equipped with DC excitation system, the IEEE Type DC1A exciter model [62] is used which is mathematically described by:

$$T_{r_i}\frac{dV_{mi}}{dt} = V_i - V_{mi}, \tag{2.21}$$

$$T_{f_i}\frac{dR_{fi}}{dt} = \frac{K_{f_i}}{T_{f_i}}E_{fd_i} - R_{fi}, \tag{2.22}$$

$$T_{A_i}\frac{dV_{Ri}}{dt} = K_{A_i}R_{fi} - V_{Ri} - \frac{K_{A_i}K_{f_i}}{T_{f_i}}E_{fd_i} + K_{A_i}\left(V_{ref_i} - V_{mi}\right), \tag{2.23}$$

$$T_{E_i}\frac{dE_{fd_i}}{dt} = V_{R_{Limi}} - \left(K_{E_i}E_{fd_i} - S_E\left(E_{fd_i}\right)\right), \tag{2.24}$$

$$V_{R_{Limi}} = \begin{cases} V_{rmin_i}; & V_{Ri} < V_{rmin_i} \\ V_{Ri}; & V_{rmin_i} \leq V_{Ri} < V_{rmax_i} \\ V_{rmax_i}; & V_{Ri} \geq V_{rmax_i} \end{cases}, \tag{2.25}$$

$$S_E\left(E_{fd_i}\right) = \begin{cases} B_{ei}(E_{fd_i} - A_{ei})^2; E_{fd_i} \geq A_{ei} \\ 0; E_{fd_i} < A_{ei} \end{cases}. \tag{2.26}$$

For GEN-9, the governing equations of the static excitation system (IEEE Type ST1A) [62] are:

$$T_{m_i}\frac{dV_{mi}}{dt} = V_i - V_{mi}, \tag{2.27}$$

$$E_{fd_i} = K_{A_i}V_{lim_i}, \tag{2.28}$$

$$V_{lim_i} = \begin{cases} V_{min_i}; & V_{ei} < V_{min_i} \\ V_{ei}; & V_{min_i} \leq V_{ei} < V_{max_i} \\ V_{max_i}; & V_{ei} \geq V_{max_i} \end{cases}, \tag{2.29}$$

$$V_{ei} = V_{ref_i} - V_{mi} + V_{PSS_i}. \tag{2.30}$$

2.3.3 Power System Stabilizer Model

GEN-9 is also equipped with a Power System Stabilizer (PSS) which is driven by the rotor speed deviation signal which is obtained from its corresponding rotating shaft speed. It is composed of two lead-lag blocks to introduce phase shift into its output supplementary

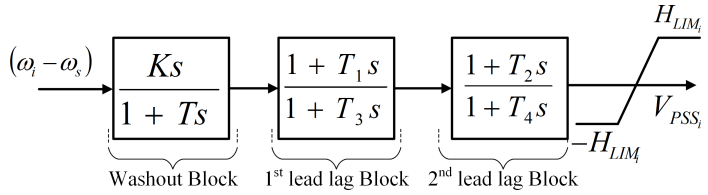

Figure 2.3: Block diagram of the PSS installed at GEN-9

signal (V_{PSSi}) and a washout block to ensure the supplementary signal is zero in the steady-state. Figure 2.3 shows the block diagram of the PSS of GEN-9. The dynamic model of the PSS is expressed as:

$$T_i \frac{dv_{1_i}}{dt} = -\left(\frac{K_i}{T_i}(\omega_i - \omega_s) + v_{1_i}\right), \tag{2.31}$$

$$T_{3_i} \frac{dv_{2_i}}{dt} = \left(\frac{T_{3_i} - T_{1_i}}{T_{3_i}}\right)\left(\frac{K_i}{T_i}(\omega_i - \omega_s) + v_{1_i}\right) - v_{2_i}, \tag{2.32}$$

$$T_{4_i} \frac{dv_{3_i}}{dt} = \left(\frac{T_{3_i} - T_{1_i}}{T_{3_i}}\right)\left(v_{2_i} + \left(\frac{T_{1_i}}{T_{3_i}}\right)\left(\frac{K_i}{T_i}(\omega_i - \omega_s) + v_{1_i}\right)\right) - v_{3_i}, \tag{2.33}$$

$$v_{4_i} = v_{3_i} + \left(\frac{T_{2_i}}{T_{4_i}}\right)\left(v_{2_i} + \left(\frac{T_{1_i}}{T_{3_i}}\right)\left(\frac{K_i}{T_i}(\omega_i - \omega_s) + v_{1_i}\right)\right), \tag{2.34}$$

$$V_{PSS_i} = \begin{cases} -H_{LIM_i}; & v_{4_i} < -H_{LIM_i} \\ v_{4_i}; & -H_{LIM_i} \leq v_{4_i} < H_{LIM_i} \\ H_{LIM_i}; & v_{4_i} \geq H_{LIM_i} \end{cases}. \tag{2.35}$$

2.3.4 AC Network Model

The AC network represents the transmission lines, transformers, and aggregated loads of the system. Each transformer is represented by its winding resistance, leakage reactance, and the off-nominal turns-ratio and each transmission line is modeled as an equivalent-π. Since the objective of this study is to investigate low-frequency dynamics, the AC network is modeled by algebraic equations describing the network nodal equations

$$\overline{I} = Y_N \times \overline{V}, \tag{2.36}$$

where $\overline{I}$ and $\overline{V}$ are the vectors of the current and voltage phasors and Y_N is the admittance matrix. Power system loads are modeled as constant impedances and are included in the Y_N matrix.

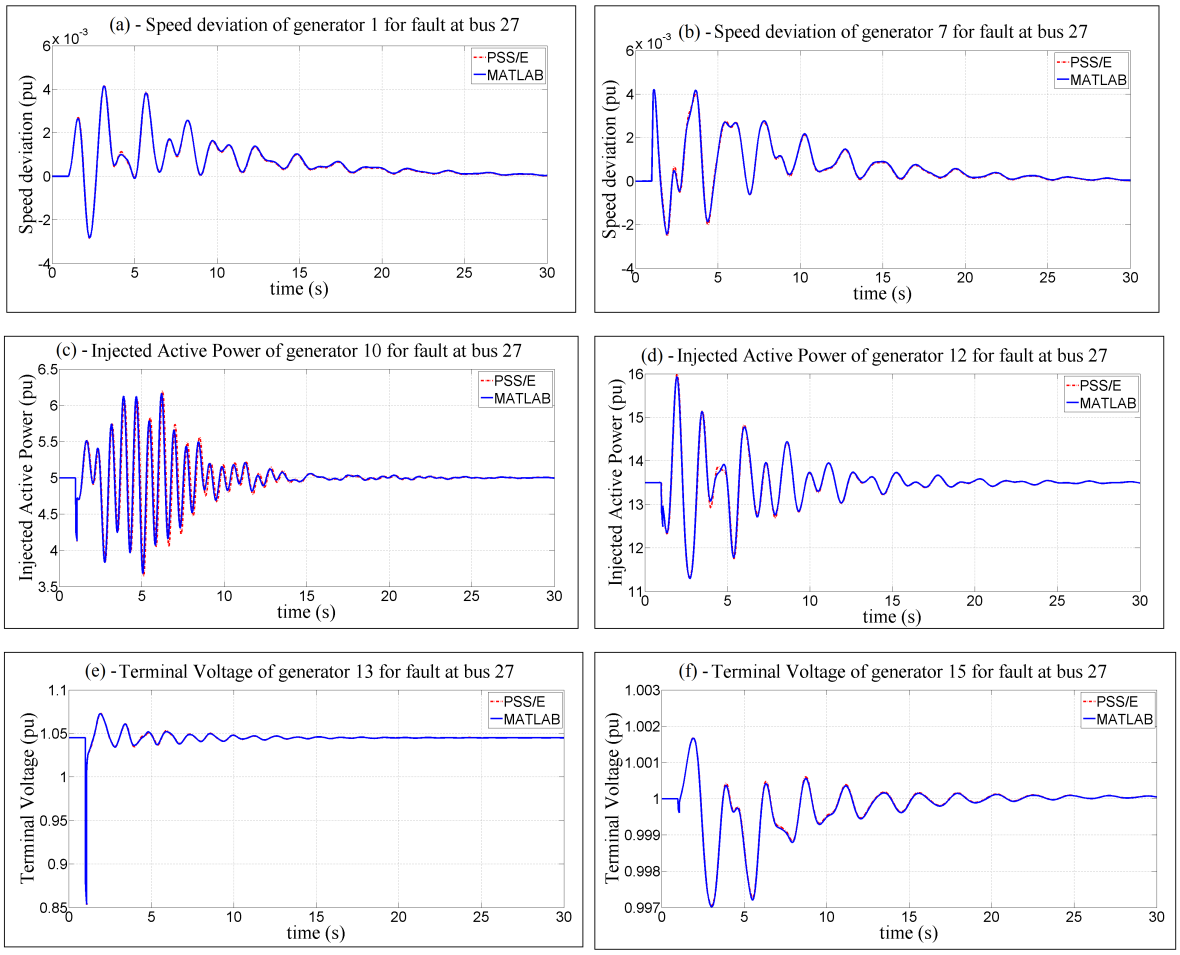

Figure 2.4: System-1 time-response to a three-phase, 5-cycle fault at Bus-27

2.4 Implementation and Validation of the Benchmark System Non-Linear Model in MATLAB/Simulink

The overall dynamic model of System-1, based on the component models of Section 2.3, was constructed and implemented in the MATLAB/Simulink software platform. To demonstrate the accuracy of the model, the time-responses of System-1 subject to faults at different locations and operating conditions are obtained and compared with the corresponding responses obtained from time-domain simulation of System-1 in the PSS/E production-grade platform (Ver 33.4) based on the PSS/E built-in component models.

Figure 2.4 provides a comparison between the corresponding results obtained from the

MATLAB/Simulink and the PSS/E. Initially, System-1 is under a steady-state full-load condition. At time t=1s, System-1 is subjected to a temporary, self-cleared, three-phases-to-ground fault for 5 cycles at Bus-27. Figure 2.4 shows the time-response of System-1 to this disturbance. Figure 2.4 shows close agreement between the corresponding results from both simulation platforms and verifies accuracy of the developed non-linear time-domain simulation of System-1 in the MATLAB/Simulink platform.

The speed deviation of GEN-1 and GEN-7, Figure 2.4(a) and (b), show that System-1 experiences low-frequency oscillations which are of significant interest when the depth of wind power integration increases in the system. This characteristic is also evident in the injected active power for GEN-10 and GEN-12, Figure 2.4(c) and (d).

2.5 Small-Signal Dynamical Stability Analysis of the Benchmark System

2.5.1 Model Development

The overall nonlinear model of System-1, based on the component models of Section 2.3, constitutes a set of Differential-Algebraic Equations (DAEs) in the general form of:

$$\dot{X} = f\left(X,\ I_g, V_g, U\right), \tag{2.37}$$

$$0 = g\left(X,\ I_g, V_g\right), \tag{2.38}$$

$$0 = h_1\left(X,\ I_g, V_g, V_l\right), \tag{2.39}$$

$$0 = h_2\left(V_g, V_l\right), \tag{2.40}$$

Equation (2.37) represents the dynamical model of all GENs which is constructed from (2.1)-(2.4), (2.11)-(2.12), (2.21)-(2.24), (2.27), and (2.31)-(2.33). Equation (2.38) represents the algebraic equations of all (i) GENs stator electrical systems, (ii) static exciters and (iii) PSS and are constructed from (2.15)-(2.18), (2.28)-(2.30), and (2.34) respectively. Equation (2.39) represents the network nodal equations for generator buses [62], i.e.,

$$\begin{aligned} 0 = {} & I_{d_i} V_i \sin\left(\delta_i - \theta_i\right) + I_{q_i} V_i \cos\left(\delta_i - \theta_i\right) + P_{L_i}\left(V_i\right) \\ & - \sum_{k=1}^{n} V_i V_k Y_{ik} \cos\left(\theta_i - \theta_k - \alpha_{ik}\right), \end{aligned} \tag{2.41}$$

$$0 = I_{d_i} V_i \cos(\delta_i - \theta_i) - I_{q_i} V_i \sin(\delta_i - \theta_i) + Q_{L_i}(V_i) - \sum_{k=1}^{n} V_i V_k Y_{ik} \sin(\theta_i - \theta_k - \alpha_{ik}). \quad (2.42)$$

Equation (2.40) represents the network nodal equations for non-generator buses by [62],

$$P_{L_i}(V_i) - \sum_{k=1}^{n} V_i V_k Y_{ik} \cos(\theta_i - \theta_k - \alpha_{ik}) = 0, \quad (2.43)$$

$$Q_{L_i}(V_i) - \sum_{k=1}^{n} V_i V_k Y_{ik} \sin(\theta_i - \theta_k - \alpha_{ik}) = 0. \quad (2.44)$$

X is the system states vector, U is the inputs vector, I_g is the vector of GENs d- and q-axis rotor currents, V_g is the vector of phase-angles and magnitudes of GENs terminal voltages, and V_l is the vector of phase-angles and magnitudes of non-generator bus voltages. Linearizing (2.37)-(2.40) about an operating point provides

$$\Delta\dot{X} = A_1 \Delta X + B_1 \Delta I_g + B_2 \Delta V_g + E_1 \Delta U, \quad (2.45)$$

$$0 = C_1 \Delta X + D_1 \Delta I_g + D_2 \Delta V_g, \quad (2.46)$$

$$0 = C_2 \Delta X + D_3 \Delta I_g + D_4 \Delta V_g + D_5 \Delta V_l, \quad (2.47)$$

$$0 = D_6 \Delta V_g + D_7 \Delta V_l, \quad (2.48)$$

where the entries of the matrices depend on the initial values of the system states, inputs and algebraic variables (I_g, V_g, V_l). Eliminating the algebraic variables from (2.45)-(2.48) results in the following linearized dynamic model of the system, i.e.,

$$\Delta\dot{X} = A_{sys} \Delta X + B_{sys} \Delta U, \quad (2.49)$$

where

$$A_{sys} = A_1 - B_1 {D_1}^{-1} C_1 - \left(B_2 - B_1 {D_1}^{-1} D_2\right) \left(D_4 - D_3 {D_1}^{-1} D_2 - D_5 {D_7}^{-1} D_6\right)^{-1} \left(C_2 - D_3 {D_1}^{-1} C_1\right),$$

$$B_{sys} = E_1.$$

It should be noted that an operating point for the system linearization is determined from the solution of algebraic equations (2.38)-(2.40) and

$$0 = f(X,\ I_g, V_g, U). \quad (2.50)$$

The magnetic saturation of GENs results in numerical non-linearity of this set of equations which requires iterative solution techniques.

2.5.2 Eigenstructure and Oscillatory Modes of System-1

The linearized model of (2.49) is used to investigate the small-signal dynamic characteristics of System-1 that serve as the basis to identify the impacts of wind power integration on the eigenstructure, low-frequency oscillatory modes and the dynamical behavior as discussed in Chapter 5. The eigenstructure analysis shows that System-1 includes 26 oscillatory modes as shown in Table 2.1. Eleven modes are control modes that are highly damped with damping ratios (ζ) [62] in the range of 61% - 100%. Seven modes have frequencies below 0.1 Hz. The remaining fifteen modes have relatively low damping ratios (ζ between 2.71% and 8.01%), four of which are inter-area modes and eleven modes are local plant modes. The participation factors associated with the different oscillatory modes reveal the following.

i. The control modes are associated with the magnetic flux and the excitation systems states of the synchronous generators.

ii. The least damped modes (16 and 17) are primarily affected by the power system stabilizer located at GEN-9.

iii. GEN-8 is the dominant contributor to modes 16 and 17 which is also, the closest generator to GEN-9.

iv. Mode 26 represents oscillations of Gen-8, GEN-9 and GEN-13 against the generators of the New York System. Mode 24 represents oscillations of GEN-2 – GEN-7, located at New England System, against the generators of the New York system. Therefore, the New England System can be divided into two groups, one including GEN-8, GEN-9 and GEN-13 and the other includes GEN-2 – GEN-7. These two groups do not oscillate against each other.

v. The other two inter-area modes represent oscillations of the generators of the New York System against the equivalent areas of Ontario (GEN-14), Michigan (GEN-15), and PJM (GEN-16).

The system eigenstructure shows that System-1 also exhibits low-frequency oscillations in the form of local plant modes and inter-area modes. These oscillations are evident in the time-response of System-1, Figure 2.4, when subjected to a large-signal disturbance.

Table 2.1: Oscillatory Modes of System-1 (Base Case)

Control Oscillatory Modes			Electromechanical Oscillatory Modes			
Mode	Frequency (Hz)	Damping (ζ) (%)	Mode	Frequency (Hz)	Damping (ζ) (%)	Mode Type
1	0.0264	100%	12	1.8831	6.91%	Local Modes
2	0.0451	99.69%	13	1.5631	8.01%	
3	0.0955	88.23%	14	1.5492	5.48%	
4	0.1332	85.93%	15	1.5373	7.48%	
5	1.6200	85.67%	16	1.4216	2.71%	
6	0.1585	84.31%	17	1.3384	3.61%	
7	0.0882	83.93%	18	1.2637	7.52%	
8	0.0907	79.69%	19	1.2227	6.53%	
9	0.0977	78.99%	20	1.2148	4.76%	
10	0.0946	77.65%	21	1.2051	6.40%	
11	0.3361	61.42%	22	1.074	6.51%	
			23	0.8104	5.52%	Inter-area Modes
			24	0.7653	4.29%	
			25	0.5602	6.66%	
			26	0.4242	7.71%	

Impact of wind power integration on these oscillatory modes is a major concern and thus a focus of this thesis.

2.6 Wind Power in System-1

This section describes the strategy to introduce wind power, in the form of large-scale WPPs, in System-1. Realistic introduction of wind power in System-1 is carried out based on the following:

- Identifying expected depth of penetration of wind power in the NPCC system. The selected penetration levels of wind power in this work are based on future wind power integrations in the system [63].
- Identifying the locations of wind power resources in the NPCC system, and thus WPP locations by mapping the schematic diagram of Figure 2.1 to the geographical area that it represents.
- Considering system load increase while the output from the conventional power plants remain unchanged, thus the WPPs accommodate the system expansion and load growth.

- Considering different distribution patterns to allocate the wind power in System-1.
- Considering various combinations of Type-3 and Type-4 WPPs. This enables identification of the impacts due to interactions among controllers of both WPP types.

2.6.1 Depth of Wind Power Penetration

The New England and New York systems, each has potential wind power resources that can reach to 25 GW capacities, including both offshore and onshore wind power [63]. Recent studies have identified the required transmission network upgrade of both systems for the integration of wind power, equivalent to 20% - 30% of the total annual energy demand in 2024 [63]. Therefore, in this thesis, three wind power penetration levels are selected to identify the impacts of wind power integration on the low-frequency dynamicis of System-1, i.e., 5%, 15%, and 30%. These levels are selected based on the identified ranges in [8, 9] as follows.

i. At low-penetration levels (up to 5%) the existing control and operation practices are expected to be sufficient to accommodate the added wind power.

ii. At medium-penetration levels (up to 15%) noticeable changes in the operation and control practices are needed to cope with the added WPPs.

iii. At high-penetration levels (beyond 15%) significant changes to the control and operation practices will be need. At high wind power penetration levels, it is anticipated that new operation and control strategies are required.

For the study cases reported in this thesis, the load of System-1 is increased uniformly under constant power factor and the output power of the conventional power plants are kept unchanged at the base case (hereafter refered to as Base-Case) which represents System-1 without any WPP. Thus the load growth is supplied by incoporating WPPs in the system. The Wind Power Penetration Level (WPPL) is defined as:

$$WPPL = \frac{WPPs \text{ MW}}{WPPs \text{ MW } + Conventional\ Power\ Plants\ MW} \times 100\% \tag{2.51}$$

2.6.2 WPP Locations

Figure 2.5 (©[2015] IEEE) provides the projection of the detailed representation of the NPCC system (based on 48 power plants and 140 buses) on the geographical area that it serves [64, 65] . Based on Figure 2.5 (©[2015] IEEE) and Figure 2.1, Figure 2.6 identifies

the areas of System-1 that accommodates large-scale on-shore and off-shore wind power integration in the future, i.e., two possible areas in the New England system and one possible area in the New York system. Thus, we categorize the WPPs as follows:

i. **New England Northern WPP group (hereafter Northern Group)**: The WPPs in the Northern Group are connected to Bus-26 and Bus-29, corresponding to on-shore wind power.

ii. **New England Southern WPP group (hereafter Southern Group)**: The WPPs in the Southern Group are connected to Bus-59 and Bus-65 to represent off-shore wind power.

iii. **New York WPP Group (hereafter New-York Group)**: The WPPs in New-York Group are connected to Bus-33 and Bus-45 and represent onshore wind power.

The Clustered-Distribution (CD) pattern and the Uniform-Distribution (UD) pattern are adopted to allocate the amount of wind power to each WPP. In the CD pattern, the WPPs of each group are connected at one bus in that group. For the UD pattern, equal amount of wind power are allocated to the six WPP locations. The reason of considering the two patterns is to identify the impacts of the added WPPs on (i) the dynamics of the area that they are integrated within and (ii) the inter-area oscillations as a function of the power exchange between different electrical areas. Finally, for each of the WPPLs and distribution patterns, different combinations of Type-3 and Type-4 WPPs are considered. This is achieved by varying the contribution perecntage of wind power from Type-3 WPPs to the total integrated wind power in System-1. Five combinations are considered which are 100%, 75%, 50%, 25%, and 0% of the total wind power from Type-3 WPPs. Combinations of Type-3 and Type-4 WPPs allows the investigation of:

i. Impact of each WPP type separately on the low-frequency dynamics.

ii. Impacts due to the interaction of both WPP types.

2.6.3 Study Cases

Based on the selected WPPLs (three levels), the wind power allocation patters (two patterns), and combinations of WPP types (five combinations); 30 study cases, corresponding to System-1 with WPPs, are considered as shown in Table 2.2, Table 2.3 and Table 2.4. These cases cover a wide range of scenarios of wind power integration. For each case, a power-flow study is performed to ensure that the initial operating conditions meet the steady-state power flow requirements, e.g., voltage profile.

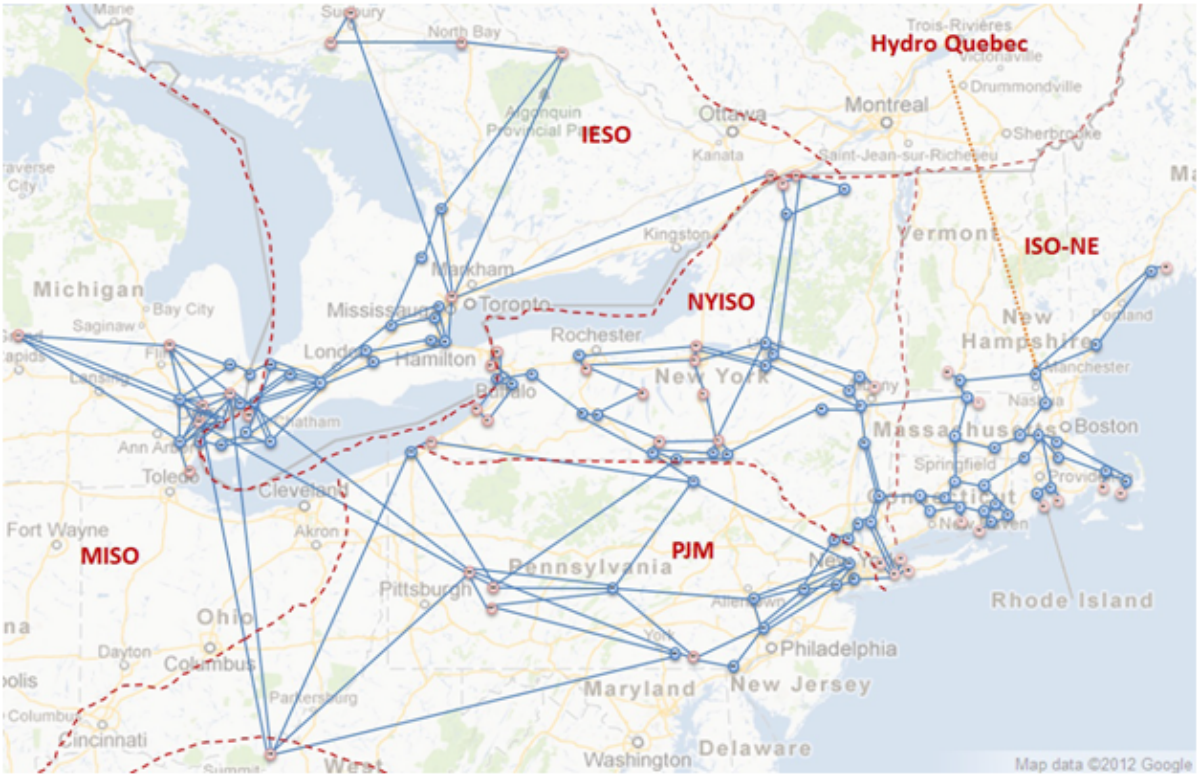

Figure 2.5: Projection of the detailed representation of the NPCC system on its geographical map

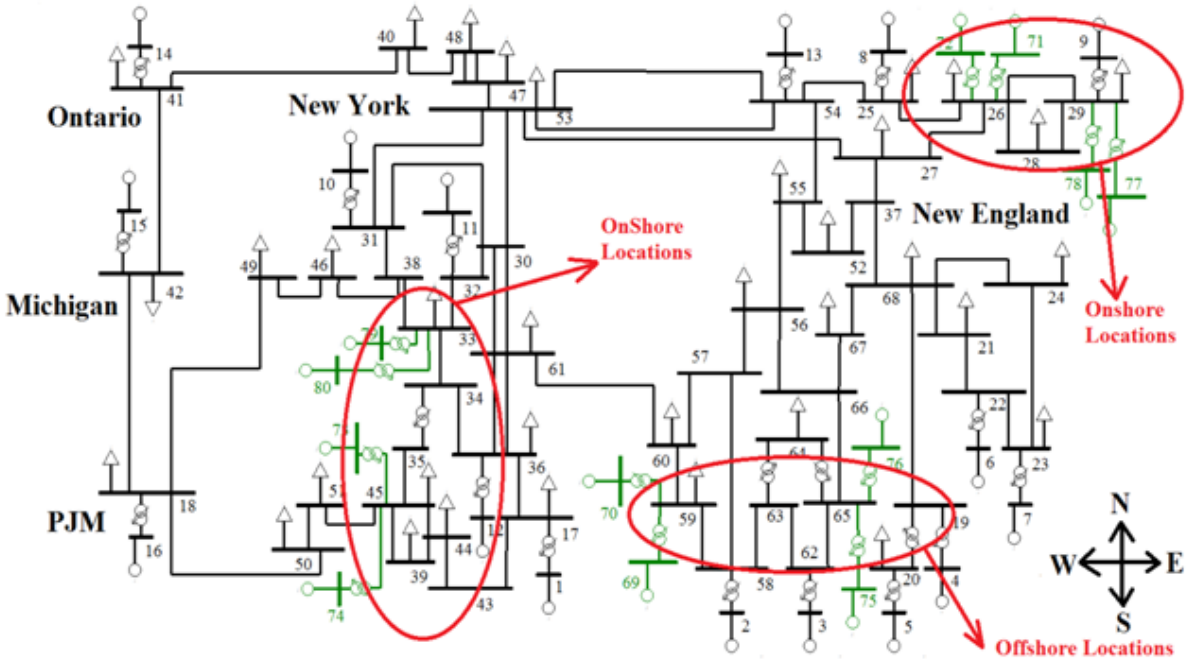

Figure 2.6: Schematic diagram of System-1 that identifies locations of WPPs

Table 2.2: Study cases for 5% WPPL

		Clustered distribution (CD)					Uniform distribution (UD)				
Installed Capacity (MW)		987.81									
# of Type-3 Units		660	495	330	165	0	660	495	330	165	0
# of Type-4 Units		0	100	200	300	400	0	100	200	300	400
Type-3 WPPs percentage		100%	75%	50%	25%	0%	100%	75%	50%	25%	0%
Bus-59	Type-3	660	495	330	165	0	330	248	165	82	0
	Type-4	0	100	200	300	400	0	50	100	150	200
Bus-65	Type-3	No WPPs Connected					330	247	165	83	0
	Type-4						0	50	100	150	200

Table 2.3: Study cases for 15% WPPL

		Clustered distribution (CD)					Uniform distribution (UD)				
Installed Capacity (MW)		3312.07									
# of Type-3 Units		2220	1665	1110	555	0	2220	1665	1110	555	0
# of Type-4 Units		0	330	660	990	1320	0	330	660	990	1320
Type-3 WPPs percentage		100%	75%	50%	25%	0%	100%	75%	50%	25%	0%
Bus-26	Type-3	740	555	370	185	0	370	277	185	92	0
	Type-4	0	110	220	330	440	0	55	110	165	220
Bus-29	Type-3	No WPPs Connected					370	278	185	93	0
	Type-4						0	55	110	165	220
Bus-33	Type-3						370	277	185	92	0
	Type-4						0	55	110	165	220
Bus-45	Type-3	740	555	370	185	0	370	278	185	93	0
	Type-4	0	110	220	330	440	0	55	110	165	220
Bus-59	Type-3	740	555	370	185	0	370	277	185	92	0
	Type-4	0	110	220	330	440	0	55	110	165	220
Bus-65	Type-3	No WPPs Connected					370	278	185	93	0
	Type-4						0	55	110	165	220

Table 2.4: Study cases for 30% WPPL

		Clustered distribution (CD)					Uniform distribution (UD)				
Installed Capacity (MW)		8043.61									
# of Type-3 Units		5400	4050	2700	1350	0	5400	4050	2700	1350	0
# of Type-4 Units		0	810	1620	2430	3240	0	810	1620	2430	3240
Type-3 WPPs percentage		100%	75%	50%	25%	0%	100%	75%	50%	25%	0%
Bus-26	Type-3	1350	1013	675	338	0	750	562	375	187	0
	Type-4	0	202	405	607	810	0	113	225	338	450
Bus-29	Type-3	No WPPs Connected					750	563	375	188	0
	Type-4						0	112	225	337	450
Bus-33	Type-3	1350	1013	675	338	0	1200	900	600	300	0
	Type-4	0	202	405	607	810	0	180	360	540	720
Bus-45	Type-3	1350	1012	675	337	0	1200	900	600	300	0
	Type-4	0	203	405	608	810	0	180	360	540	720
Bus-59	Type-3	1350	1012	675	337	0	750	562	375	187	0
	Type-4	0	203	405	608	810	0	113	225	338	450
Bus-65	Type-3	No WPPs Connected					750	563	375	188	0
	Type-4						0	112	225	337	450

2.7 Conclusions

This chapter presents the selected test system to investigate the impact of high-depth penetration of wind power integration on the power system transient stability. The nonlinear dynamic model of the test system is developed in MATLAB/Simulink platform and its accuracy is verified by comparing the transient time-response obtained from MATLAB/Simulink with that obtained from the system time-domain simulation in the PSS/E platform. The nonlinear dynamic model is also linearized about an operating point to deduce a small-signal dynamic (linear) model of the study system.

The nonlinear time-domain simulation and the eigenstructure analysis of the test system show that it experiences low-frequency oscillations in the form of lightly damped local plant oscillatory modes and inter-area oscillatory modes. These oscillatory modes are of significant interest when the depth of wind power integration increases in the system. These results form the basis for investigating the impacts of high-depth penetration of wind power integration in the subsequent chapters.

This chapter also presents a strategy to identify WPP locations and depth of penetration of wind power in the test system. The adopted approach considers system load increase to be accommodated by WPPs and hence the level of non-WPP generation remains unchanged. Two WPP distribution patterns and combinations of Type-3 and Type-4 WPPs are also considered, and thus 30 cases are specified to be investigated in

the following chapters. This covers a wide range of possible scenarios of wind power integration and provides study cases to investigate the impacts of high-depth of wind power penetration in the subsequent chapters.

Chapter 3

Wind Power Plant Models

3.1 Introduction

Identifying the impacts of high-depth penetration of wind power on the dynamic oscillatory modes and transient stability of a power system requires appropriate WPP models for large-signal (nonlinear) and small-signal dynamic analyses of the overall power system. Such models (i) must represent the WPP dynamics in the frequency range of transient stability studies, i.e., 0.1 to 2 Hz and (ii) should not impose prohibitive computational burden when used for transient studies of realistic size power systems. These requirements make the equivalent models of the WPP more suitable, as compared to the detailed models, for this type of studies. The PSS/E-software built-in generic (equivalent) models have been widely used and also verified against field measurement results [27]. However, the models constructed based on different documents [4, 22, 23, 27, 28] cannot be used to replicate the time-responses of the PSS/E built-in models. In addition, these documents do not discuss the hybrid nature of the generic models which is evident in the time-response of the PSS/E built-in models as discussed in Chapter 4.

To overcome the above, this chapter introduces and develops enhanced equivalent models of the Type-3 and Type-4 WPPs. The models are inherently nonlinear and their salient features are (i) they replicate the field verified time-responses of the PSS/E software built-in models, (ii) they highlight the hybrid nature of the generic models by encompassing all discrete logics associated with different limits, and (iii) they are implementable in any time-domain simulation platform, e.g., MATLAB/Simulink platform. The developed enhanced WPP models are implemented in the MATLAB/Simulink-based dynamic nonlinear model of System-1, Chapter 2, Section 2.3, to investigate the impact of wind power on System-1 dynamics. This chapter also (i) presents linearized WPPs models extracted from the developed nonlinear enhanced generic models and (ii) discusses

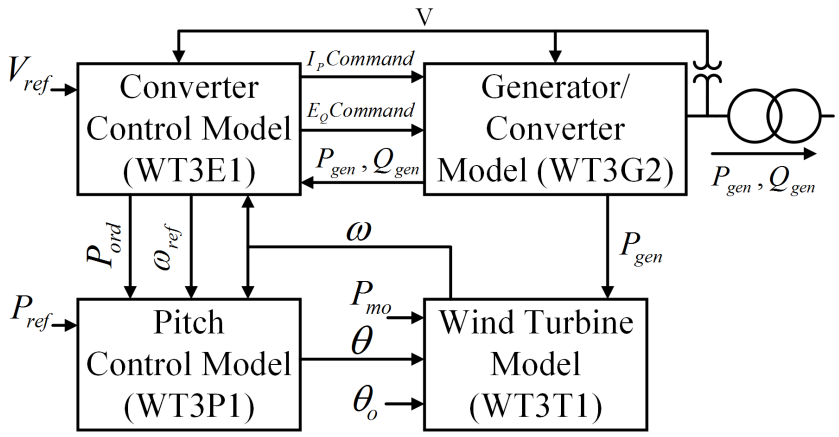

Figure 3.1: Type-3 WPP functional blocks

the impacts of the discrete event logics on the small-signal dynamic analyses. Chapter 4 provides comprehensive performance evaluation and verification of the developed nonlinear and linearized models. The linearized and the nonlinear WPPs models are used to identify the impacts of high-depth of wind power penetration on the low-frequency oscillations and transient stability in the following chapters.

3.2 Enhanced Type-3 WPP Model

For transient stability analysis of a power system where the internal dynamics of the WPP is not of concern, the concept of equivalencing is used to represent the WPP, e.g., the generic model [66] with respect to the host grid. Hereafter the term WPP refers to the equivalent of the wind power plant at its point of connection. Figure 3.1 represents the structure of the generic model of the Type-3 WPP [27], and consists of the following four blocks [28].

3.2.1 WT3G2 - Generator/Converter Model

This block represents the generator and the rotor-connected converter. The electrical dynamics of the generator stator and rotor are neglected since they are much faster than those of the converter. Thus, the dynamics of the converter are the dominant and are represented by first-order transfer functions to reflect fast dynamic response of the converter to the commands from the converter control model. This enables representation of the generator by a controlled current source as shown in Figure 3.2 which also incorporates Low Voltage active Power Logic (LVPL) and reactive current management logic [28].

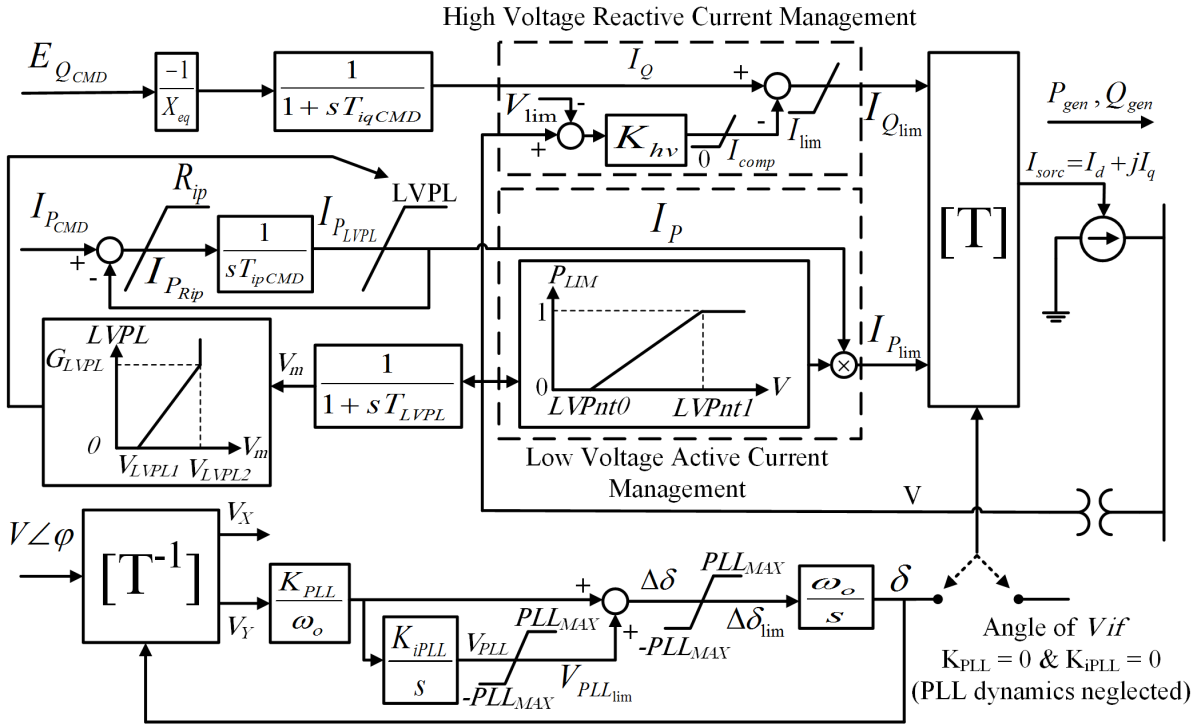

Figure 3.2: Type-3 WPP Generator/Converter Model

The LVPL limits the WPP active current component based on the value of the terminal voltage. The salient factor in the post-fault period is the active current ramp rate limit. The high voltage reactive current logic mitigates over-voltage by reducing the injected reactive power as limited by the machine rating. The model also includes a Phase-Locked Loop (PLL) unit. The PLL dynamics are practically very fast relative to the time frame of the transient stability studies and thus can be neglected. Thus, the non-linear model of the generator/converter can be expressed as:

$$\frac{dI_Q}{dt} = \frac{1}{T_{iq_{CMD}}}\left(\frac{-E_{q_{CMD}}}{X_{eq}} - I_Q\right), \tag{3.1}$$

$$\frac{dI_{P_{LVPL}}}{dt} = \frac{I_{P_{R_{ip}}}}{T_{ip_{CMD}}}, \tag{3.2}$$

$$\frac{dV_m}{dt} = \frac{1}{T_{LVPL}}\left(V - V_m\right), \tag{3.3}$$

$$\frac{dV_{PLL}}{dt} = K_{iPLL}\left[V_Y \frac{K_{PLL}}{\omega_o}\right], \tag{3.4}$$

$$\frac{d\delta}{dt} = \omega_o \Delta\delta_{lim}, \tag{3.5}$$

$$\begin{bmatrix} I_d \\ I_q \end{bmatrix} = \begin{bmatrix} \cos\delta & -\sin\delta \\ \sin\delta & \cos\delta \end{bmatrix} \begin{bmatrix} I_{P_{lim}} \\ I_{Q_{lim}} \end{bmatrix}, \tag{3.6}$$

$$I_{SORC} = I_d + jI_q, \tag{3.7}$$

$$\Delta\delta = V_{PLLlim} + V_Y \frac{K_{PLL}}{\omega_o}, \tag{3.8}$$

$$P_{gen} = I_{P_{lim}} \times V, \tag{3.9}$$

$$Q_{gen} = -\left(I_{Q_{lim}} + \frac{V}{X_{eq}}\right) \times V, \tag{3.10}$$

$$I_{P_{R_{ip}}} = \begin{cases} I_{P_{CMD}} - I_P; & (I_{P_{CMD}} - I_P) < R_{ip} \\ R_{ip}; & (I_{P_{CMD}} - I_P) \geq R_{ip} \end{cases}, \tag{3.11}$$

$$I_P = \begin{cases} I_{P_{LVPL}}; & I_{P_{LVPL}} < LVPL \\ LVPL; & I_{P_{LVPL}} \geq LVPL \end{cases}, \tag{3.12}$$

$$I_{P_{lim}} = I_P \times P_{lim}, \tag{3.13}$$

$$LVPL = \begin{cases} 0; & V_m < V_{LVPL1} \\ \dfrac{G_{LVPL}\,(V_m - V_{LVPL1})}{(V_{LVPL2} - V_{LVPL1})}; & V_{LVPL1} \leq V_m < V_{LVPL2} \\ Very\ large\ value; & V_m \geq V_{LVPL2} \end{cases}, \tag{3.14}$$

$$I_{Q_{lim}} = \begin{cases} I_{lim}; & (I_Q - I_{comp}) < I_{lim} \\ I_Q - I_{comp}; & (I_Q - I_{comp}) \geq I_{lim} \end{cases}, \tag{3.15}$$

$$I_{comp} = \begin{cases} 0; & V \leq V_{lim} \\ K_{hv}\,(V - V_{lim})\,; & V > V_{lim} \end{cases}, \tag{3.16}$$

$$P_{lim} = \begin{cases} 0; & V < LVPnt0 \\ \dfrac{V\,(V - LVPnt0)}{(LVPnt1 - LVPnt0)}; & LVPnt0 \leq V < LVPnt1 \\ 1; & V \geq LVPnt1 \end{cases}, \tag{3.17}$$

$$V_{PLLlim} = \begin{cases} -PLL_{MAX}; & V_{PLL} < -PLL_{MAX} \\ V_{PLL}; & -PLL_{MAX} \leq V_{PLL} < PLL_{MAX} \\ PLL_{MAX}; & V_{PLL} \geq PLL_{MAX} \end{cases}, \tag{3.18}$$

$$\Delta\delta_{lim} = \begin{cases} -PLL_{MAX}; & \Delta\delta_{lim} < -PLL_{MAX} \\ \Delta\delta; & -PLL_{MAX} \leq \Delta\delta_{lim} < PLL_{MAX} \\ PLL_{MAX}; & \Delta\delta_{lim} \geq PLL_{MAX} \end{cases}, \tag{3.19}$$

and P_{gen} (Q_{gen}) is the injected active (reactive) power in the system and are in per unit based on the WPP rated apparent power.

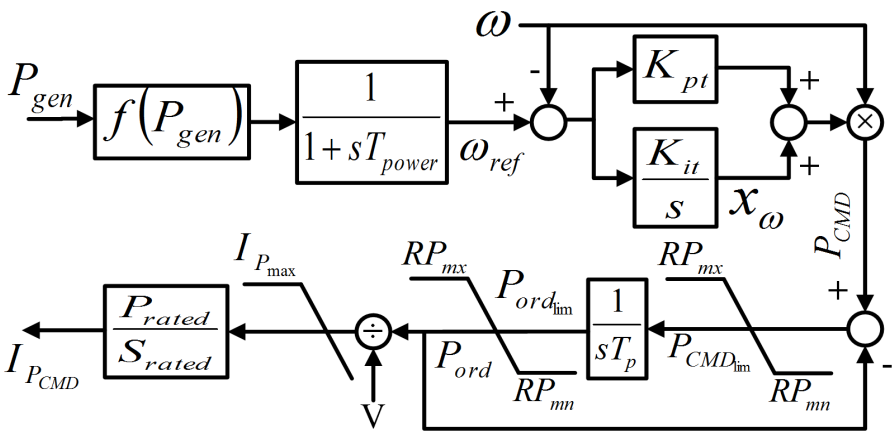

Figure 3.3: Type-3 WPP Converter Control Model—Active Power Control

3.2.2 WT3E1 - Converter Control Model

3.2.2.1 Active Power Control

Figure 3.3 shows the active power control stream, where the wind turbine reference speed (ω_{ref}) is determined from a piece-wise linear relation with the generated active power and a PI-controller based on speed error is used for torque control to determine the active power command. Reference [4] proposes a logic for activating the limits of the PI-controller, however; this can cause erroneous results as will be shown in Chapter 4, and thus eliminated in the developed enhanced model of this chapter. In addition, the active power control is carried out based on the rated active power of the WPP. Therefore, the active current command to the generator/converter block is recalculated based on the WPP rated apparent power. This step is not clarified in various documents describing Type-3 WPP model and the addition of this step is considered as the first enhancement to the generic model of Figure 3.3. From Figure 3.3, the enhanced active power control is:

$$\frac{d\omega_{ref}}{dt} = \frac{1}{T_{power}} \left(f\left(P_{gen}\right) - \omega_{ref} \right), \tag{3.20}$$

$$\frac{dx_{\omega}}{dt} = K_{it} \left(\omega - \omega_{ref} \right), \tag{3.21}$$

$$\frac{dP_{ord_{lim}}}{dt} = \frac{P_{CMD_{lim}}}{T_{fp}}, \tag{3.22}$$

$$P_{CMD} = \omega \left(x_{\omega} + K_{Pt} \left(\omega - \omega_{ref} \right) \right), \tag{3.23}$$

$$P_{CMD_{lim}} = \begin{cases} RP_{mn}; & (P_{CMD} - P_{ord}) < RP_{mn} \\ P_{CMD} - P_{ord}; & RP_{mn} \leq (P_{CMD} - P_{ord}) < RP_{mx} \\ RP_{mx}; & (P_{CMD} - P_{ord}) \geq RP_{mx} \end{cases}, \tag{3.24}$$

$$P_{ord} = \begin{cases} P_{mn}; & P_{ord_{lim}} < P_{mn} \\ P_{ord_{lim}}; & P_{mn} \leq P_{ord_{lim}} < P_{mx} \\ P_{mx}; & P_{ord_{lim}} \geq P_{mx} \end{cases}, \tag{3.25}$$

$$I_{P_{CMD}} = \begin{cases} \left(\frac{P_{rated}}{S_{rated}}\right)\left(\frac{P_{ord}}{V}\right); & \frac{P_{ord}}{V} < I_{P_{max}} \\ \left(\frac{P_{rated}}{S_{rated}}\right) I_{P_{max}}; & \frac{P_{ord}}{V} \geq I_{P_{max}} \end{cases}. \tag{3.26}$$

3.2.2.2 Reactive Power Control

The reactive power control is composed of (i) the reactive power command (Q_{CMD}) determination mechanism and (ii) the Volt/VAR control as shown in Figure 3.4. The model allows Q_{CMD} to be determined from any of the following three alternatives based on the user-specified flag, VARFLG, i.e.:

i. From a Separate Model (Q_{ref}): This option is used when a PSS-like function is to be added to the system to allow the WPP to contribute to the system damping.

ii. From a WPP Reactive Power Emulator: This represents a simplified equivalent of the WPP supervisory reactive power management system.

iii. From a Power Factor Regulator.

During disturbances that results in low voltages at the WPP terminal, all integrators of the WPP reactive power emulator are frozen at their pre-disturbance values to avoid the integrators wind-up. This function is adopted from [24] but mentioned neither in the PSS/E nor the WECC related documents. Neglecting this function (as discussed in Chapter 4) can highly impact the system response. This freezing function is the second enhancement of this work to the generic model of Type-3 WPP. The Volt/VAR control determines the voltage command (E_{qCMD}) based on the desired injected reactive power and the limits represent the hardware limitations. Based on VARFLG=1 and VLTFLG=1 in Figure 3.4, the system equations are:

$$\frac{dV_{m_e}}{dt} = \frac{1}{T_{RV}}\left(V - V_{m_e}\right), \tag{3.27}$$

$$\frac{dx_{iv}}{dt} = \frac{K_{iv}}{f_n}\left(V_{ref} - V_{m_e}\right) \times y_{frz}, \tag{3.28}$$

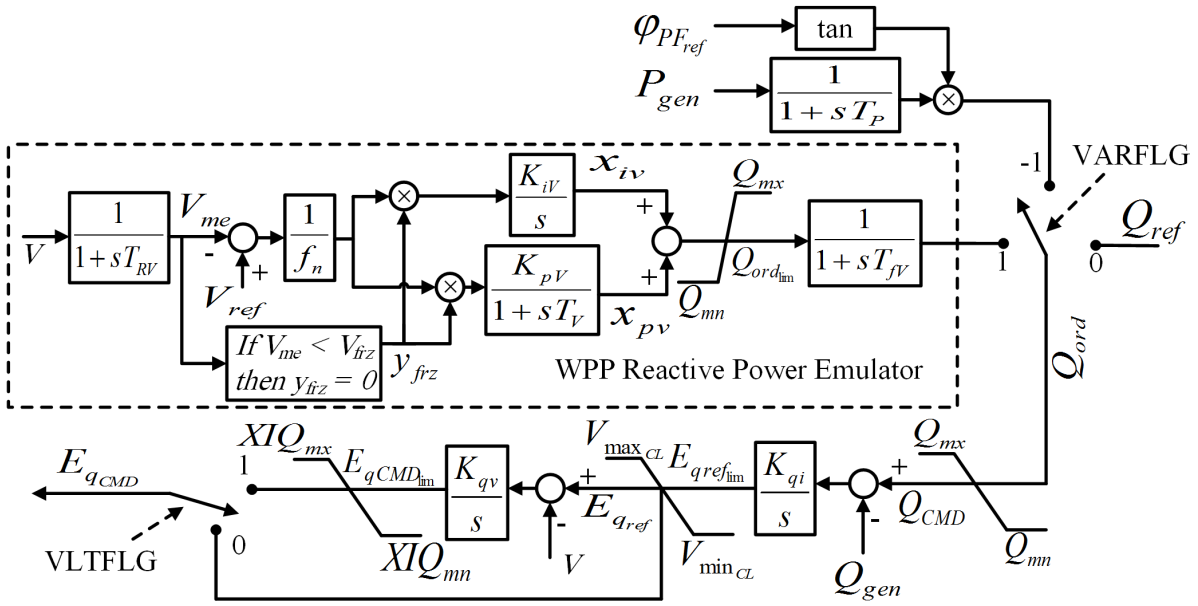

Figure 3.4: Type-3 WPP Converter Control Model—Reactive Power Control

$$\frac{dx_{pv}}{dt} = \frac{K_{pv}}{T_V f_n}\left(V_{ref} - V_{m_e} - \frac{f_n x_{pv}}{K_{pv}}\right) \times y_{frz}, \tag{3.29}$$

$$\frac{dQ_{ord}}{dt} = \frac{1}{T_{fV}}\left(Q_{ord_{lim}} - Q_{ord}\right), \tag{3.30}$$

$$\frac{dE_{q_{ref_{lim}}}}{dt} = K_{qi}\left(Q_{CMD} - Q_{gen}\right), \tag{3.31}$$

$$\frac{dE_{q_{CMD_{lim}}}}{dt} = K_{qv}\left(E_{q_{ref}} - V\right), \tag{3.32}$$

$$y_{frz} = \begin{cases} 0; & V_{m_e} < V_{frz} \\ 1; & V_{m_e} \geq V_{frz} \end{cases}, \tag{3.33}$$

$$Q_{ord_{lim}} = \begin{cases} Q_{mn}; & (x_{iv} + x_{pv}) < Q_{mn} \\ x_{iv} + x_{pv}; & Q_{mn} \leq (x_{iv} + x_{pv}) < Q_{mx} \\ Q_{mx}; & (x_{iv} + x_{pv}) \geq Q_{mx} \end{cases}, \tag{3.34}$$

$$Q_{CMD} = \begin{cases} Q_{mn}; & Q_{ord} < Q_{mn} \\ Q_{ord}; & Q_{mn} \leq Q_{ord} < Q_{mx} \\ Q_{mx}; & Q_{ord} \geq Q_{mx} \end{cases}, \tag{3.35}$$

$$E_{q_{ref}} = \begin{cases} V_{min_{CL}}; & E_{q_{ref_{lim}}} < V_{min_{CL}} \\ E_{q_{ref_{lim}}}; & V_{min_{CL}} \leq E_{q_{ref_{lim}}} < V_{max_{CL}} \\ V_{max_{CL}}; & E_{q_{ref_{lim}}} \geq V_{max_{CL}} \end{cases}, \tag{3.36}$$

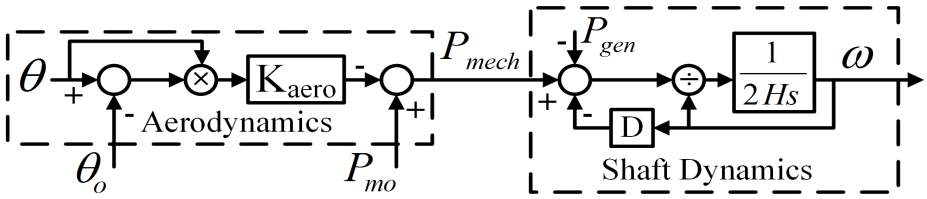

Figure 3.5: Type-3 WPP Wind Turbine Model

$$E_{q_{CMD}} = \begin{cases} XIQ_{mn}; & E_{q_{CMD_{lim}}} < XIQ_{mn} \\ E_{q_{CMD_{lim}}}; & XIQ_{mn} \leq E_{q_{CMD_{lim}}} < XIQ_{mx} \\ XIQ_{mx}; & E_{q_{CMD_{lim}}} \geq XIQ_{mx} \end{cases} . \tag{3.37}$$

3.2.3 WT3T1 - Wind Turbine-Generator Mechanical Model

The mechanical system of a wind turbine can be represented either by a two- or a single-mass model [24]. Figure 3.5 shows the single-mass model which also represents (i) the aerodynamics governing the relation between the pitch angle (θ) and the mechanical power ((P_{mech})) and (ii) the shaft dynamics under constant wind speed [26]. The model adopts an approximation to C_p characteristics [67]. From Figure 3.5, the wind turbine dynamics are:

$$\frac{d\omega}{dt} = \frac{1}{2H}\left(\frac{P_{mech} - P_{gen} - D\omega}{\omega}\right), \tag{3.38}$$

$$P_{mech} = P_{m_o} - K_{aero}\theta\left(\theta - \theta_o\right), \tag{3.39}$$

where (P_{m_o}) and (θ_o) are the initial values of the mechanical power and the pitch angle respectively.

3.2.4 WT3P1 - Pitch Angle Control Model

WT3P1 of Figure 3.6 provides the input pitch angle to the turbine model as shown in Figure 3.1, and assumes the pitch angle is at its minimum value at the rated wind speed. It also incorporates non-windup limits [4,24] based on the blocking logic of discrete-valued variables y_p and y_c for the pitch control and pitch compensation integrators respectively. y_p and y_c are determined from Table 3.1 (and Figure 3.7) where "err" is the error signal input to the integrators, ω_{err} in case of y_p and P_{err} in case of y_c.

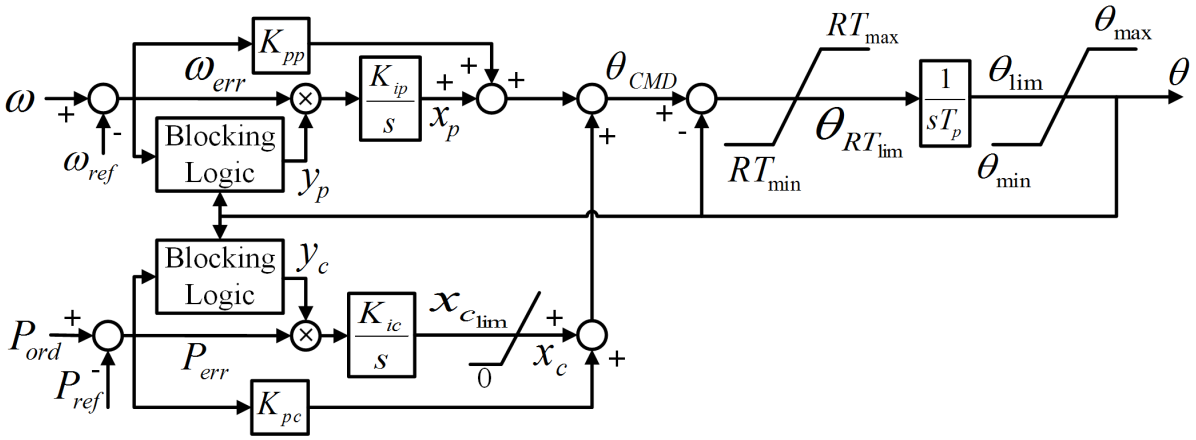

Figure 3.6: Type-3 WPP Pitch Angle Control Model

Table 3.1: Truth Table for the Discrete Blocking Signals y_p and y_c

	$\theta = \theta_{max}$	$\theta = \theta_{min}$	$\theta_{min} < \theta < \theta_{max}$
err >0	0	1	1
err <0	1	0	1
err $= 0$	1	1	1

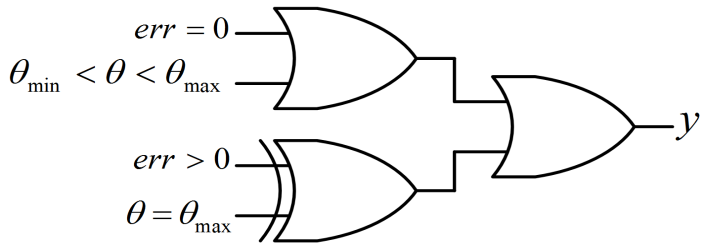

Figure 3.7: Type-3 WPP Blocking Logic Realization

The non-windup limits have significant impacts on the dynamic response of the Type-3 WTG model, i.e., (i) switching deadlock response and (ii) the convergence of the system to a different steady-state other than the pre-disturbance one, even if the pre- and post-disturbance system parameters are the same [4]. Reference [4] addresses the switching deadlock by hysteresis characteristics in the switching of the non-windup limits. The dynamics of the pitch angle control, based on Figure 3.6, are expressed as:

$$\frac{dx_p}{dt} = K_{ip}\left(\omega - \omega_{ref}\right) \times y_p, \tag{3.40}$$

$$\frac{dx_{clim}}{dt} = K_{ic}\left(P_{ord} - P_{ref}\right) \times y_c, \tag{3.41}$$

$$\frac{d\theta_{lim}}{dt} = \frac{\theta_{RT_{lim}}}{T_p}, \tag{3.42}$$

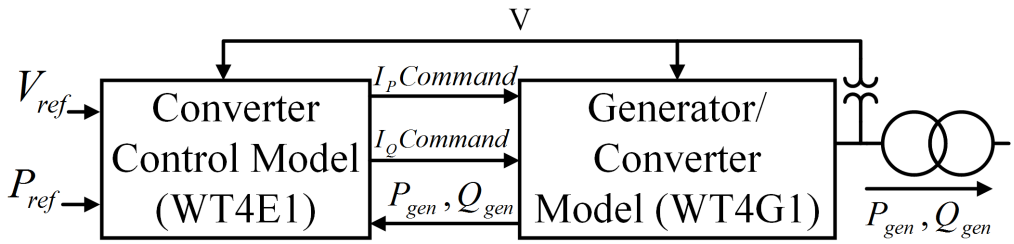

Figure 3.8: Type-4 WPP functional blocks

$$\theta_{CMD} = x_c + K_{pc}\left(P_{ord} - P_{ref}\right) + x_p + K_{pp}\left(\omega - \omega_{ref}\right), \tag{3.43}$$

$$x_c = \begin{cases} 0; & x_{clim} < 0 \\ x_{clim}; & x_{clim} \geq 0 \end{cases}, \tag{3.44}$$

$$\theta_{RT_{lim}} = \begin{cases} RT_{min}; & (\theta_{CMD} - \theta) < RT_{min} \\ \theta_{CMD} - \theta; & RT_{min} \leq (\theta_{CMD} - \theta) < RT_{max} \\ RT_{max}; & (\theta_{CMD} - \theta) \geq RT_{max} \end{cases}, \tag{3.45}$$

$$\theta = \begin{cases} \theta_{min}; & \theta_{lim} < \theta_{min} \\ \theta_{lim}; & \theta_{min} \leq \theta_{lim} < \theta_{max} \\ \theta_{max}; & \theta_{lim} \geq \theta_{max} \end{cases}. \tag{3.46}$$

3.3 Enhanced Type-4 WPP Model

Figure 3.8 shows the structure of Type-4 WPP model [27] and consists of blocks WT4G1 and WT4E1. The Type-4 WPP does not represent the mechanical system. Since Type-4 WPP model has commonalities with Type-3 WPP, the WT3G2 and WT3E1 of Figure 3.1 are used as the basis for WT4G1 and WT4E1 respectively of Figure 3.8, and only the differences are highlighted in the following sub-sections.

3.3.1 WT4G1 - Generator/Converter Model

Figure 3.9 shows the dynamic model of the generator/converter. Similar to the WT3G2 block of Type-3 WPP, WT4G1 block is based on active and reactive current commands from the converter control model. The PLL dynamics are ignored, since they are very fast relative to the time frame of the transient stability studies and the overall WPP dynamics are dominated by the converter dynamic characteristics, thus, angle δ is the phase-angle of the terminal bus voltage. Based on the commonalities of WT3G2 and

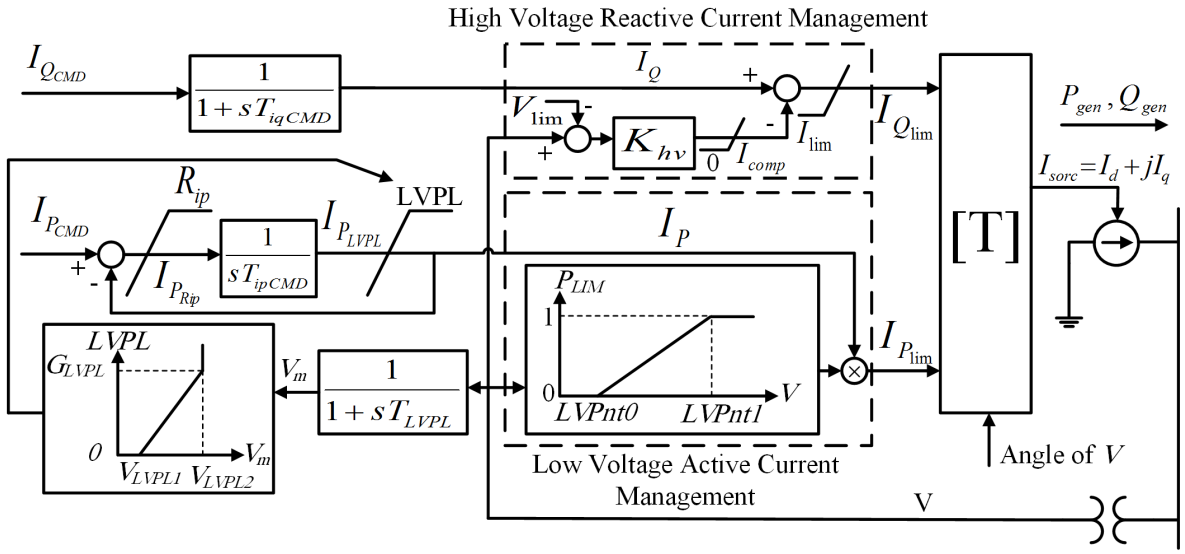

Figure 3.9: Type-4 WPP Generator/Converter Model

WT4G1, (3.1)–(3.3), (3.6), (3.7) and (3.9)–(3.17) are also applicable to WT4G1 while (3.1) and (3.10) change to (3.47) and (3.48), respectively, i.e.,

$$\frac{dI_Q}{dt} = \frac{-1}{T_{iq_{CMD}}} \left(I_{Q_{CMD}} + I_Q\right), \tag{3.47}$$

$$Q_{gen} = -I_{Q_{lim}} V. \tag{3.48}$$

3.3.2 WT4E1 - Converter Control Model

As compared with the converter control model of Type-3 WPP, in Type-4 WPP:

i. The active power control stream is changed to reflect the lack of dependency on the turbine speed change.

ii. The active power control is based on the WPP apparent power and thus the recalculation step, as in Type-3 WPP, is not required.

iii. The active power and reactive power control streams are coupled through the converter current limiter as shown in Figure 3.10. The current limiter prevents the net current exceeding the rating of the converter based on the (i) maximum temperature dependent current of the converter (I_{maxTD}), (ii) hard active ($I_{P_{hl}}$) and reactive ($I_{Q_{hl}}$) currents limits, (iii) active ($I_{P_{CMD}}$) and reactive ($I_{Q_{CMD}}$) currents commands,

(iv) terminal voltage, and (v) system operator requirements represented in the PQ priority (flag PQFLAG of Figure 3.11).

Therefore, the Type-4 WPP model is also enhanced by a freezing function of the reactive power emulator. Thus, (3.27)–(3.37) also describe the reactive power control stream of WT4E1 while (3.32) and (3.37) change to (3.49) and (3.50), respectively, i.e.,

$$\frac{dI_{q_{CMD_{lim}}}}{dt} = K_{qv}\left(E_{q_{ref}} - V\right), \tag{3.49}$$

$$I_{q_{CMD}} = \begin{cases} I_{q_{mn}}; & I_{q_{CMD_{lim}}} < I_{q_{mn}} \\ I_{q_{CMD_{lim}}}; & I_{q_{mn}} \leq I_{q_{CMD_{lim}}} < I_{q_{mx}} \\ I_{q_{mx}}; & I_{q_{CMD_{lim}}} \geq I_{q_{mx}} \end{cases}. \tag{3.50}$$

The active power control stream is represented by

$$\frac{dP_{gen_f}}{dt} = \frac{1}{T_{power}}\left(P_{gen} - P_{gen_f}\right), \tag{3.51}$$

$$\frac{dx_{it}}{dt} = K_{it}\left(P_{gen_f} + x_f - \frac{K_f}{T_f}P_{CMD_{lim}} - P_{ref}\right), \tag{3.52}$$

$$\frac{dx_f}{dt} = \frac{1}{T_f}\left(\frac{K_f}{T_f}P_{CMD_{lim}} - x_f\right), \tag{3.53}$$

$$I_{P_{CMD}} = \begin{cases} \dfrac{P_{ord}}{V}; & \dfrac{P_{ord}}{V} < I_{P_{max}} \\ I_{P_{max}}; & \dfrac{P_{ord}}{V} \geq I_{P_{max}} \end{cases}, \tag{3.54}$$

$$P_{CMD_{lim}} = \begin{cases} P_{mn}; & P_{CMD} < P_{mn} \\ P_{CMD}; & P_{mn} \leq P_{CMD} < P_{mx} \\ P_{mx}; & P_{CMD} \geq P_{mx} \end{cases}, \tag{3.55}$$

$$P_{CMD} = x_{it} + K_{pt}\left(P_{gen_f} + x_f - \frac{K_f}{T_f}P_{CMD_{lim}} - P_{ref}\right), \tag{3.56}$$

$$P_{ord} = P_{ref} - P_{CMD_{lim}}. \tag{3.57}$$

3.4 WPP Linearized Models

Reference [4] is the only document that develops a linearized model based on the generic model of Type-3 WPP. However, it suffers from the limitations discussed in Chapter 1, i.e.

i. Neglecting the generator/converter model, which results in two zero-eigenvalues and thus the eigenstructure is not a full representation of the system dynamics.

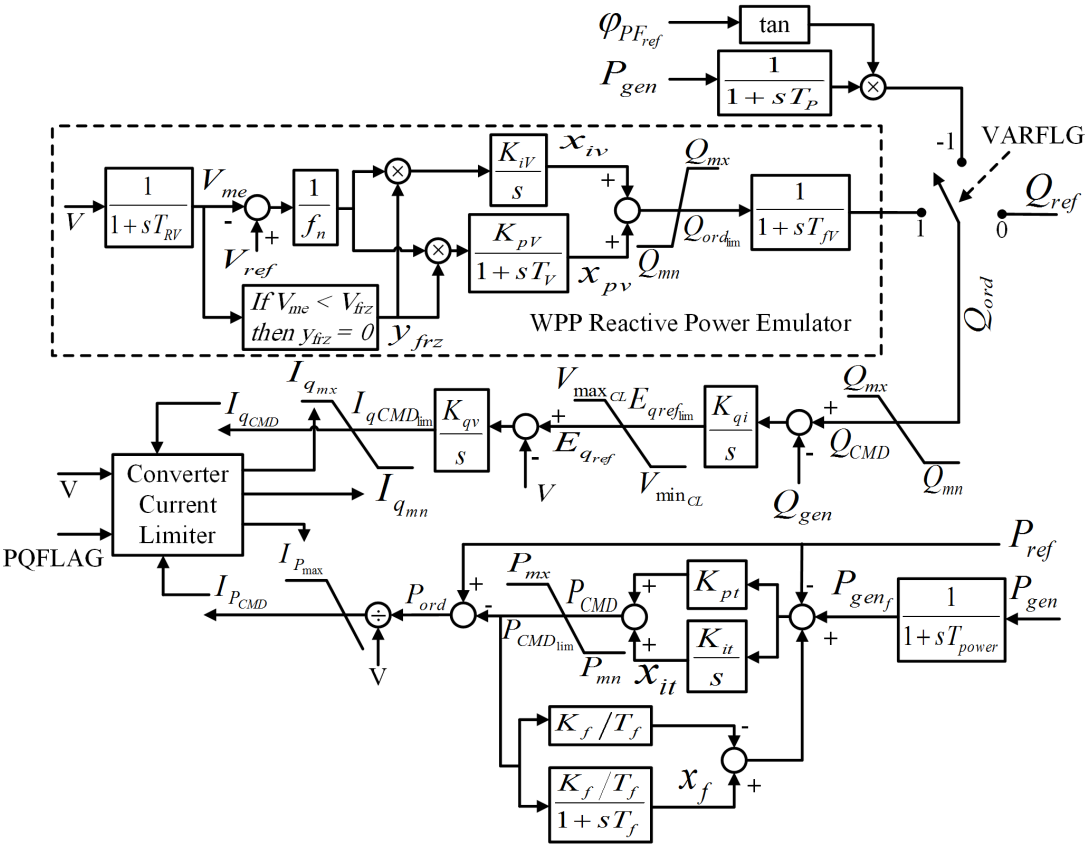

Figure 3.10: Type-4 WPP Converter Control Model

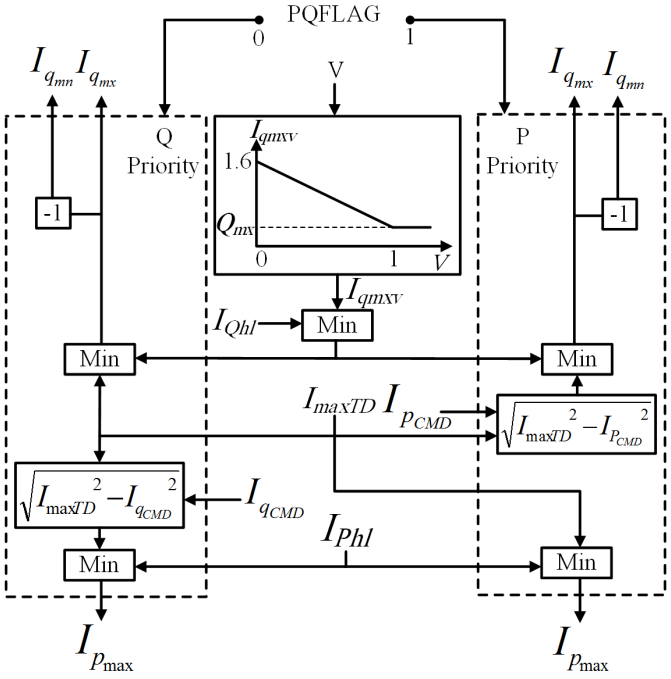

Figure 3.11: Type-4 WPP Converter Current Limiter Logic

ii. Not considering the reactive power control path.

iii. Lack of consistency between the results of the nonlinear generic model and the PSS/E-software built-in model.

No studies are reported in the technical literature that discusses development of linearized models based on the equivalent models of Type-4 WPP. This section develops the linearized models of Type-3 and Type-4 WPPs from their corresponding enhanced nonlinear models of Section 3.2 and Section 3.3. For Type-3 WPP, first the procedure to determine the steady-state operating point is discussed since it impacts the linearized model.

3.4.1 Operating Point Determination for Type-3 WPP Model

The operating point is determined based on the system power flow results and by setting the time-derivates in (3.1)–(3.46) to zero. Equations (3.21) and (3.40) conclude ω-$\omega_{ref} = 0$. In a normal operating condition, the terminal voltage is within the freezing voltage (V_{frz}) and the overvoltage limit (V_{LIM}) thresholds, and the injected active and reactive powers are within their respective limits. Therefore, the limits of the generator/converter and the converter control models are non-binding. However, in the case of pitch control, the limits may be enforced when the wind power is less than or equal to the WPP rating. In such a case, the pitch angle is at its lower limit to maximize the extracted power. Moreover, the value of the discrete variables associated with the blocking logics must be consistent with the system operating point. This results in an undefined value for θ_{CMD} and consequently it can be assumed that

$$\theta_o = \theta^+_{min} \tag{3.58}$$

Based on the initial value of P_{ord}, i.e., ${P_{ord}}^{(o)}$, there are three scenarios for the pitch angle compensation integrator of Figure 3.6:

i. ${P_{ord}}^{(o)} > P_{ref}$: The integrator is fed by a positive signal and the associated limiter does not include an upper limit. Thus, equilibrium is not achieved which leads to the failure of determining the operating point.

ii. ${P_{ord}}^{(o)} < P_{ref}$: The integrator is fed by a negative signal and its output (x_c) is forced to the lower limit of the associated limiter, thus ${x_c}^{(o)} = 0$.

iii. ${P_{ord}}^{(o)} = P_{ref}$: In this case, ${x_c}^{(o)}$ can have any value greater than or equal to zero.

Table 3.2: Initial Values of Type-3 WPP Model Variables

Model Variable	Initial Value	Model Variable	Initial Value
$P_{gen}{}^{(o)}$, $Q_{gen}{}^{(o)}$ $V^{(o)}$, $\varphi^{(o)}$	Determined from the power flow study	$I_{P_{lim}}{}^{(o)} = I_p{}^{(o)}$ $I_{P_{CMD}}{}^{(o)} = I_{P_{LVPL}}{}^{(o)}$	$\frac{P_{gen}{}^{(o)}}{V^{(o)}}$
$I_{Q_{lim}}{}^{(o)} = I_Q{}^{(o)}$	$-\left(\frac{P_{gen}{}^{(o)}}{V^{(o)}} + \frac{V^{(o)}}{X_{eq}}\right)$	$E_{q_{CMD}}{}^{(o)}$	$-I_Q{}^{(o)} X_{eq}$
$\delta^{(o)}$	$\varphi^{(o)}$	$V_Y{}^{(o)}$	0
$V_{PLL_{lim}}{}^{(o)} = V_{PLL}{}^{(o)}$	0	$\Delta\delta_{lim}{}^{(o)} = \Delta\delta^{(o)}$	0
$\omega_{ref}{}^{(o)} = \omega^{(o)}$	$f(P_{gen}{}^{(o)})$	$V_{ref}{}^{(o)}$	$V^{(o)}$
$P_{ord_{lim}}{}^{(o)} = P_{ord}{}^{(o)}$ $P_{CMD}{}^{(o)}$	$I_{P_{CMD}}{}^{(o)}\ V^{(o)}\ \frac{S_{rated}}{P_{rated}}$	$Q_{ord_{lim}}{}^{(o)} = Q_{ord}{}^{(o)}$ $Q_{CMD}{}^{(o)}$	$Q_{gen}{}^{(o)}$
$x_{pv}{}^{(o)}$	0	$x_{iv}{}^{(o)}$	$Q_{ord_{lim}}{}^{(o)}$
$x_\omega{}^{(o)}$	$\frac{P_{CMD}{}^{(o)}}{\omega^{(o)}}$	$E_{qref}{}^{(o)} = E_{qref_{lim}}{}^{(o)}$	$V^{(o)}$
$E_{qCMD_{lim}}{}^{(o)}$	$E_{q_{CMD}}{}^{(o)}$	$\theta^{(o)} = \theta_{CMD}{}^{(o)}$	θ_{min}
$P_m{}^{(o)}$	$P_{gen}{}^{(o)} + D\omega^{(o)}$	$x_c{}^{(o)}$	0
$y_c{}^{(o)}$	1	$y_p{}^{(o)}$	1
$x_p{}^{(o)}$	$\theta_{CMD}{}^{(o)}$ - $K_{pc}(P_{ord}{}^{(o)}$-$P_{ref})$	$y_{frz}{}^{(o)}$	1

These three scenarios imply that

$$x_c^{(o)}\left(P_{ord}^{(o)} - P_{ref}\right) = 0, \tag{3.59}$$

has to be satisfied while determining the operating point. The initial values of Type-3 WPP model states are given in Table 3.2.

3.4.2 Type-3 WPP Small-Signal Dynamic (Linearized) Model

The model of Type-3 WPP is hybrid due to the switching logics associated with the limits of the controllers as discussed previously. Furthermore, the limits of the pitch-angle controller can be binding during the initialization process. These can violate the linearization assumptions where the dynamical system must remain smooth in the neighborhood of the equilibrium point. Therefore, depending on the equilibrium point adopted for linearization, the eigenstructure necessarily is not unique. The model of Type-3 WPP, i.e., (3.1)–(3.46), can be written as

$$\dot{x} = f\left(x,\ Y,\ u\right), \tag{3.60}$$

$$0 = g\left(x,\ Y,\ u\right), \tag{3.61}$$

where

$$Y = \begin{bmatrix} \varphi & V & I_d & I_q \end{bmatrix}^T, \quad u = \begin{bmatrix} V_{ref} & P_{ref} \end{bmatrix}^T \text{ and}$$

$$x = \begin{bmatrix} I_Q & I_{P_{LVPL}} & V_m & V_{PLL} & \delta & \omega_{ref} & x_\omega & P_{ord_{lim}} & V_{m_e} \\ & x_{iv} & x_{pv} & Q_{ord} & E_{q_{ref_{lim}}} & E_{q_{CMD_{lim}}} & \omega & x_p & x_{c_{lim}} & \theta_{lim} \end{bmatrix}^T.$$

Linearizing (3.60) and (3.61) results in

$$\Delta\dot{x} = [a_{ij}]\,\Delta x + [b_{ij}]\,\Delta u + [h_{ij}]\,\Delta Y, \tag{3.62}$$

$$0 = [l_{ij}]\,\Delta x + [m_{ij}]\,\Delta u + [n_{ij}]\,\Delta Y, \tag{3.63}$$

for which (i) the non-zero elements are given in Appendix A and (ii) the algebraic variables can be eliminated when the WPP linearized model is included in the system linearized model of Chapter 2. The linearized model of a Type-3 WPP can have up to eight eigenstructures since it contains three discrete variables y_{frz}, y_c, and y_p. However, in a normal operating condition, y_{frz} is always 1 which decreases the number to four.

It should be noted that the initial value of the pitch angle highly affects the linearized model of Type-3 WPP. For example, if $\theta_o = 0$, the pitch-angle controller will be decoupled from the wind turbine. The reason is that the simplified aerodynamics model will not affect the turbine speed and consequently perturbations in the pitch-angle do not affect the turbine speed. Moreover; if the pitch compensation integrator state (x_c) is blocked during initialization, x_c is eliminated from the state vector.

Furthermore, it should be noted that the eigenstructure of Type-3 WPP always contains a single zero- eigenvalue since (3.21) and (3.40) constitute double integrators. This is reflected as two linearly-dependent rows in $[a_{ij}]$ of (3.62). However, the participations of different states in the corresponding eigenvector depend on the initial value of the pitch-angle [4]. In contrast to [4], the linearized model does not experience the scenario where the eigenstructure includes two zero-eigenvalues. The reason of this discrepancy is that reference [4] neglects the dynamics of generator/converter model which result in $P_{ord_{lim}} = P_{gen}$. This implies that the turbine speed (ω) is influenced by $P_{ord_{lim}}$ instead of P_{gen}. This in turn results in two linearly-dependent rows corresponding to ω and $x_{c_{lim}}$ when $\theta_o = 0$. However; when the generator/converter model is considered, the dynamics of the active current ($I_{P_{LVPL}}$) result in linear independency of ω and $x_{c_{lim}}$ states and thus a single zero-eigenvalue.

Finally, based on the data of $f(P_{gen})$ in (3.20) and the operating conditions, the reference speed is not affected by perturbations in P_{gen}. The reason is that the WPP

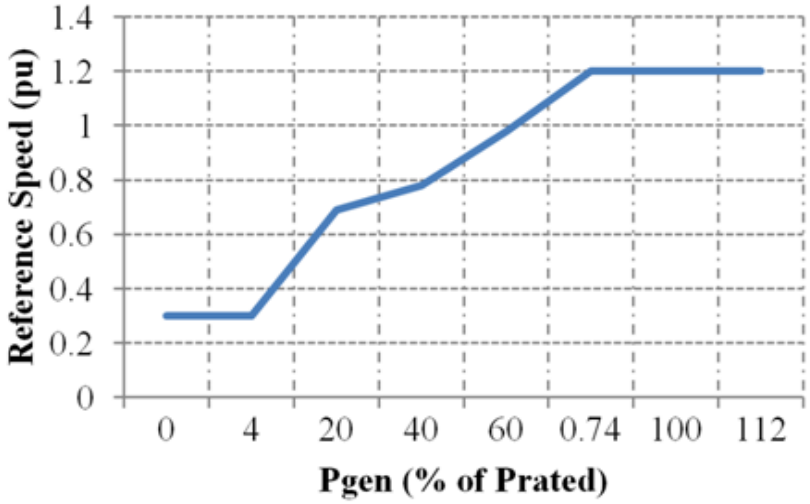

Figure 3.12: Generated Active Power - Reference Speed characteristics ($f(P_{gen})$) of Type-3 WPP

operates near its rated capacity and $f(P_{gen})$ provides a constant reference speed in the range of $0.74 \leq P_{gen} \leq 1.12$ pu, as shown in Figure 3.12. Therefore, the linear dynamics of ω_{ref} is influenced only by the low-pass filter time-constant (T_{power}).

3.4.3 Type-4 WPP Small-Signal Dynamic (Linearized) Model

Exploiting the similarities between the dynamic models of Type-3 and Type-4 WPPs, this sub-section relies on the developments of the previous one and only describes the differences of the Type-4 WPP linearized model as compared with that of the Type-3 WPP. The salient difference is the uniqueness of the eigenstructure of Type-4 WPP linear model since there are no switching logics associated with any limits as is the case for Type-3 WPP. Furthermore, the impact of the current limiter in the converter controller model does not appear in the linearized model. However, this limiter and the generator/converter model limits impact the response of the non-linear dynamic model. Finally, in contrast to Type-3 WPP, the linearized model for Type-4 WPP does not include a zero-eigenvalue.

3.5 Conclusions

This chapter presents enhanced (nonlinear) generic models of Type-3 and Type-4 WPPs. These models are hybrid due to the interaction of the continuous states with discrete

logics. The enhancements include (i) generator active current command recalculation step for Type-3 WPPs and (ii) a freezing function to the WPP reactive power emulator for Type-3 and Type-4 WPPs. This chapter also elaborates on the active power control logic which is not required but implemented in one version of the generic models, i.e., reference [4]. The main feature of the enhanced models is that they can replicate the field-verified responses of the built-in PSS/E-software models in any adopted software platform. It should be noted that the generic models described in the technical literature do not necessarily provide such replications, as will be shown in Chapter 4. Chapter 4 validates the response of the developed enhanced generic models against the PSS/E-software built-in models and also shows limitations of the previously documented models in this regard.

This chapter also develops linearized models of Type-3 and Type-4 WPPs from the enhanced generic models. In addition, it provides a detailed discussion of the multiple eigenstructure of Type-3 WPP and the single structure of Type-4 WPP linear models. This chapter clarifies that the linear model of Type-3 WPP cannot include two zero-eigenvalues as reported in the technical literature. It also emphasizes that different limits implemented in the model of Type-4 WPP significantly impact its dynamic response. Chapter 4 validates the accuracy of the developed WPPs linearized models through comparing their time-responses against those of the corresponding nonlinear models when subjected to small-signal disturbances.

Chapter 4

Wind Power Plant Model Validation

4.1 Introduction

This chapter evaluates and validates dynamic performance of the enhanced generic models of Type-3 and Type-4 WPPs that were developed and presented in Chapter 3. The validation is primarily based on comparing the time-domain responses of the developed, nonlinear, enhanced models, obtained from MATLAB/Simulink software platform, with those of the PSS/E-software built-in models which have been validated against field measurements [27].

In addition to comparison with the PSS/E-software built-in model time-response, the simulation results of the developed enhanced model of Type-3 WPP are also compared with those of the model (i) described in PSS/E [28] and WECC [22] documentations, and (ii) investigated in [4]. The comparisons demonstrate that only the developed enhanced model is capable of reproducing the response of the PSS/E-software built-in model. This chapter also compares the time-domain response of the developed Type-4 WPP model with those of models described in the PSS/E [28] and WECC [23] documentations which are the only available technical literature discussing the Type-4 WPP generic model. The comparisons show that the previously documented models are either omitting or adding parts that are not integral parts of the generic models.

Finally, the extracted linear models of Type-3 and Type-4 WPPs are validated against the time-responses of their non-linear enhanced models under small-signal disturbance scenarios. The linearized and the nonlinear WPPs models are used to identify the impacts of high-depth of wind power penetration on the low-frequency oscillations and transient stability of System-1, respectively, as presented in Chapter 5.

4.2 Large-Signal Dynamics - Type-3 WPP

The purpose of the reported studies in this section is to evaluate and verify the Type-3 enhanced model (hereafter referred to as Type-3-E) of Chapter 3. The Type-3-E represents a 990-MW, 0.575-kV, Type-3 WPP which is connected to Bus-59 of System-1 through a 0.575/345 kV, 1102.2-MVA transformer and accounts for 5% depth of wind power penetration. The WPP is composed of 660 WTG units each at 1.5 MW [28]. The WPP parameters are given in Appendix B. The performance of Type-3-E is also compared with those of:

i. The PSS/E-software built-in Type-3 WPP model which hereafter is referred to as Type-3-PSSE1. This is done by comparing the non-linear system response using the PSS/E-software for time-domain simulation.

ii. The Type-3 WPP model described in the PSS/E [28] and the WECC [22] documentations and hereafter is referred to as Type-3-PSSE2.

iii. The Type-3 WPP model of [4] and hereafter referred to as Type-3-H.

4.2.1 Fault close to the WPP terminal

Initially System-1 is in a steady-state condition and the WPP delivers 988-MW to the system at Bus-59. At t=1s, System-1 is subjected to a 5-cycle, temporary self-cleared L-L-L-G fault at Bus-60. Figure 4.1 shows the WPP time response to the fault obtained from Type-3-E (in Matlab platform) and the Type-3-PSSE1 (in the PSS/E platform). Close agreement between the corresponding results (i) verifies accuracy of the enhanced model (Type-3-E) and (ii) indicates the presence of the freezing function in the WPP reactive power emulator in both Type-3-E and Type-3-PSSE1. The effect of neglecting the freezing function is shown in the next section. Figure 4.1(d) shows the effect of the switching logics in the pitch-angle control that results in (i) switching deadlock response and (ii) evolution of the system to a new post-fault steady-state [4].

4.2.2 Fault at a remote bus

The initial conditions and the fault are identical to those of the previous case except the fault occurs at Bus-53 which is electrically remote from the WPP. Figure 4.2 shows the system response to the fault. The disturbance results in insignificant speed deviation, Figure 4.2(c), and pitch angle deviations, Figure 4.2(d). Figure 4.2(a) shows that injected active power is restored to the pre-fault value in about 200 ms. However, the reactive

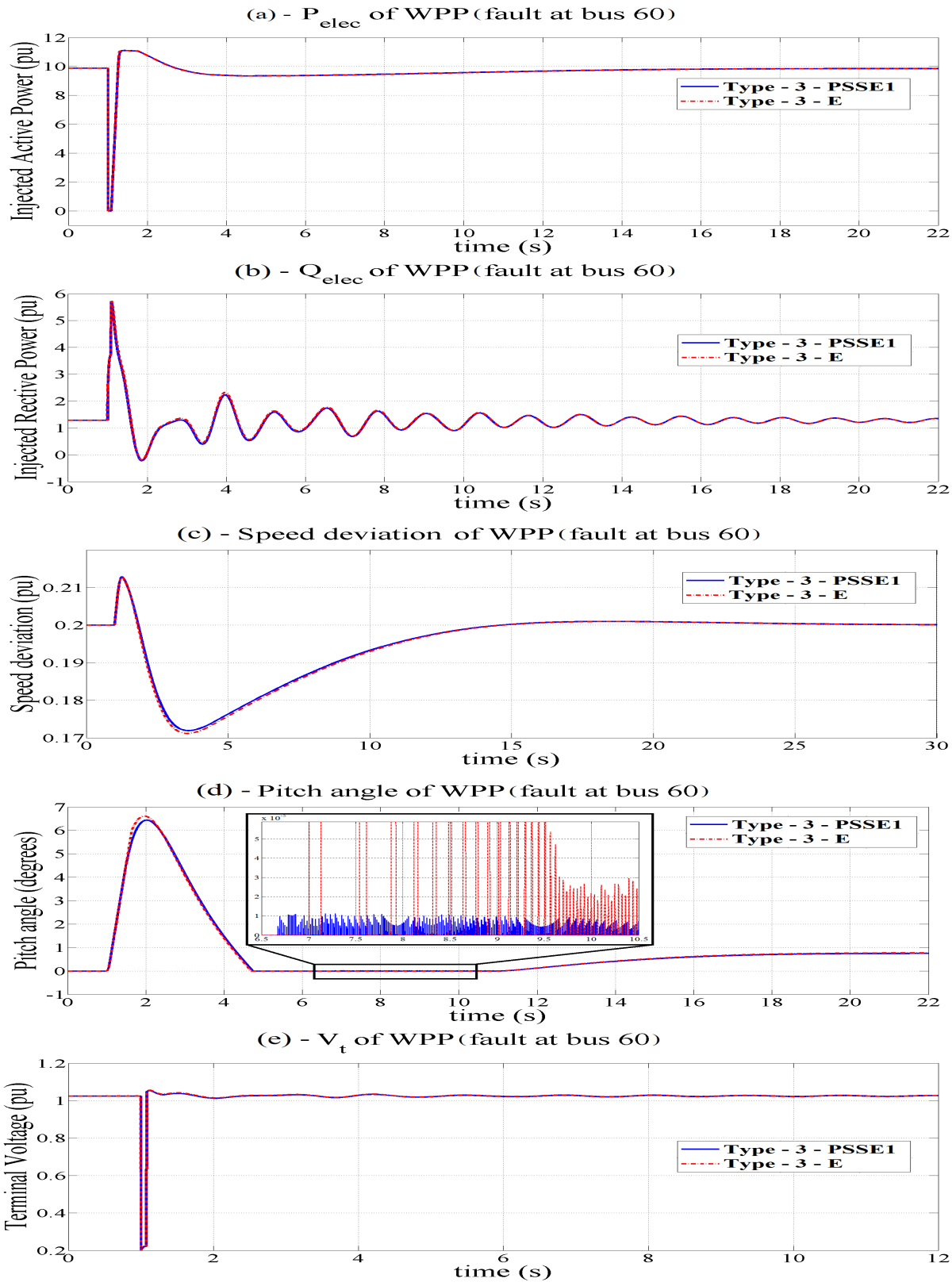

Figure 4.1: Type-3 WPP response to a fault close to the terminal bus for developed enhanced model (Type-3-E) and PSS/E platform built-in model (Type-3-PSSE1)

power shows sustained oscillations, Figure 4.2(b). This indicates the parameters of the reactive power control stream can be further tuned to achieve an improved response. However, this is out of scope of this work and the parameters are adopted as suggested by [28]. The simulation results of Figure 4.2 also verify that Type-3-E and Type-3-PSSE1 are the same and reproduce identical results. It should be noted that some of the details of Type-3-PSSE2 are described in neither the PSS/E documentation [28] nor the WECC modeling guidelines [22, 27].

4.3 Comparisons with Other Type-3 WPP Models

4.3.1 Comparison with Type-3-H

Type-3-H does not include (i) the generator/converter model and (ii) the reactive power control path of Figure 3.4. To provide a meaningful comparison, Type-3-H is augmented with the models of (i) and (ii) as given in Figure 3.2 and Figure 3.4, respectively. Type-3-H differs from Type-3-E by (i) addition of a switching logic to the PI-controller of the active power control path and (ii) derivation of active power control based on the rated apparent power of the WPP. Figure 4.3 and Figure 4.4 show the time-response of the two models to the fault scenarios of the study cases of Figure 4.1 and Figure 4.2, respectively.

Figure 4.3 illustrates that the injected reactive power and the terminal voltage responses of the two models closely match. The reasons are that (i) the generator/converter model and the reactive power control path are adopted from Type-3-E and (ii) the active and reactive power control streams are decoupled in the generic model. Therefore, the changes introduced in the active power control stream have minimal impact on the injected reactive power and consequently on the terminal voltage. However, the injected active power, speed deviation, and pitch angle of the two models are noticeably different for a fault either close to, Figure 4.3, or electrically remote from, Figure 4.4, the WPP terminal bus. The main reason for the discrepancies in the pitch angle and speed deviation responses is the difference in the active power injection by Type-3-E and Type-3-H.

The source of the discrepancy in the active power response is different for the two faults considered. For the fault close to the WPP terminal bus, derivation of active power control based on the rated apparent power of the WPP, is the reason for the discrepancy where longer times are required to reach steady-state values. However, for the electrically remote fault, the added switching logic to Type-3-H is the source of the discrepancy, especially during the fault period, Figure 4.4(a). During the fault period, the impact of the added switching logic is observable in the Type-3-H response. This

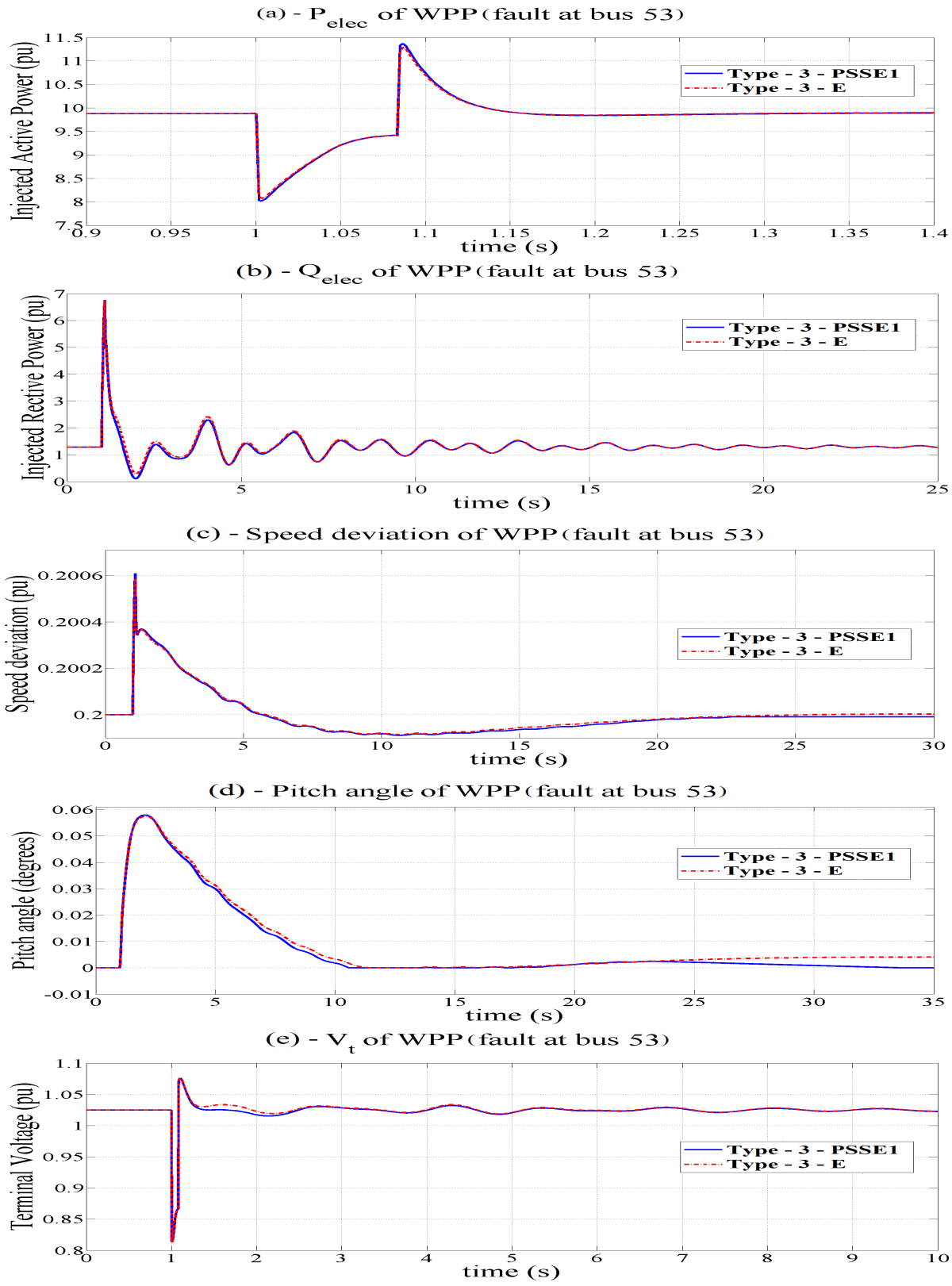

Figure 4.2: Type-3 WPP response to a fault at a remote bus for developed enhanced model (Type-3-E) and PSS/E platform built-in model (Type-3-PSSE1)

effect is not detected in the response of either Type-3-E or Type-3-PSSE1. The compared results show that Type-3-H cannot be used to replicate the field verified time responses of Type-3-PSSE1.

4.3.2 Comparison with Type-3-PSSE2

This model is not the same as the developed Type-3-E model since it (i) neglects all the switching logics associated with the pitch-angle control, (ii) neglects the freezing function of the reactive power emulator, and (iii) derives the active power control based on the rated apparent power of the WPP. Figure 4.5 compares the time-responses of Type-3-E and Type-3-PSSE2 to the fault scenario of Figure 4.1 where both models are simulated in the Matlab platform. The reasons for the differences in the responses are:

- Reactive power and terminal voltage: neglecting the freezing function results in rapid saturation of the reactive power emulator integrators after the fault clearing.
- Active power and turbine speed: derivation of active power control based on the rated apparent power of the WPP results in the discrepancy.
- Pitch angle: neglecting the switching logics results in a response which is free from any switching deadlocks. In addition, the final steady-state value of Type-3-PSSE2 pitch angle is significantly different from that of Type-3-E.

4.4 Large-Signal Dynamics Type-4 WPP

Case studies similar to those reported for Type-3 WPP are also conducted for validation of the developed Type-4 WPP enhanced non-linear model which is hereafter referred to as Type-4-E. The Type-4 based WPP is a 500-MW plant (corresponding to 2.5% depth of wind power penetration) which is composed of 200 units of 2.5-MW and 0.575-kV [28], connected through a 0.575/345-kV, 600-MVA transformer to System-1 at Bus-59. The WPP parameters are given in Appendix B. Similar to Type-3-E in Section 4.2, the performance of Type-4-E is compared with those of:

i. The PSS/E-software built-in Type-4 WPP model which hereafter is referred to as Type-4-PSSE1.

ii. The Type-4 WPP model described in the PSS/E [28] and the WECC [23] documentations and hereafter is referred to as Type-4-PSSE2.

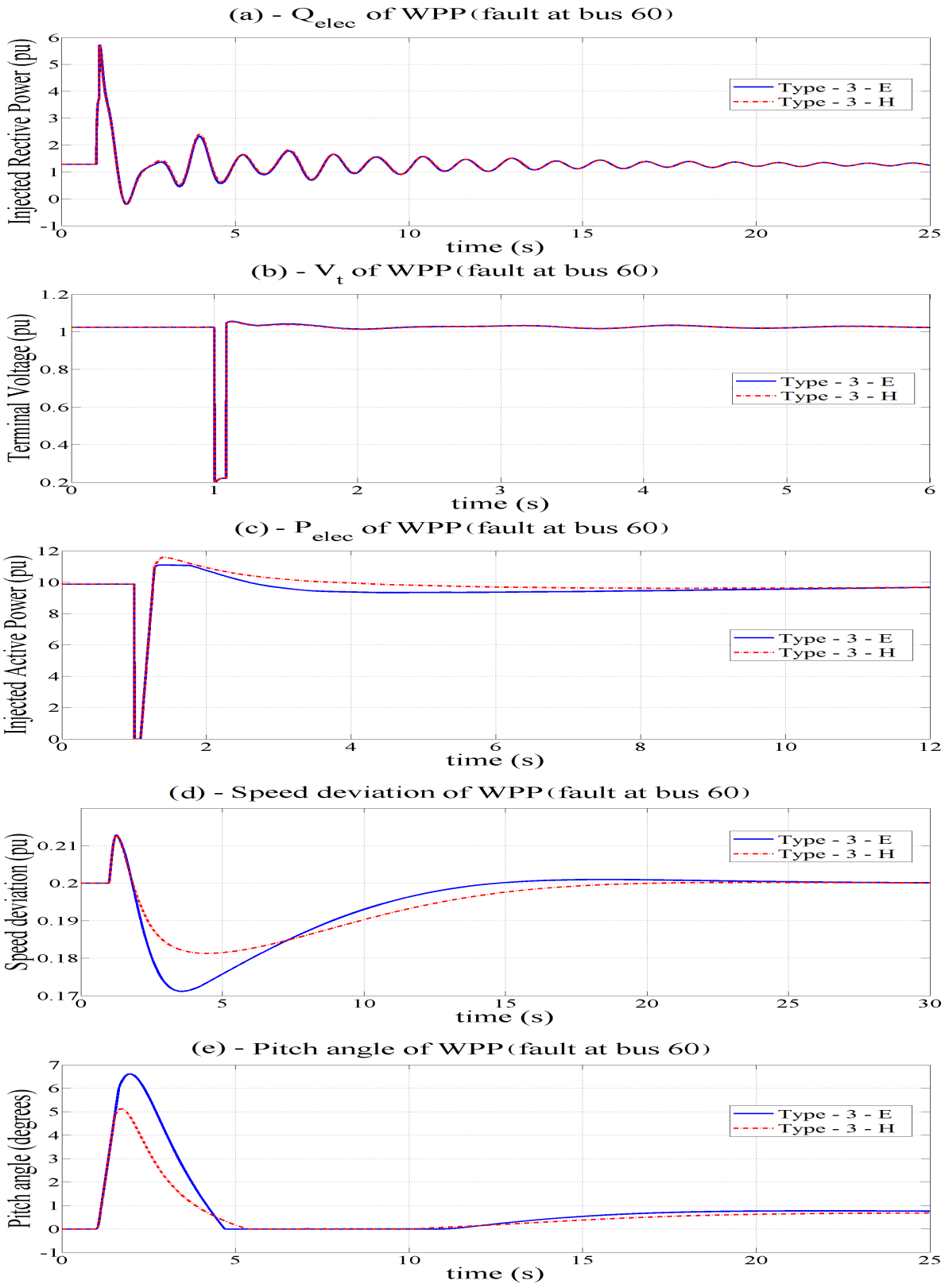

Figure 4.3: Type-3 WPP response to a fault close to the terminal bus for developed enhanced model (Type-3-E) and WPP model presented in [4] (Type-3-H)

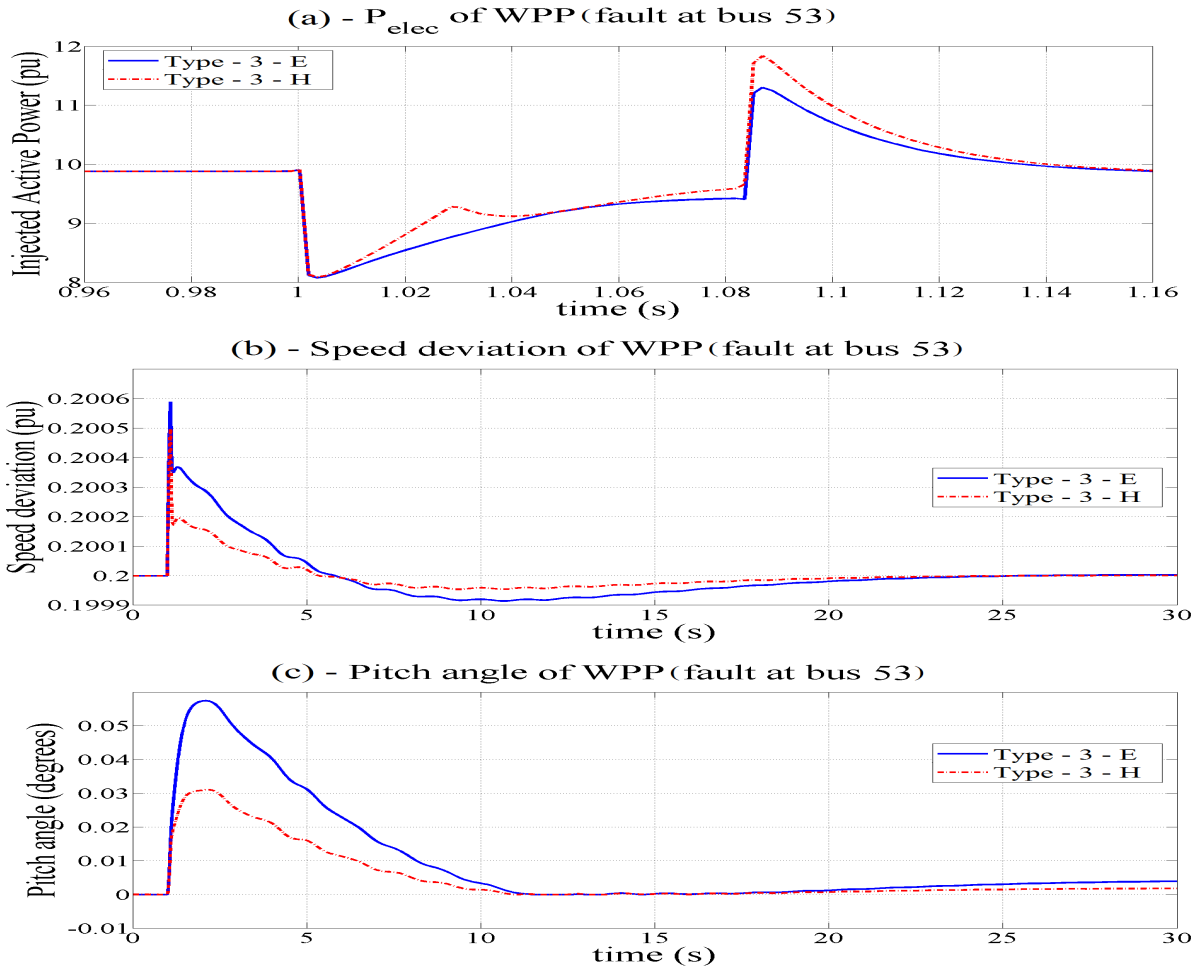

Figure 4.4: Type-3 WPP response to a fault at a remote bus for developed enhanced model (Type-3-E) and WPP model presented in [4] (Type-3-H)

4.4.1 Developed Enhanced Model Validation

The same faults of Figure 4.1 (fault close to the WPP terminal bus) and Figure 4.2 (fault at an electrically remote bus) are applied for validation of Type-4-E. Figure 4.6 and Figure 4.7 show the WPP time-responses to the faults obtained from Type-4-E (in Matlab platform) and Type-4-PSSE1 (in the PSS/E platform). Figure 4.6 and Figure 4.7 show that Type-4-E closely captures all the details of the PSS/E-software built-in model, i.e., Type-4-PSSE1, indicating that both models are the same. Figure 4.1 - Figure 4.2 (Type-3 WPP) and Figure 4.6 - Figure 4.7 (Type-4 WPP) conclude:

- Both WPP types have fast active power control responses which are mainly influenced by the active current ramp rate limit (R_{ip}).

- The reactive power response of Type-4 WPP is faster than that of Type-3 WPP and

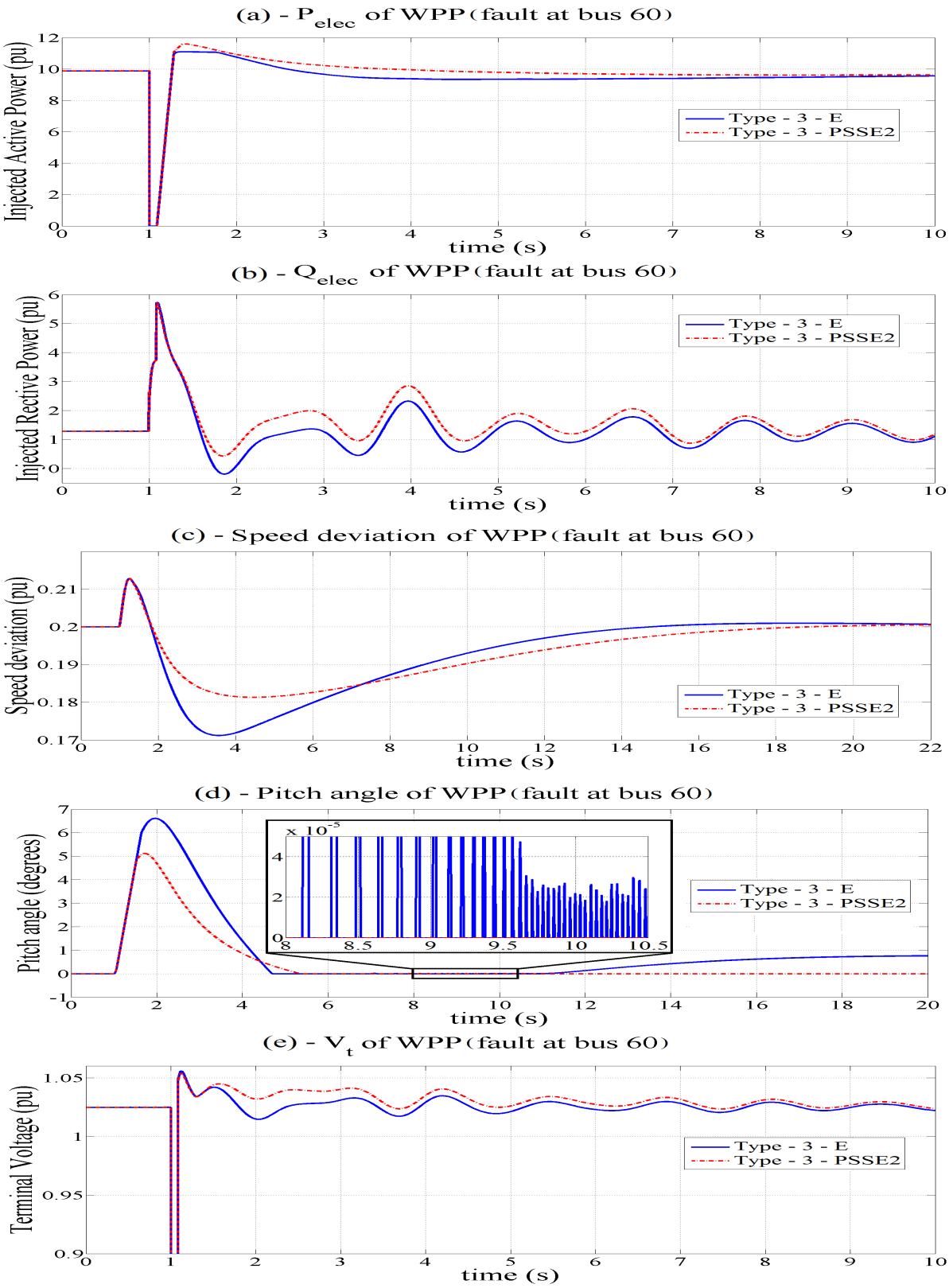

Figure 4.5: Type-3 WPP response to a fault close to the terminal bus for developed enhanced model (Type-3-E) and PSS/E and WECC documented model (Type-3-PSSE2)

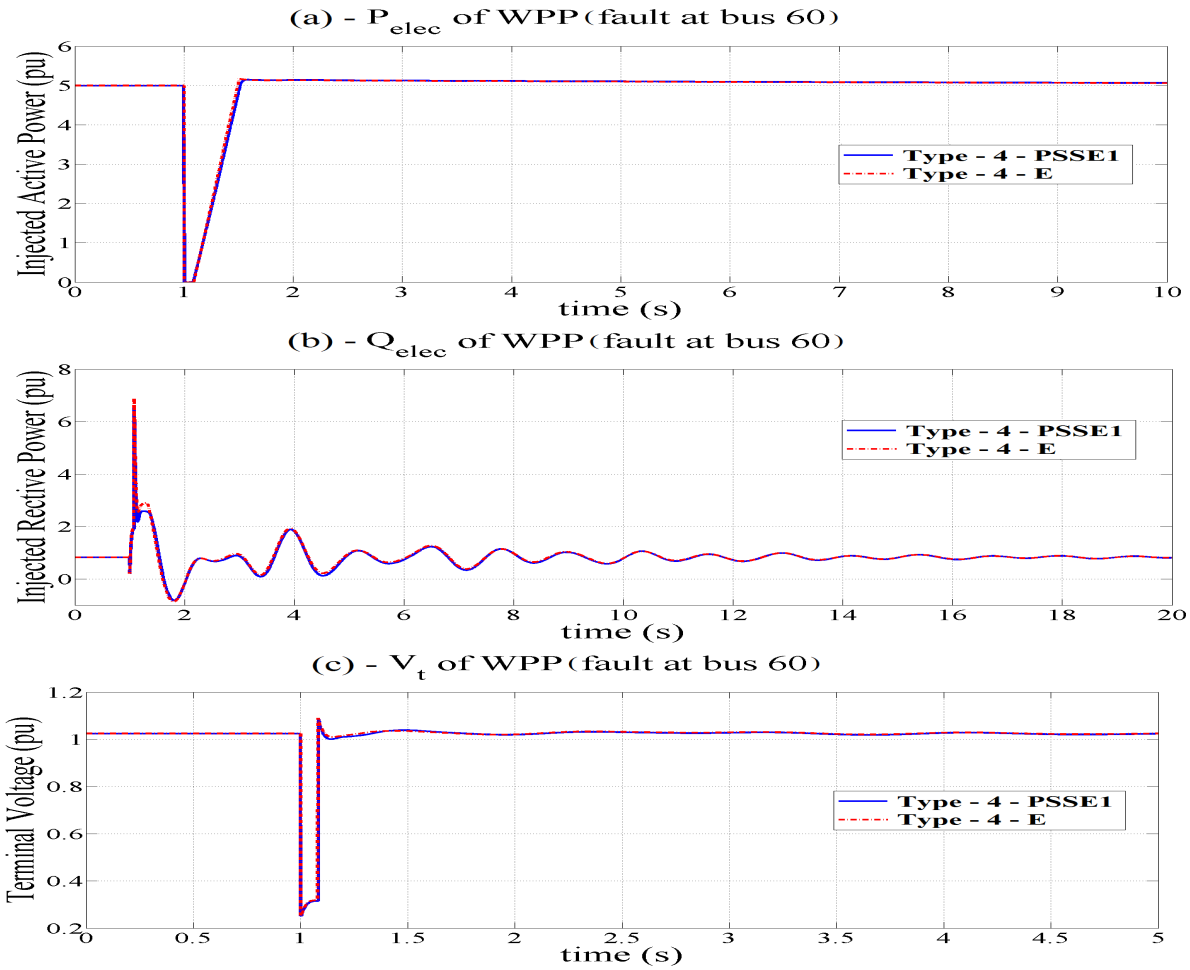

Figure 4.6: Type-4 WPP response to a fault close to the terminal bus for developed enhanced model (Type-4-E) and PSS/E platform built-in model (Type-4-PSSE1)

consequently the oscillations are damped faster. However, this fast response results in a high spike in the reactive power response that reaches 7 times the steady-state value. This spike vanishes rapidly and the overshoot is nearly 1.5 times the steady state value.

4.4.2 Comparison with Type-4-PSSE2

For this comparison, the fault scenario of Figure 4.6 is considered and the time-response of the system is shown in Figure 4.8. In contrast to the results of the case that compares Type-3-E with Type-3-PSSE2, i.e., Figure 4.5, the active power response of Type-4-PSSE2 is identical to that of Type-4-E. The reason is that active power control of Type-4 WPP is derived based on the apparent power of the WPP which is not the same for Type-3 WPP. Moreover, the active and reactive power control paths are coupled only through

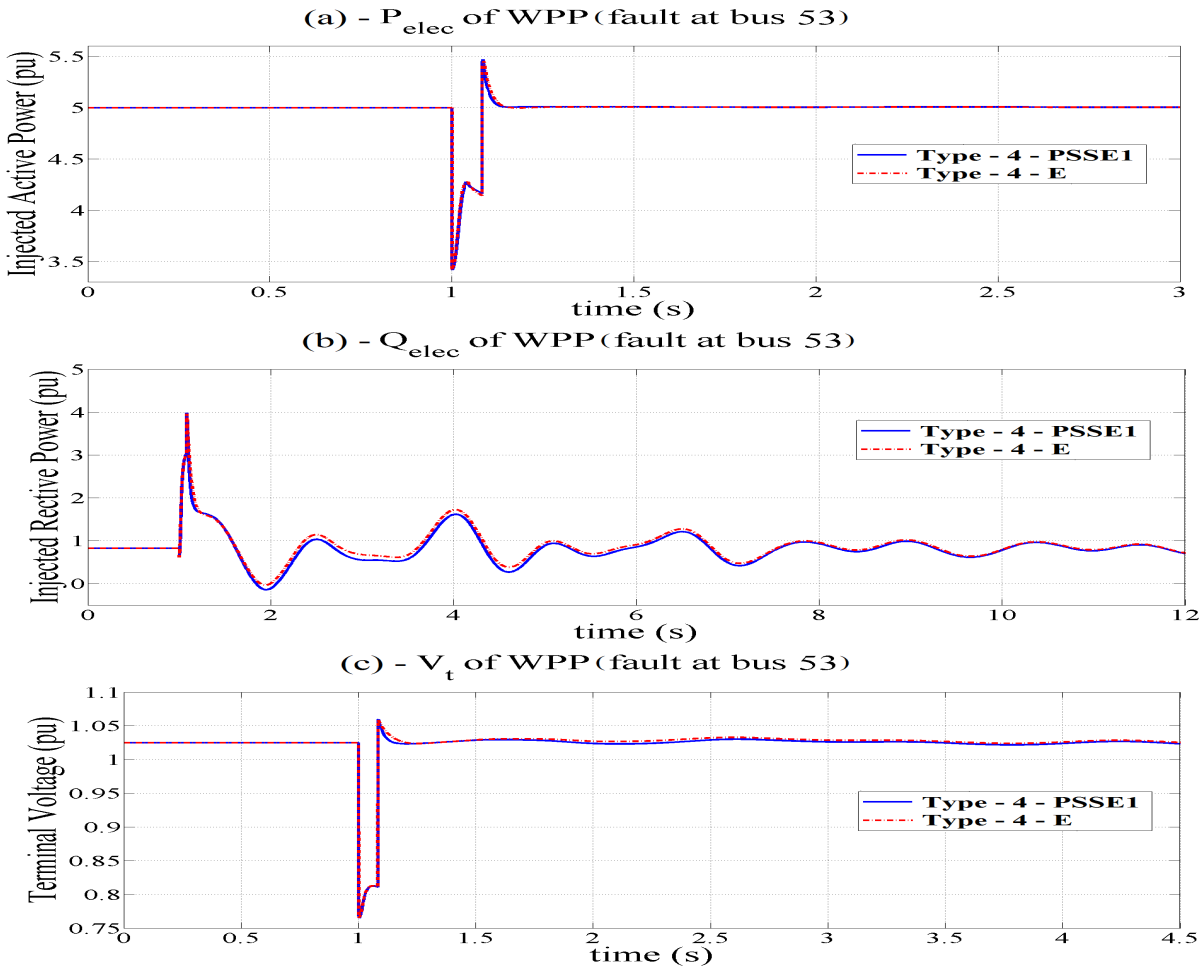

Figure 4.7: Type-4 WPP response to a fault at a remote bus for developed enhanced model (Type-4-E) and PSS/E platform built-in model (Type-4-PSSE1)

the converter current limiter logic as given in Figure 3.10. The coupling introduces insignificant mutual impacts on the active and reactive power control paths. Therefore, the discrepancy in the reactive power responses does not affect the active power responses. The source of discrepancy in the reactive power response of Figure 4.8(b) is the saturation of the reactive power emulator integrators due to the lack of freezing function. For Type-4 based WPP model, the deviation of Type-4-PSSE2 response from that of Type-4-E is significantly less than the deviation in the case of the Type-3 WPP (Type-3-E and Type-3-PSSE2).

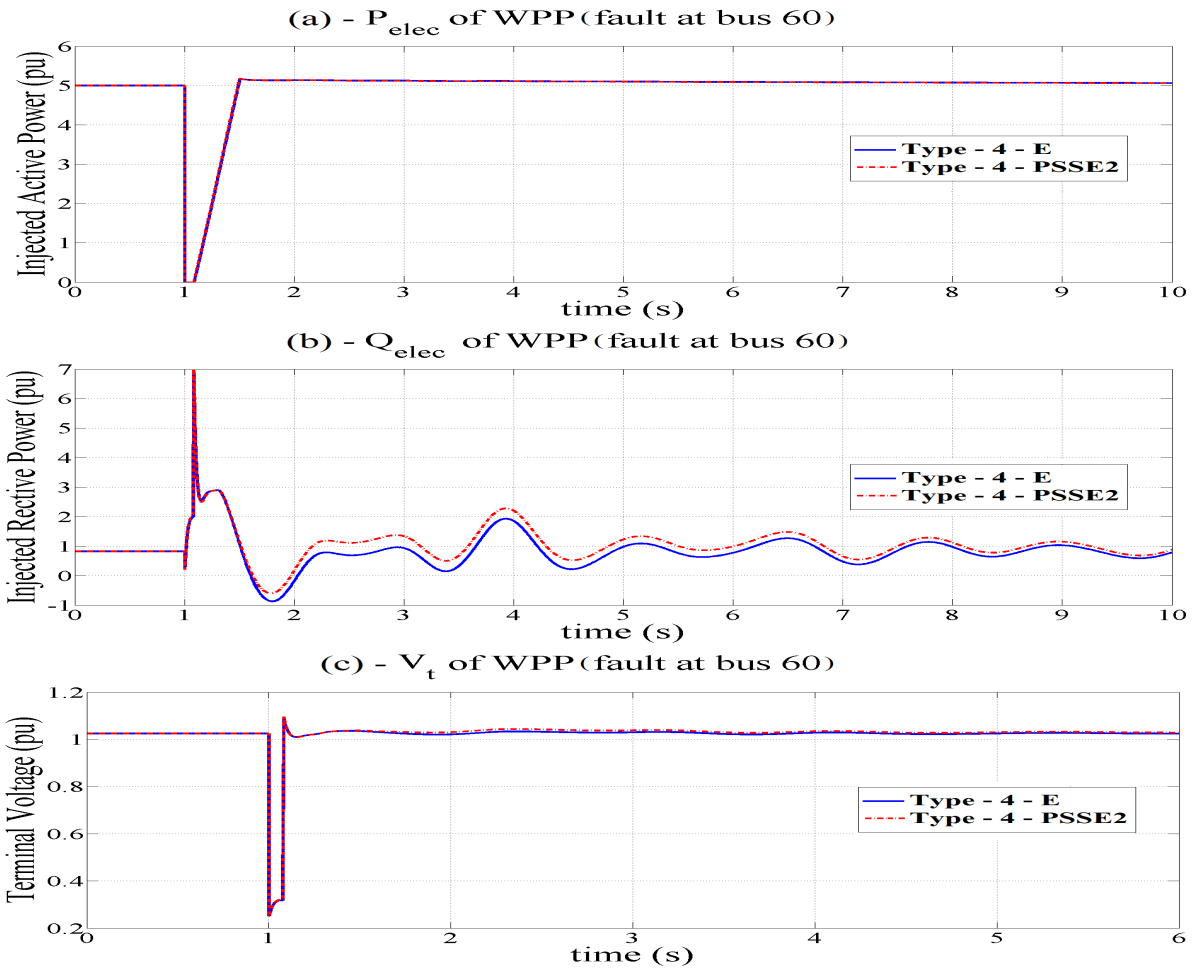

Figure 4.8: Type-4 WPP response to a fault close to the terminal bus for developed enhanced model (Type-4-E) and PSS/E and WECC documented model (Type-4-PSSE2)

4.5 Linearized Model Validation

This section investigates performance of the linearized models, Section 3.4, extracted from the developed enhanced generic models of Type-3 and Type-4 WPPs. In addition, this section validates the accuracy of the linearized models by comparing their responses against those of the corresponding non-linear models in the Matlab platform, when subjected to small-signal disturbances. The case reported in this section corresponds to a disturbance which is 5% increase in the reference voltage of the converter controller for 40 msec. The disturbance is selected such that none of the limits of the non-linear models is activated. Therefore, the assumption of linearity remains valid.

System-2, Figure 4.9, is used for performance evaluation and validation of the developed linearized models. It is composed of a WPP which is connected to a large system through two 345-kV lines. The system parameters are given in Appendix C. The reason

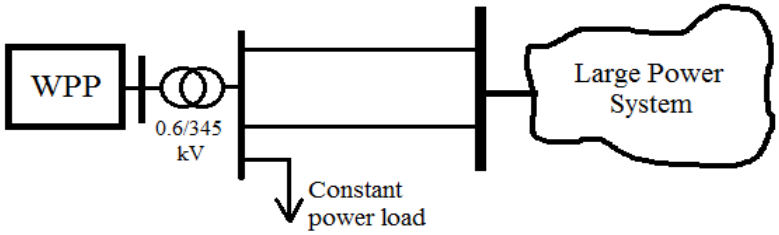

Figure 4.9: A schematic diagram of System-2

for using System-2, rather than System-1, is that it can easily demonstrate impact of the WPP linear model attributes on the small-signal dynamics while such details are not readily observable from the System-1 behavior. For example, the impact of a small disturbance on the non-linear system response can be observed due to the small size of System-2. Therefore, the linearized and non-linear system responses can be compared. In addition, System-2 is limited to a single WPP feeding a single load. Therefore, the linearized system only contains the WPP model states and thus the WPP eigenstructure characteristics of Chapter 3 can be examined.

4.5.1 Type-3 WPP linearized model validation

As discussed in Section 3.4.2, linearization for Type-3 WPP is dependent on the system initial (pre-disturbance) operating point. The reason is that the pitch-angle control is highly non-linear due to its hybrid nature. In the pitch-angle control of the developed enhanced model, two switching logics repeatedly change their states as the dynamical response evolves, as shown in Figure 4.1(d) and discussed in Chapter 3. The discrete change of variables associated with these logics dictates multiple consecutive piecewise linear models to determine the response. Furthermore, the switching logic can be activated, even if the disturbance is small and within the range of small-signal perturbations and thus multiple concatenated linearized models are required. However, if the operating point is determined under the assumption of zero pitch-angle, the pitch-angle control dynamics are decoupled and the non-linearities of the pitch-angle control can be neglected. This is the case when the extracted wind power is less than the rated MVA of the WPP. This is the only case where Type-3 WPP generic model provides a unique linear model, and the system response is shown in Figure 4.10. Under the aforementioned condition, no perturbation in the reference power affects the system due to the decoupled pitch-angle control. Therefore, any Automatic Generation Control (AGC)-like action that may be implemented for the WPP has to be investigated based on the non-linear model and not the linearized model.

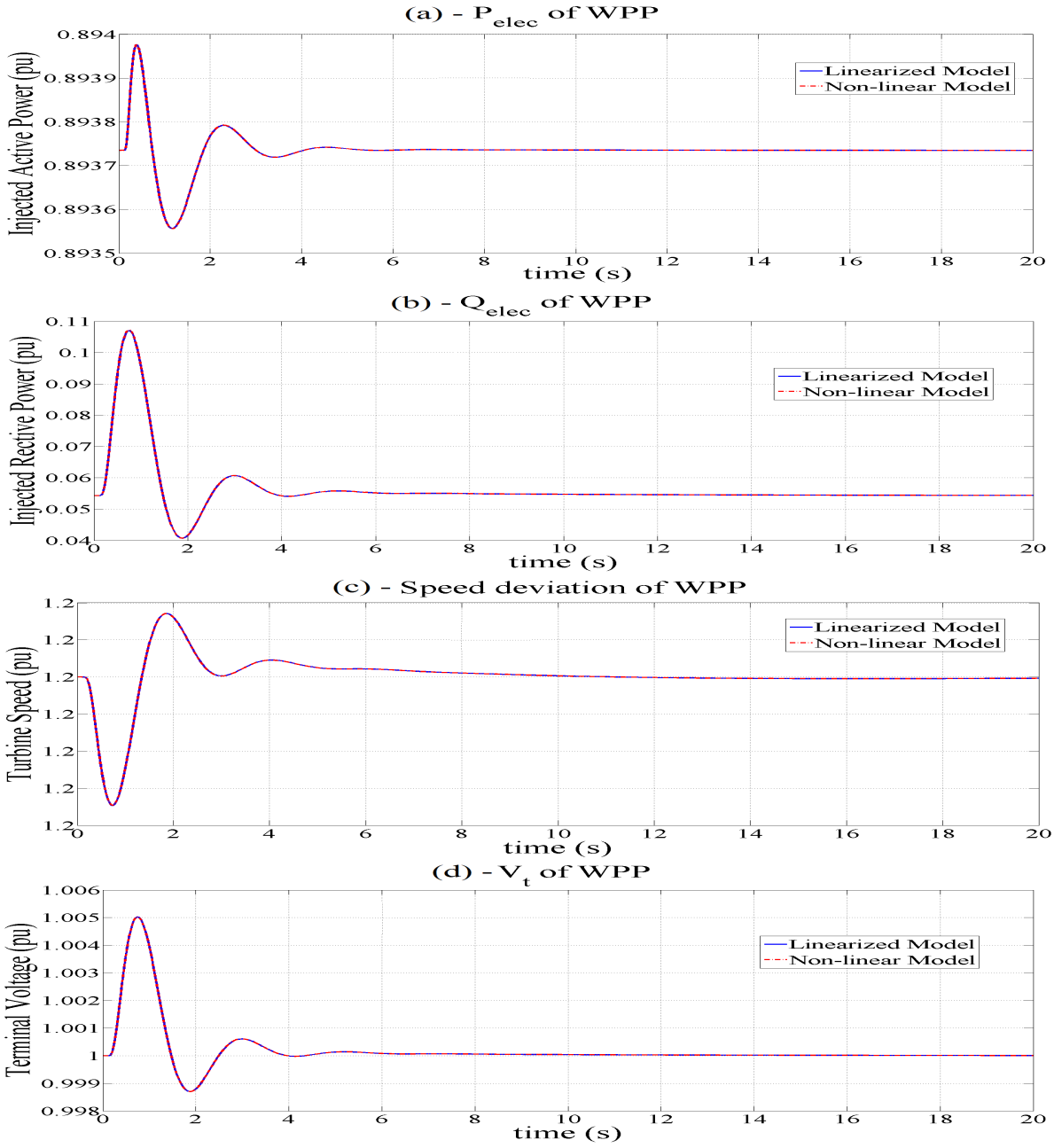

Figure 4.10: Type-3 WPP linearized model response

4.5.2 Type-4 WPP linearized model

In contrast to the Type-3 WPP model, Type-4 WPP has a unique linearized model. The reason is that the enhanced model of Type-4 WPP does not require switching logics as Type-3 WPP model does. Moreover, the freezing function of the reactive power emulator is activated when the terminal voltage is below the freezing threshold (V_{frz}). This threshold is fairly low (0.7 pu) such that small-signal disturbances do not activate it. Therefore,

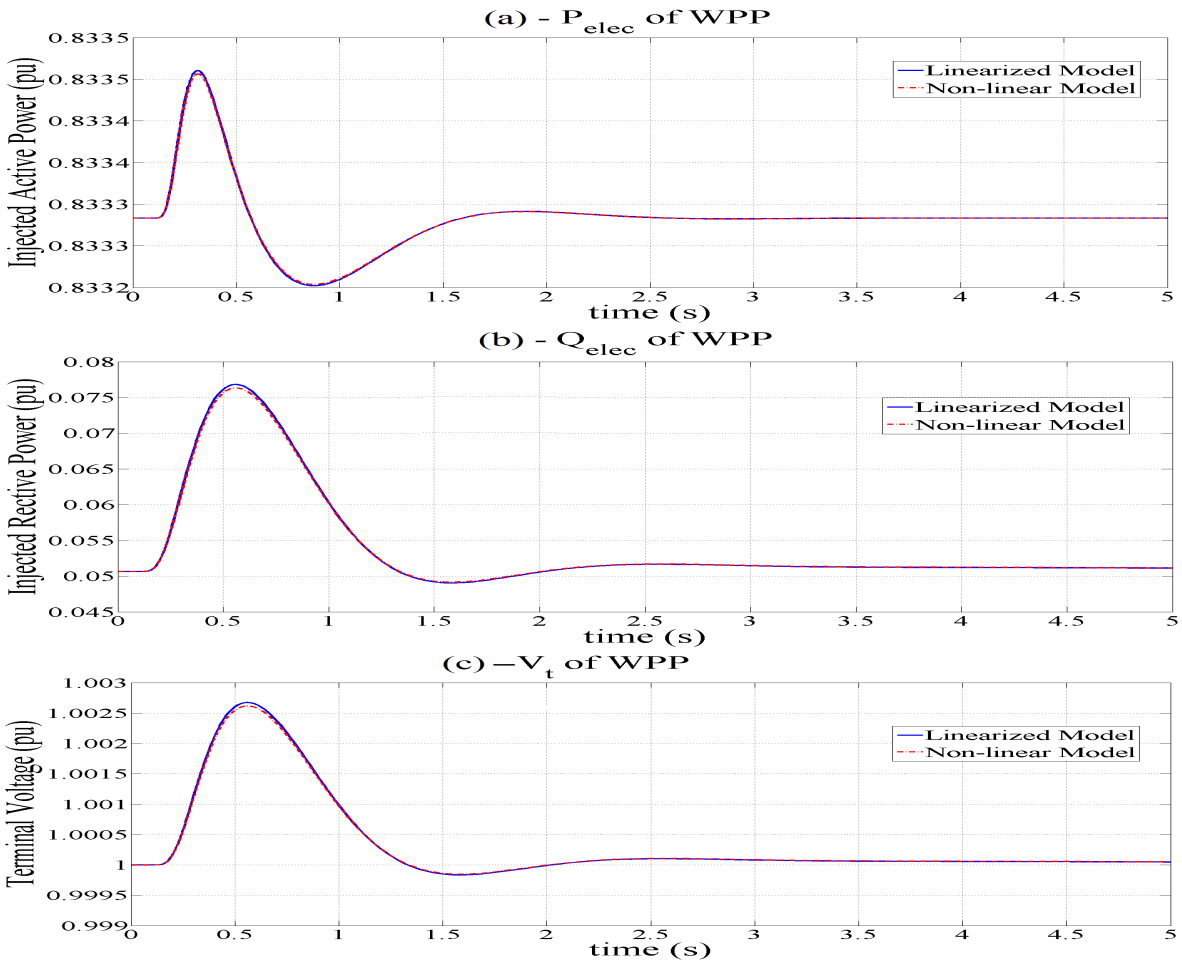

Figure 4.11: Type-4 WPP linearized model response

the freezing function action does not affect the linearized system response. Figure 4.11 compares the response of the Type-4 WPP linear model to its corresponding enhanced non-linear model to the disturbance of Figure 4.10. The closely matching responses of Figure 4.11 indicate that the extracted linear model is an accurate representative of the enhanced non-linear model of Type-4 WPP, subject to small-signal disturbances.

4.6 Conclusions

This chapter evaluates and validates the enhanced, non-linear, equivalent models of Type-3 and Type-4 WPPs that were developed in Chapter 3. The validation is based on comparing the time-responses of the developed models (Type-3-E and Type-4-E) with those of the built-in models in the PSS/E platform (Type-3-PSSE1 and Type-4-PSSE1). The PSS/E-software built-in models are chosen as the reference since their responses

have been compared with and validated against field measurements. The respective comparisons show that the developed models accurately capture all the dynamics of the PSS/E built-in models. The main contribution of this chapter in continuation of Chapter 3 is providing complete enhanced non-linear generic models of Type-3 and Type-4 WPPs that are implementable in any time-domain simulation software and can replicate the time- responses of the built-in models of the PSS/E software.

This chapter also compares the time-responses of the developed models (Type-3-E and Type-4-E) and the generic models that have been reported in all documented versions of the generic models available in the technical literature (Type-3-H, Type-3-PSSE2, and Type-4-PSSE2). These comparisons show that the documented models of Type-3 and Type-4 WPPs have deficiencies, i.e., either omit or add parts to the generic models which are not defined as integral parts of these generic models and thus they cannot be used to replicate the time-response of the built-in generic models of the PSS/E software (Type-3-PSSE1 and Type-4-PSSE1). For Type-4 WPP model, the deviation of Type-4-PSSE2 response from that of Type-4-E is significantly less than the deviation in the case of the Type-3 WPP model (Type-3-E and Type-3-PSSE2).

The performance of the developed linearized models of Type-3 and Type-4 WPP, presented in Chapter 3, are also validated in this chapter. This is based on comparing their responses against those of the corresponding non-linear models, based on time-domain MATLAB platform, when subjected to small-signal disturbances. These comparisons show that the linearized models of Type-3 and Type-4 WPPs capture the anticipated dynamics and accurately match the time-responses of the non-linear models, when subjected to small-signal disturbances. It also concludes that the non-linear model of Type-3 WPP can be represented by a single linearized model only under certain conditions, otherwise multiple linear models are required to properly/accurately represent the non-linear model. However, the Type-4 WPP can be represented by a single small-signal (linear) dynamic model.

Based on the developed and verified enhanced generic models of Type-3 and Type-4 WPPs, the impacts of high-depth wind power penetration on power systems dynamics can be investigated as discussed in Chapter 5 and Chapter 6.

Chapter 5

Impacts of Wind Power on Power System Low-Frequency Dynamics

5.1 Introduction

The continuous increase in the level of wind power integration in power systems necessitates systematic investigation of the impacts of the high-depth of penetration of wind power on the power system low-frequency dynamics. There are multiple reported studies in the technical literature in this regard. However, the reported conclusions are not definitive and even contradictory. For example, a group of studies conclude that high level of wind power enhances the dampings of the oscillatory modes while another set of studies contradicts this conclusion and show that the wind power, not even at high penetration levels, leads to system instability. Such contradicting conclusions are the results of limitations/drawbacks and the specific scenarios of the conducted studies, i.e.,

- Decreasing the capacity of the conventional power plants or eliminating them from the power system as wind power is integrated in the power system. Such scenarios result in decreasing the total effective inertia of the power system and eliminating the controllers damping effects of the removed power plants.
- Neglecting the impact of load increase which can have a de-stabilizing effect on the system, especially at high-depth of penetration of the wind power.
- Conducting the studies on relatively small power systems that are not suitable/ realistic for high-depth, large-scale integration of wind power.
- Identifying the impacts due to a single type of WPPs and not considering the cases where different types of WPPs exist in the system. This overlooks the impacts due to interactions between different WPP types at different participation percentages.

This chapter investigates the impact of the high-depth of penetration of wind power on low-frequency dynamics, i.e., oscillatory modes (based on the linearized model) and non-linear time-response of System-1. This investigation adopts a practical approach for adding wind power to System-1 based on the proposed study cases presented in Chapter 2, Section 2.6.3 (Table 2.2, Table 2.3 and Table 2.4). The proposed study cases overcome the limitations/drawbacks of the reported studies in the technical literature and lead to generalized conclusions. This is achieved by:

i. Considering different WPPLs, i.e., 5%, 15% and 30%, to cover a wide range of wind power penetration levels and investigate the impacts associated with each penetration level.

ii. Considering system load increase while keeping the output power of the conventional power plants unchanged.

iii. Considering different allocation patterns of the added WPPs.

iv. Considering different participation percentages of Type-3 and Type-4 WPPs.

For the reported studies in this chapter, the enhanced nonlinear equivalent WPP models, developed in Chapter 3, are added to the dynamical model of System-1 and implemented in MATLAB/Simulink software to investigate the impact of high-depth of penetration of wind power on the non-linear time-response of System-1. The extracted linearized WPP models, developed in Chapter 3, are used to identify the impacts of high-depth of penetration of wind power on the low-frequency oscillatory modes of System-1 by analyzing the eigenstructure of the overall linearized system model.

5.2 Wind Power Impacts on Oscillatory Modes

To investigate the impact of wind power on the low-frequency oscillatory modes of System-1, the eigenstructure of the linearized model of the system, corresponding to the study cases of Chapter 2, Table 2.2, Table 2.3 and Table 2.4, are examined. The base case oscillatory modes of System-1 (hereafter referred to as existing modes), presented in Chapter 2 - Section 2.5.2: Table 2.1, are classified as:

i. Control modes: these modes are associated with the magnetic flux and the excitation systems states of the synchronous generators of System-1 (Mode 1 - Mode 11, Table 2.1).

ii. Local plant modes: these modes are associated with the oscillations of one or a group of synchronous generators against the rest of System-1 (Mode 12 - Mode 22, Table 2.1).

iii. Inter-area modes: these modes are associated with the oscillations of a group of synchronous generators in one part of System-1 against other aggregates of synchronous generators in other parts of System-1 (Mode 23 - Mode 26, Table 2.1).

The results of the small-signal dynamical analysis of the system, including WPPs, highlight the

i. impacts of the added WPPs on the existing modes, i.e., those oscillatory modes that are present even without the presence of the WPPs in System-1, and

ii. new oscillatory modes that appear as a result of introducing WPPs in System-1 and otherwise do not exist.

This section presents the impacts of the high-depth of penetration of wind power on the existing modes.

5.2.1 Control Modes

Figure 5.1 and Figure 5.2 show the real and imaginary parts of the eigenvalues corresponding to the control modes for different WPPLs and participation percentages of Type-3 WPPs. These eigenvalues are the closest to the imaginary axis of the s-plan and the eigenvalues corresponding to the other control modes are not included in Figure 5.1 and Figure 5.2, but the changes in their values are consistent with those presented in Figure 5.1 and Figure 5.2. Figure 5.1 and Figure 5.2 illustrate that neither the real nor the imaginary parts of the eigenvalues corresponding to the control modes are practically affected by the WPPL. These modes are neither affected by the WPP type, i.e., Type-3 or Type-4 WPPs, as shown in Figure 5.1 and Figure 5.2. The reason is that these modes are dominantly associated with the magnetic flux states of the synchronous generators and since the operating conditions of each conventional generator is only changed by the change in its respective injected reactive power as the injected active power is kept unchanged; the impacts of the WPPs on these states are insignificant when compared to the base case. Therefore, the impacts of wind power on the control modes are negligible and of no practical importance.

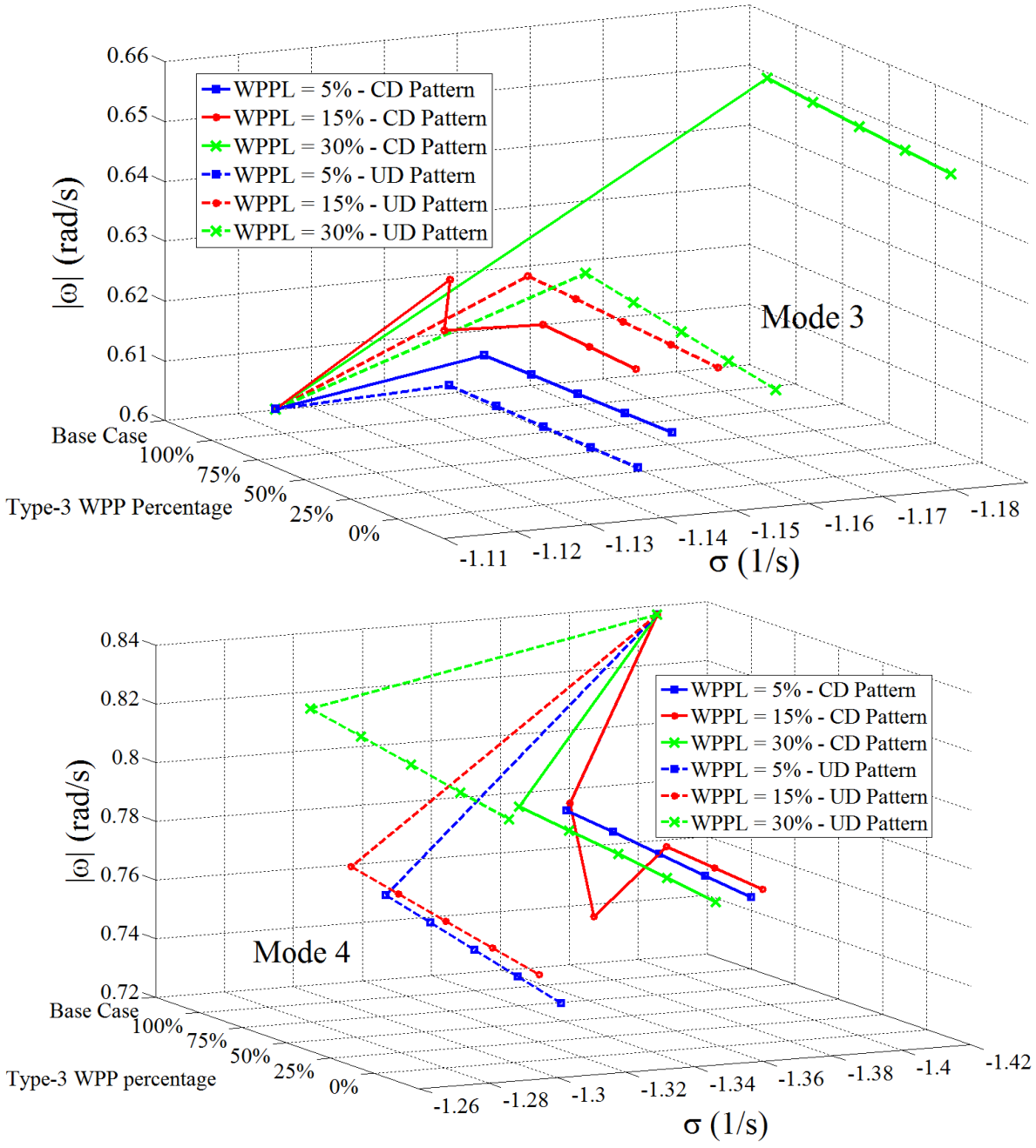

Figure 5.1: The eigenvalues corresponding to control modes 3 and 4 for different WPPLs and participation percentages of Type-3 WPPs

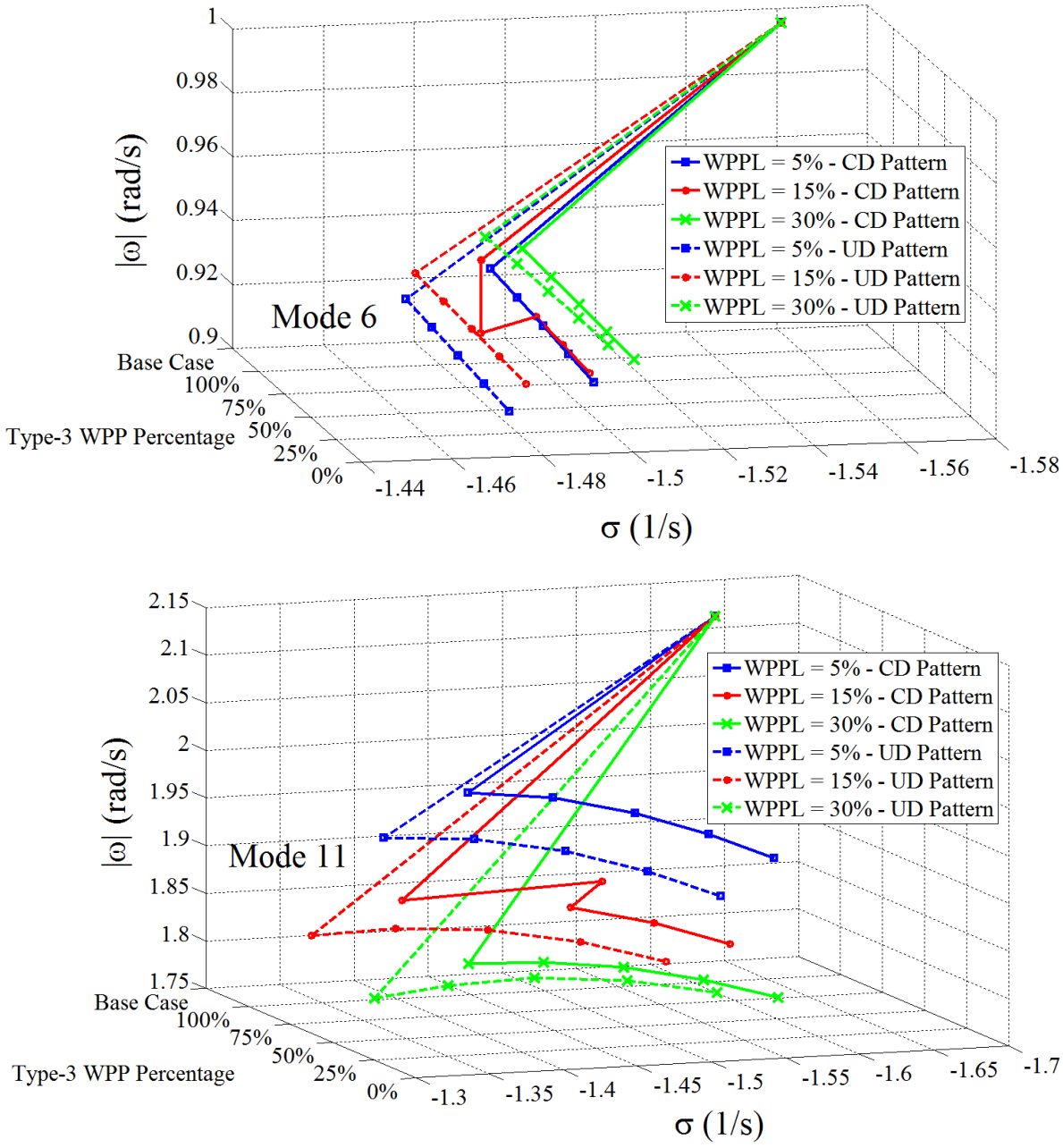

Figure 5.2: The eigenvalues corresponding to control modes 6 and 11 for different WPPLs and participation percentages of Type-3 WPPs

5.2.2 Local Plant Modes

5.2.2.1 Impacts due to WPPL and WPP location

As WPPL increases from 5% to 30%, the damping ratios of the local plant modes decrease by 2% to 60% relative to their values in the base case. Table 5.1 shows the most affected modes and indicates that as the WPPL increases, the damping ratio of a larger number of local modes are decreasing below 5%. This results in low-frequency oscillations with larger amplitudes and longer durations when the system is subjected to a disturbance. The reason for a such decrease is interactions among the reactive power controllers of the WPPs and the excitation systems of the affected generators. The addition of WPPs to System-1 and the load increase results in increasing the reactive power injected by the synchronous generators. In addition, the reactive power controllers of the WPPs restore the bus voltages near the affected generators to their pre-fault values in a shorter time compared to the base case. However, due to the slow response of the DC exciters located at the affected synchronous generators, the amplitude and duration of the oscillations of the affected generators increase which appears as a decrease in the damping ratio of the local plant mode of the affected synchronous generators.

The locations of WPPs determine the local plant modes whose damping ratios are decreased. For example, mode 21 is a local plant mode corresponding to GEN-12. The damping ratio of this mode is mostly affected by the WPP integration of the New-York Group. The presence of WPPs in the New York system can drive this mode to instability and the effect is more pronounced with the increase in the WPPL. This can be observed by comparing the decrease in the damping ratio of mode 21 corresponding to WPPL of 15% and 30%. Mode 21 is not significantly affected for WPPL of 5%. The reason is that the addition of the WPPs for the study cases corresponding to 5% WPPL (Table 2.2) is limited to the New England system at the Southern Group.

5.2.2.2 Impacts due to WPP type

Figure 5.3 shows the change of the damping ratios of the most affected local plant modes of Table 5.1 due to the change in the participation percentage of Type-3 WPP. Figure 5.3 shows that 100% Type-3 WPP, based on UD pattern, has the most impact on the damping ratios of the affect local plant modes while 100% Type-4 WPP, based on UD pattern, has the least impact. The local plant modes are affected by interactions between the controllers of the WPPs and the excitation systems of the generators corresponding to such modes. Even though both WPP types adopt nearly the same reactive power controller structure, as discussed in Chapter 3, they do not have the same parameter

Table 5.1: Most affected local plant modes for different WPPLs

WPPL	Affected Mode(s)	Lowest Damping		Highest Damping		Damping reduction range
		Value	Case	Value	Case	
5%	22	4.76%	100% Type-3 UD	5.79%	100% Type-4 CD	11.06% - 26.89%
15%	21	3.83%	100% Type-3 UD	4.78%	100% Type-4 CD	25.31% - 40.16%
	22	4.61%	100% Type-3 UD	5.74%	100% Type-4 CD	11.83% - 29.19%
30%	12	4.45%	100% Type-3 CD	5.24%	100% Type-4 CD	24.17% - 35.60%
	17	2.06%	100% Type-3 CD	3.38%	100% Type-4 CD	6.37% - 42.94%
	21	2.67%	100% Type-3 UD	4.76%	100% Type-4 CD	25.63% - 58.28%
	22	3.94%	100% Type-3 UD	5.63%	100% Type-4 CD	13.52% - 39.48%

values (as given in Appendix B). This results in Type-3 WPPs having the highest impact on the damping ratios of local plant modes. Figure 5.3 also shows that changes in the damping ratios of the affected local plant modes are nearly linear.

5.2.3 Inter-area Modes

The investigations show that the inter-area modes are mainly affected by the WPP locations. The salient study result is that when a system is characterized by an inter-area mode and one area is exporting power to another, then if introducing a WPP results in increasing the power exchange between the areas, the damping ratio of the inter-area mode is reduced. However, if the location(s) of the introduced WPP(s) are such that the power exchange between the two areas remains unchanged, then the damping ratio of the inter-area mode is not affected. It should be noted that the integration of WPP does not introduce new inter-area modes in the host system. The reason is that Type-3 and Type-4 WPPs do not change the inertia distribution of the system and their time-response is not in the frequency range of the inter-area modes. This conclusion is based on observing the change in the damping ratio of mode 24 of Table 2.1 associated with the different study cases presented in Chapter 2 (Table 2.2, Table 2.3 and Table 2.4). Mode 24 represents oscillations of GEN-2 - GEN-7, located at the south of the New England System (Figure 2.6), against the generators of the New York system and primarily affected by WPP at a low WPPL, i.e., at 5% level (Table 2.2). The damping ratio of this mode decreases

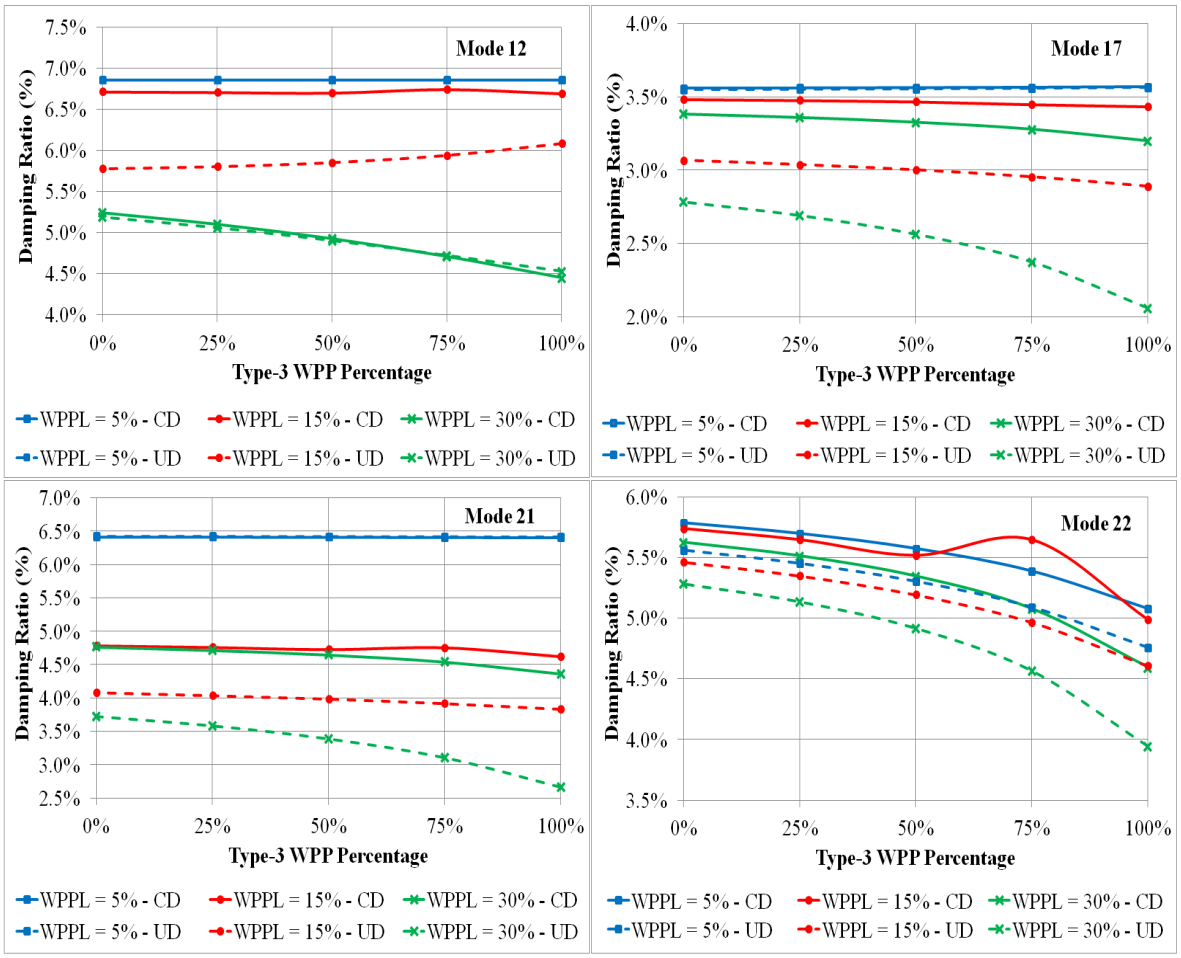

Figure 5.3: Impact of WPP type on the damping ratios of local plant modes

from 4.29%, in the base case, to 2.48% corresponding to 5% WPPL as shown in Table 5.2. This represents a 42% decrease in the damping ratio and thus is of concern at this low WPPL. Table 5.2 shows the damping ratio of mode 24 for the proposed study cases in Chapter 2. Table 5.2 shows that the change in the damping ratio of mode 24 in some of the proposed study cases is not as significant as that in the case of 5% WPPL, 100% Type-3 under UD pattern. However, for some study cases, e.g., the case corresponding to 15% WPPL and 100% Type-4 WPP, the damping ratio of mode 24 increases. The reason is that for the study cases corresponding to 15% and 30% WPPLs, WPPs are added in the New-York Group which results in decreasing the power exchange between the New York system and GEN-2 - GEN-7, and consequently an increase in the damping ratio of mode 24.

To further investigate the conditions associated with the above results, i.e., relating the addition of wind power to a power system and the change in the damping ratios of its

Table 5.2: Damping ratio of mode 24 for study cases proposed in Chapter 2

Type-3 / Type-4 Ratio	5% WPPL		15% WPPL		30% WPPL	
	CD	UD	CD	UD	CD	UD
100% / 0%	3.03%	2.48%	3.61%	3.28%	4.08%	3.15%
75% / 25%	3.46%	3.08%	3.89%	3.67%	4.21%	3.47%
50% / 50%	3.74%	3.47%	4.12%	3.97%	4.32%	3.74%
25% / 75%	3.90%	3.71%	4.26%	4.17%	4.40%	3.92%
0% / 100%	4.03%	3.87%	4.36%	4.30%	4.45%	4.04%

inter-area oscillatory modes, the locations of added WPPs corresponding to three study cases from the proposed cases in Chapter 2, are changed as follows.

- ***Case-1M***

This scenario corresponds to (i) 15% WPPL, (ii) 100% Type-3 WPP, and (iii) all WPPs added to the Southern WPP Group (at Bus-59 and Bus-65). In this study case, the power exchange between the southern area of the New England system (GEN-2 - GEN-7) and the New York system increases. This decreases the damping ratio of mode 24 to 1.49% which is a very low value when compared to the base case value of 4.29%.

- ***Case-2M***

This scenario corresponds to (i) 5% WPPL, (ii) 100% Type-3 WPP, and (iii) all the WPPs added to the Northern WPP Group (at Bus-26 and Bus-29). This study case investigates the impact of WPPs on the damping ratio of mode 26. Mode 26 represents oscillations of GEN-8, GEN-9 and GEN-13, located at the north of the New England System (Figure 2.6), against the generators of the New York system. In this scenario, the power exchange between the northern area of the New England system (GEN-8, GEN-9 and GEN-13) and the New York system increases and thus decreases the damping ratio of mode 26 from 7.71% (base case) to 4.57%, i.e., 40.73% reduction.

- ***Case-3M***

This scenario corresponds to (i) 15% WPPL, (ii) 100% Type-3, and (iii) all WPPs added to the New-York Group (at Bus-33 and Bus-45). In this study case, the power exchanges between the New York system and both areas of the New England system, i.e., north area (GEN-8, GEN-9 and GEN-13) and south area (GEN-2 GEN-7), decrease. The reason is that all the WPPs are added in the New York system which is importing power from the other two areas. This decrease in the power exchange increases the damping ratios of mode 24 and mode 26 to 5.39% and 7.85% respectively, compared to 4.29% and

Table 5.3: Damping ratios of mode 24 and mode 26 for the modified study cases

	Base Case	Case-1M	Case-2M	Case-3M
Mode 24	4.29%	1.49%	3.12%	5.39%
Mode 26	7.71%	6.69%	4.57%	7.85%

7.71% respectively in the base case. Table 5.3 provides a summary of the damping ratios of mode 24 and mode 26 for the above study cases.

The significance of this conclusion is that it provides a unified explanation for the different and contradicting conclusions reported in the technical literature regarding the impacts of wind power on the inter-area oscillatory modes, i.e.,

i. Addition of WPPs does not introduce new inter-area oscillatory modes. However, it can impact the existing ones.

ii. The impact of adding WPPs is limited to changes in the damping ratios of inter-area modes while their corresponding frequencies are not noticeably affected.

iii. The impact of WPPs on the damping ratio of an inter-area mode depends on the location(s) of the added WPP(s) with respect to the power exchange between the areas exhibiting such an inter-area oscillations. This indicates if the added WPPs increase the power exchange between two areas, the damping of the inter-area mode corresponding to these two areas decreases.

5.3 New Oscillatory Modes

Addition of WPPs introduces new oscillatory modes that do not exist in the base case; however, the new modes are not inter-area modes. The new modes can be categorized as:

i. Modes introduced by integration of Type-3 WPPs only and hereafter are referred to as Type-3 Modes.

ii. Modes introduced by addition of either Type-3 or Type-4 WPPs and hereafter are referred to as Common Modes.

iii. Modes introduced by addition of both Type-3 and Type-4 WPPs and hereafter are referred to as Mutual Modes.

5.3.1 Type-3 Modes

This mode is associated with the equivalent Wind Turbine Generator (WTG) of Type-3 WPP. The number of Type-3 modes is equal to the number of added Type-3 WPPs. These modes are of low-frequency (e.g., 0.0264 Hz) and highly damped (e.g., $\zeta = 71\%$). They are affected neither by the location of the WPPs nor the WPPL. The reason is that the low-frequency oscillations originating from the host grid do not affect the mechanical system of Type-3 WPP due to the fast response of the rotor-connected converter and its controllers. Thus, the dynamics of the equivalent wind turbine is practically decoupled from the dynamics of the host grid.

5.3.2 Common Modes

The common mode is associated with the WPP converter and the corresponding controllers. Each common mode is highly damped with the damping ratio within the range of 50% to 100%. However, the frequency of each common mode varies in a fairly wide range (0.4 - 9 Hz). The common mode is not affected by the WPPL and exists regardless of the WPP type. The reason is that both WPP types adopt nearly the same controller structure for active or reactive power components.

5.3.3 Mutual Modes

Mutual modes result from interactions between the controllers of Type-3 and Type-4 WPPs, i.e. they exist only when both WPP types are present in the system. The reason for the presence of the mutual modes is that the parameters of the controllers are not the same for both WPP types even when both types adopt the same controller structure. The frequency range of these modes is fairly narrow, i.e., 0.45Hz to 0.55Hz, and their damping ratios are relatively high, i.e., 26% - 50%. The mutual modes are not affected by the WPPL since they result from interactions of controllers. The damping ratios of mutual modes increase with the increase in the level of wind power associated with Type-4 WPPs. The reason is that the response of the reactive power controller of Type-4 WPP is faster than that of Type-3 WPP as discussed in Chapter 4. Therefore, the oscillations in the time-response are damped faster as the percentage of Type-4 WPPs increases. The number of the mutual modes is equal to the number of the added WPPs since in the proposed study cases both WPP types are added simultaneously to all the selected locations (Table 2.2, Table 2.3 and Table 2.4).

5.4 Wind Power Impacts on Nonlinear Time-Response

This section investigates the impact of wind power on the nonlinear transient response of System-1. For the investigation presented in this section:

i. System-1 is subjected to a five-cycle, three-phase-to-ground, self-cleared fault.

ii. The nonlinear enhanced equivalent WPP models, developed in Chapter 3, are used. The wind power is added to System-1 based on the study cases presented in Chapter 2 (Table 2.2, Table 2.3 and Table 2.4) and the nonlinear model of the overall system, i.e., System-1 including WPPs, is implemented in the MATLAB/Simulink software.

iii. Different power system load models, i.e., constant impedance, constant power and constant current representations were considered. All the three representations result in similar time-responses and thus the same conclusions, based on either representation, can be made. To avoid unnecessary reputations, the results based on representing System-1 loads via constant impedances are presented.

iv. Faults at all buses of System-1 for all the study cases presented in Chapter 2 were considered. Most of the fault scenarios result in dynamic time-responses that are consistent with the linearized system (small-signal) analyses presented in the previous section. Two fault locations (at Bus-26 and Bus-29) result in distinct dynamical time-responses. The fault at Bus-29 results in an unstable time-response for nearly all the study cases proposed in Chapter 2. The reason is that Bus-29 is the high voltage terminal bus of GEN-9 (Figure 2.6) and the System-1 instability results from the instability of GEN-9 for all study cases. Therefore, the time-responses of System-1 due to the fault at Bus-26 are presented in this section.

5.4.1 Base Case Nonlinear Time-Response

The fault at Bus-26 results in oscillatory instability of System-1 where the speed oscillatory amplitudes of the synchronous generators increase with time as shown in Figure 5.4. Figure 5.4 shows the speed deviation of GEN-9 for the fault at Bus-26. This oscillatory instability is due to the static exciter and PSS of GEN-9 which is the most affected generator by the fault at Bus-26.

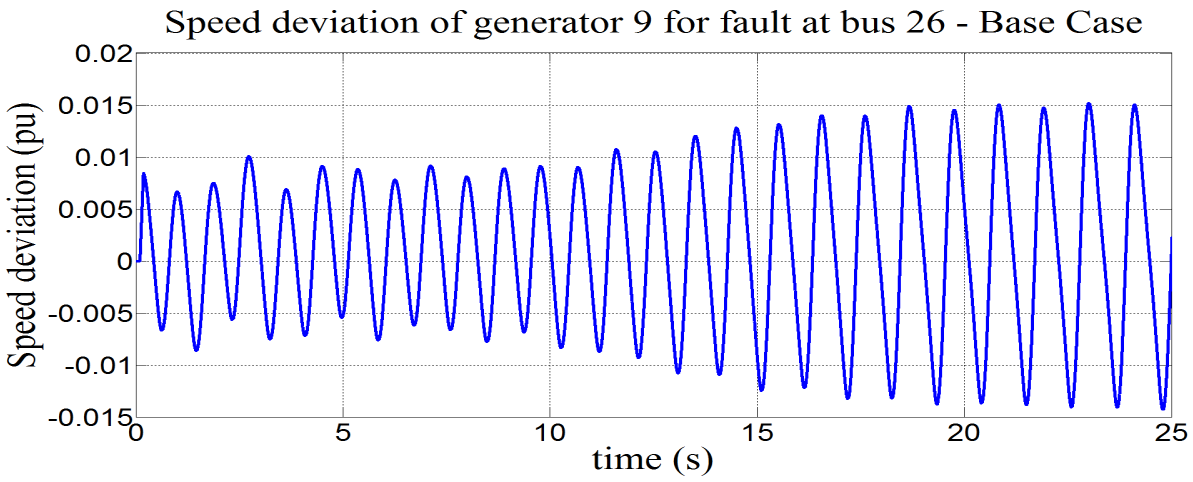

Figure 5.4: GEN-9 speed deviation for fault at Bus-26 for the base case

5.4.2 Nonlinear Time-Response Corresponding to Wind Power Levels

The same fault of Figure 5.4 is applied to Bus-26. Figure 5.5(a) and (b) show the speed deviation of GEN-9 corresponding to 100% Type-4 WPP at 5% WPPL and 15% WPPL respectively. For 5% WPPL, Figure 5.5(a), System-1 is stable where the oscillations in the synchronous generators speeds are fully damped after 10 seconds. This represents a significant improvement in System-1 time-response as compared to that of the base case, Figure 5.4.

Figure 5.5(b) also shows that System-1 is stable. However, the pattern of speed oscillations of GEN-9 is different than that of Figure 5.5(a). In Figure 5.5(b), the envelope for the GEN-9 speed oscillations exhibits two crests where the first crest is higher than the second one. The second crest exhibits its highest value when the participation percentages of Type-3 and Type-4 WPPs are equal, i.e., for the study cases corresponding to 50% Type-3 WPPs in Table 2.3. The time-response of Figure 5.5(b) is due to the interactions between the controllers of Type-3 and Type-4 WPPs and is only observed when both WPP types exist in the system.

For the study cases corresponding to 30% WPPL, Table 2.4, the System-1 behavior becomes highly non-linear and the impact of wind power on System-1 transient stability, i.e., whether System-1 is stable or not when subjected to the fault at Bus-26, cannot be predicted without using the time-domain simulation of the system nonlinear model. For the study cases of Table 2.4, the same fault of Figure 5.4 results in System-1 instability for cases corresponding to 75% and 100% Type-4 WPPs under UD pattern, and stable

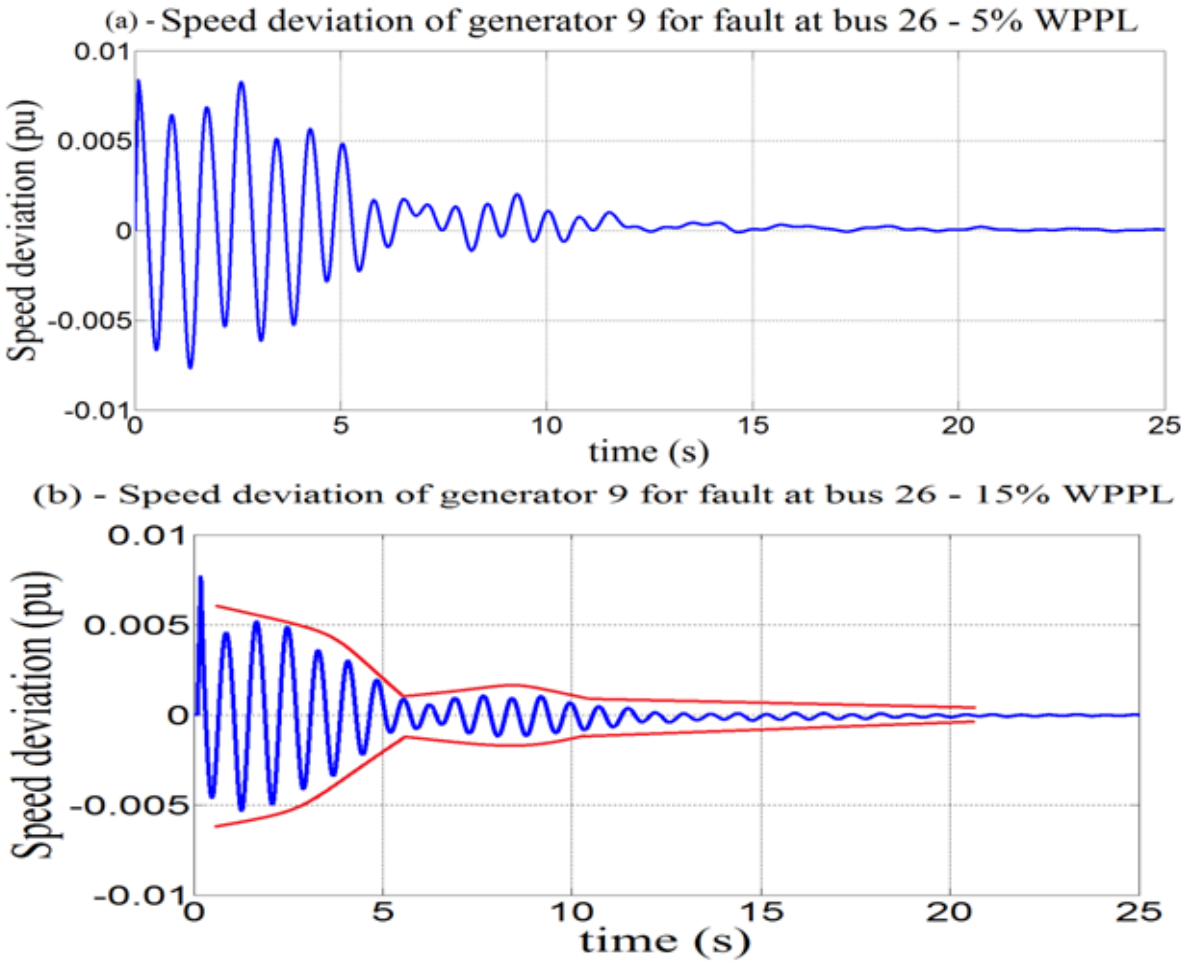

Figure 5.5: GEN-9 speed deviation for fault at Bus-26 corresponding to 100% Type-4 WPP (a) 5% WPPL and (b) 15% WPPL

Table 5.4: Transient stability assessment for fault at Bus-26 with 30% WPPL

WPPs Pattern	Type-3 WPPs Percentage				
	100%	75%	50%	25%	0%
CD	Stable	Stable	Stable	Stable	Stable
UD	Stable	Stable	Stable	Unstable	Unstable

time-response for the remaining study cases as shown in Table 5.4. Figure 5.6(a) and (b) show the speed deviation of GEN-9 corresponding to 75% Type-4 WPP under CD and UD patterns respectively. Figure 5.6(a) shows that the pattern of speed oscillations is different than the one corresponding to the 15% WPPL, Figure 5.5(b), where the speed oscillations do not exhibit an envelope and they are fully damped after 20 seconds. This duration is longer than that of the 5% WPPL, Figure 5.5(a). Regarding Figure 5.6(b), the amplitudes of speed oscillations increase and the system becomes unstable.

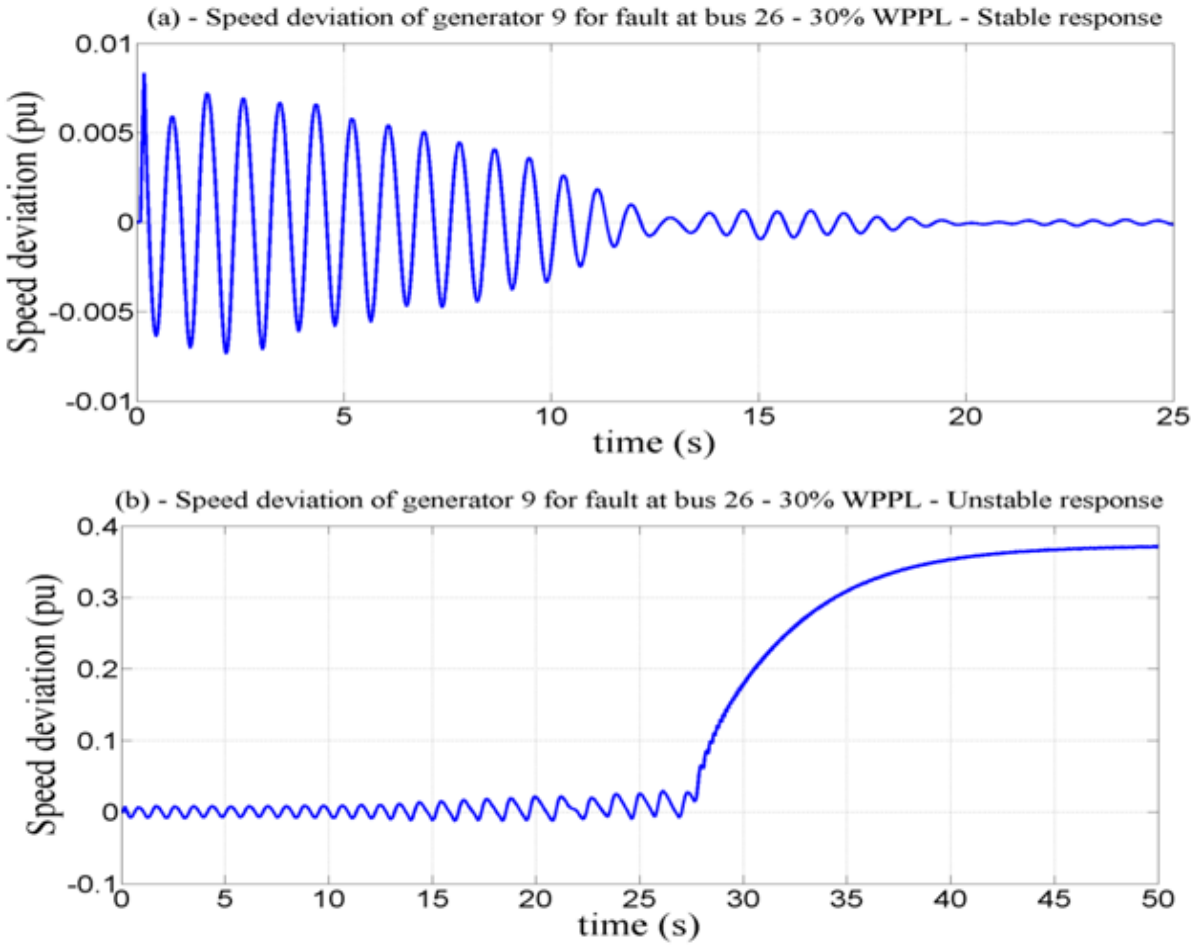

Figure 5.6: GEN-9 speed deviation for fault at Bus-26 corresponding to 75% Type-4 WPP (a) CD pattern (Stable) and (b) UD pattern (Unstable) WPPL

The above results show that as the WPPL increases, System-1 exhibits higher degree of nonlinearity and the impact of wind power on System-1 transient stability can be determined only from the time-domain simulation of the system nonlinear model. This indicates that the results of the transient stability assessment of System-1 for the 5% and 15% WPPLs cannot be extrapolated to the 30% WPPL. In addition, the impact of wind power on the transient time-response, i.e., when System-1 is stable when subjected to a fault, is significantly different for 5%, 15% and 30% WPPLs, i.e., Figure 5.5(a) and (b) and Figure 5.6(a) respectively. Finally, the results reinforce the necessity of developing nonlinear models that can capture all the dynamics of the WPPs in the frequency range of transient stability assessment.

5.5 Conclusions

This chapter presents the impacts of wind power on the low-frequency dynamics of System-1. The adopted approach in adding wind power to System-1 and thus, the proposed study cases largely overcome the limitations/drawbacks of the reported studies in the technical literature. For identifying the impacts of wind power on the low-frequency oscillatory modes, linearized WPP models developed in Chapter 3 are used for eigenstructure analysis of the overall linearized system model (System-1 including WPPs). The salient conclusion of this work is identifying the impact of wind power on the inter-area oscillatory modes. This conclusion (i) presents a consistent basis for identifying the impacts of high-depth of wind power penetration on inter-area oscillations and (ii) provides a unified explanation of the contradicting results reported in the technical literature, i.e.,

i. Addition of WPPs does not introduce new inter-area oscillatory modes. However, it may impact the existing ones. The reason is that WPPs do not change the inertia distribution of the system.

ii. The impact of adding WPPs is limited to changing the damping ratios of inter-area modes while their corresponding oscillation frequencies are insignificantly affected.

iii. The impact of WPPs on the damping ratio of an inter-area mode is determined based of the location(s) of the added WPP(s) with respect to the power exchange between the areas exhibiting such an inter-area oscillations. This indicates if the added WPPs increase the power exchange between two areas then the damping of the inter-area mode corresponding to these two areas will decrease.

This chapter also discusses the impacts of wind power on the local plant modes. It shows that the impact on the local plant modes is related to interactions among the reactive power controllers of the WPPs and the excitation systems of the affected generators. The addition of WPPs to System-1 and the load increase results in increasing the reactive power injected by the synchronous generators. In addition, the reactive power controllers of the WPPs restore the bus voltages near the affected generators to their pre-fault values in a shorter time compared to the base case. However, due to the slow response of the DC exciters located at the affected synchronous generators, the amplitude and duration of the oscillations of the affected generators increase which appears as a decrease in the damping ratio of the local plant mode of the affected synchronous generators.

Moreover, this chapter categorizes the new oscillatory modes introduced by the addition of WPPs to System-1 into (i) Type-3 Modes, (ii) Common Modes, and (iii) Mutual

Modes. Type-3 modes are associated with the equivalent WTG of Type-3 WPPs and are affected neither by the WPPL nor the WPP location. This is due to the fast responses of the rotor-connected converter and its controllers. Common modes (i) are associated with the WPP converter and the corresponding controllers, (ii) exist regardless the WPP type and (iii) are not affected by the WPPL. The reason is that both WPP types adopt nearly the same controller structures. Mutual modes exist when both WPP types are present in the system and result from interactions between the controllers of Type-3 and Type-4 WPPs. The reason for the presence of the mutual modes is that the parameters of the controllers are not the same for both WPP types. The mutual modes are not affected by the WPPL and their damping ratios increase with the increase in the level of wind power associated with Type-4 WPPs. This is due to the faster response of the reactive power controller of Type-4 WPP compared to that of Type-3 WPP.

This chapter also presents the impacts of wind power on the nonlinear transient response of System-1. For these analyses, the enhanced nonlinear equivalent WPP models developed in Chapter 3 are used to simulate System-1 including WPPs in MATLAB/Simulink software. This chapter shows that as the depth of penetration of wind power increases, System-1 exhibits higher degree of nonlinearity and the impact of wind power on System-1 transient stability can be determined only from the time-domain simulation of the system nonlinear model. This indicates that the results of the transient stability assessment of System-1 for lower WPPLs cannot be extrapolated to higher WPPLs. In addition, the impact of wind power on the transient time-response, i.e., when System-1 is stable when subjected to a fault, is significantly different for the 5%, 15% and 30% WPPLs. This necessitates the assessment of the system transient response using the time-domain simulation of the system nonlinear model. Finally, the results reinforce the necessity of developing nonlinear models that can capture all the dynamics of the WPPs in the frequency range of transient stability assessment.

Chapter 6

Impacts of Wind Power on Power System Coherency[3]

6.1 Introduction

Identifying the impacts of high-depth penetration of wind power on power system coherency requires an appropriate coherency identification method which should (i) be capable of considering the effect of added WPPs on the coherency phenomenon and (ii) account for the hybrid nature of the equivalent WPP models as discussed in Chapter 3 and Chapter 4. However, the existing coherency identification methods (either model-based or measurements-based) exhibit limitations/drawbacks when WPPs are considered. These limitations/drawbacks are:

- Model-based methods suffer from the inherent inability to account for the hybrid nature of the WPPs generic models since they neglect (i) changes in the system operating conditions, (ii) changes in the system configuration, and (iii) discrete operational modes of specific subsystems, e.g., HVDC links and WPPs. Moreover, they assume that coherency is independent of (i) disturbance severity and (ii) details of the generator model [39]. Therefore, they neglect the electrical dynamics of the generators and consider linearized swing equation of synchronous generators to determine the coherent groups. Such an approach cannot be extended to include WPPs to identify the coherent groups.

- Measurement-based methods use the turbine speed deviation signals of the syn-

[3]The work presented in the first part of this chapter is published as A.M. Khalil and R. Iravani, "A Dynamic Coherency Identification Method Based on Frequency Deviation Signals," *IEEE Trans. on Power Systems*, doi: 10.1109/TPWRS.2015.2452212

chronous generators for coherency identification. Such signals, in case of WPPs, are not representative of the dynamical responses of the WPPs with respect to the host grid side, due to the fast action of the converters and their controllers. This limits the applicability of such methods to the coherency analysis of the classical power system where all power plants are based on synchronous generators.

To overcome the above, this chapter introduces and develops a new dynamic coherency identification method. This method is measurement-based and uses bus frequency deviations with respect to the system nominal frequency to identify coherent groups. The salient feature of the developed method is that it utilizes frequency-deviation signal which (i) is a natural representative of the variations in the synchronous generators rotor angles and (ii) is equally identifiable for the WPPs and non-generator buses. Therefore, the impact of the integrated WPPs on the system coherency can be investigated. Moreover, the method has the advantages of (i) dynamic tracking of the time-evolution of coherency, (ii) being immune to measurement noise, and (iii) requiring lower computational burden as compared to other measurement-based coherency identification methods. Measured bus frequency-deviation signals from the the MATLAB/Simulink-based dynamic nonlinear model of System-1, Chapter 2, Section 2.3, are used to identify the coherency characteristics of the study system. The latter part of this chapter applies the developed method to quantify the impact of high-depth penetration of wind power on the System-1 coherency structure, based on the equivalent nonlinear models developed in Chapter 3 for the study cases presented in Chapter 2, Section 2.6.3.

6.2 Dynamic Coherency Determination (DCD) Method

The developed method [38] is based on determining frequency deviations of the power system generator buses, e.g., based on the use of a Wide Area Monitoring System (WAMS), and is referred to as the Dynamic Coherency Determination (DCD) method. In addition, the developed DCD method is extended to non-generator buses and identifies each electrical area based on both coherent generators and the associated non-generator buses. The DCD method is composed of two steps.

- Identification of coherent generator groups.
- Association of non-generator buses with the appropriate coherent generator groups to form electrical areas.

The required signal for the DCD method is the frequency deviation, with respect to the system nominal frequency, within a pre-specified time period (6.3). This signal is obtained at each bus i of the system at pre-specified time instants and form the frequency deviation vector Δf_i

$$\Delta f_i = [\ldots\ldots \Delta f_i|_{t-\Delta t}\ \Delta f_i|_t\ \Delta f_i|_{t+\Delta t} \ldots\ldots]^T. \tag{6.1}$$

The reasons for selecting the frequency deviation signal are:

i. Frequency deviation is a natural representative of the status of variations in the generator rotor angle upon which the concept of coherency is defined.

ii. Frequency deviation vectors can be used to determine the Center Of Inertia Frequency Deviation (COIFD) vector of a group of coherent generators. The COIFD vector is defined as the average frequency deviation vector of the generators of a coherent group

$$COIFD = \frac{\sum_{j=1}^{n_g} \Delta f_j}{n_g}, \tag{6.2}$$

where n_g is the number of generators in the coherent group. COIFD is a representative of the coherent group for identifying the corresponding electrical area.

iii. Frequency deviation is equally calculable at non-generator buses and WPPs. This provides a means to (i) include the WPPs in the determination of the coherent groups of generators and (ii) associate non-generator buses to coherent generator groups and construct electrical areas.

Subsequent to a disturbance in the power system, the frequency deviation of bus i at time t+Δt can be determined from the rate of change of the phase angle of the bus voltage

$$\Delta f_i|_{t+\Delta t} = \frac{1}{\omega_o}\left(\frac{\emptyset_i|_{t+\Delta t} - \emptyset_i|_t}{\Delta t}\right), \tag{6.3}$$

where ω_o is the system nominal frequency, ϕ_i is the voltage phase angle of bus i, and t and t+Δt are time instants. Therefore, for a time interval (T) subsequent to a disturbance, n frequency deviation measurements are specified where

$$n = \frac{T}{\Delta t}. \tag{6.4}$$

The vector-space ΔF is formed by the frequency deviation vectors, where,

$$\Delta f_i \in \Delta F,\ i = 1, \ldots, N, \tag{6.5}$$

$$\Delta F \subset \Re^n, \tag{6.6}$$

where N is the number of buses. Equation (6.5) assumes that voltage measurements of all buses are available or can be calculated from the measurements of the observable buses, i.e., the system is fully observable.

6.2.1 Identification of Coherent Generators

The frequency deviation vectors of the generator buses form the vector–space ΔF_g where

$$\Delta F_g \subset \Delta F. \tag{6.7}$$

Two generators *"i"* and *"j"* are considered coherent after a disturbance if the difference in the corresponding rotor angles, and therefore the terminal bus frequency deviations, remain relatively small throughout the time interval of interest. This difference between the frequency deviation vectors can be expressed by the Coherency Coefficient (CC_{ij}) which is defined as the cosine of the angle between Δf_i and Δf_j

$$CC_{ij} = \frac{\Delta f_i{}^T \Delta f_j}{\|\Delta f_i\| \times \|\Delta f_j\|}\ . \tag{6.8}$$

CC_{ij} ranges from -1 to 1 where $CC_{ij} = 1$ indicates identical frequency deviation vectors and thus "perfect coherency". This is practically the case when generators *"i"* and *"j"* are connected to the same bus. In the developed method, the degree of coherency is determined based on the difference between the coherency coefficient and a pre-specified value γ. γ is the limit which separates coherent and non-coherent generators. Based on the value of γ, we define:

Definition: *Two frequency deviation vectors, Δf_i and Δf_j, are "related" in terms of coherency if they are located in the same space formed by a right angle cone (from hereafter "cone") whose axis is along one of the two frequency deviation vectors and the cosine of its vertex angle is equal to γ, otherwise they are unrelated.*

Figure 6.1 shows that frequency deviation vectors Δf_j and Δf_k are within the cone

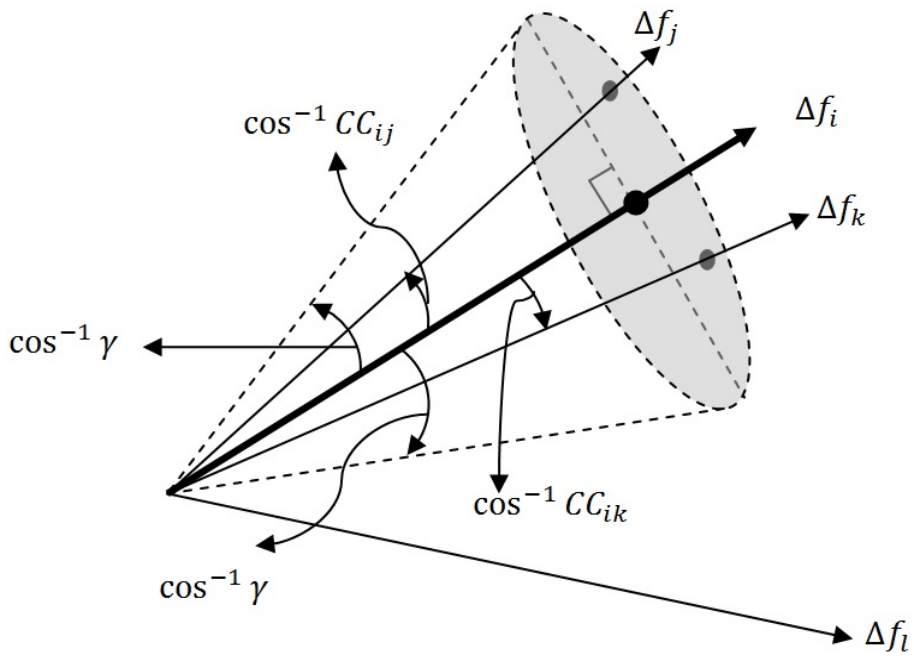

Figure 6.1: Definition of related/unrelated frequency deviation vectors in terms of coherency

whose axis is along Δf_i and the cosine of its vertex angle is γ. Therefore, Δf_j and Δf_k are related to Δf_i in terms of coherency; however, Δf_l does not belong to the same space and is "unrelated" to Δf_i. It should be noted that Δf_j and Δf_k are not necessarily related to each other. Figure 6.1 also indicates that CC of any two related vectors, e.g., Δf_i and Δf_k, is either smaller than or equal to γ.

Thus to decompose the vector-space ΔF_g into a set of coherent groups, sets of "related" frequency deviation vectors, where each set is expressed by its unique COIFD, need to be determined, as follows.

STEP-I: The objective of this step is to divide generator buses into groups where in each group all frequency deviation vectors are tightly related, i.e., γ is close to 1, e.g., 0.99.

- Select a value for γ, e.g., $\gamma = \gamma_c = 0.99$.
- Select a generator bus, e.g., bus *"i"* and assign it to group *"p"*. Assign to group *"p"* all the generator buses *"js"* such that

$$CC_{ij} \geq \gamma = \gamma_c \quad , \forall\, i \,\&\, j \in p. \tag{6.9}$$

Thus all the generators of group *"p"* are tightly and bilaterally related. This also

ensures the uniqueness of the group, irrespective of the bus selected to start the process.

- Continue the above step for the remaining buses until all the buses are divided in K groups with m_p buses in each group. Both K and m_p are integers that can assume values of unity or larger.

- Calculate COIFD vector of each group p, $p = 1,,K$,

$$COIFD_p = \frac{\sum_{j=1}^{m_p} \Delta f_j}{m_p}, \tag{6.10}$$

where m_p is the number of generators in group p, and COIFD_P is the reference vector for group p.

STEP-II: The objective of this step is to combine the tightly related generator groups of STEP-I into coherent groups, based on a more relaxed value of γ as compared to γ_c of (6.9). The reason for relaxing γ is to come up with a viable and practically meaningful number of coherent groups. If γ is too close to unity, then each generator constitutes a group. If γ is much smaller than unity, then all generators will form one group. These are the two extreme limits of any coherency identification method.

- Select a relaxed (as compared to γ_c) value for γ, e.g.,

$$0.9 \ \leq \ \gamma = \ \gamma_r \ < 0.99 \, . \tag{6.11}$$

- Calculate the CC_{pq} for each pair *"p"* and *"q"* groups of STEP-I.

- Merge the two "related" groups *"p"* and *"q"* with the highest CC_{pq} into a new coherent group *"b"*

$$COIFD_b = \frac{m_p \times COIFD_p + m_q \times COIFD_q}{m_p + m_q}. \tag{6.12}$$

- Repeat the above two sub-steps until all the CC_s are less than γ_r.

Step-II divides all the generator buses into coherent groups with a COIFD vector representing each group. The COIFD vectors are used in the next phase of the DCD method.

6.2.2 Association of Non-generator Buses

Subsequent to identification of the coherent generator groups from the previous subsection, the non-generator buses are associated to each group, as follows.

- Determine Δf_a of each non-generator bus *"a"*.
- Calculate CC_{ae} for each non-generator bus *"a"* and every coherent group e where group *"e"* is represented by its vector COIFD_e (6.12).
- Associate non-generator bus *"a"* to the coherent group which provides the highest value of CC_{ae}.

It should be noted that:

- Similar to all measurement-based methods, the DCD method requires full observability. All generator buses are observable; however, the non-generator buses must be either observable or equipped with PMUs.
- Categorization/admission process of the non-generator buses to coherent groups is not dependent on the selected value of γ which is used only for coherency identification of generators. The reason is that the non-generator buses are admitted to groups which they exhibit the highest CC with.

6.3 DCD Method Study Results for the Base Case Conditions

This section applies the DCD method to System-1 prior to the addition of any WPPs, i.e., the base case. The objective of the analysis is to demonstrate the capabilities of the DCD method in the dynamic evolution of the system coherency in its base case. The reported studies are based on time-domain simulation of System-1 in the MATLAB/Simulink platform, using the model of Chapter 2. The simulation time-step is 1.667 ms and each simulation case provides 20 seconds of dynamic response of the system subsequent to a disturbance [68]. The simulated response is sampled at the rate of 120 Hz as encouraged by the IEEE standard for synchrophasor measurements [69]. The sampling mechanism adopted is a simple selection of samples from the simulated signal corresponding to 120 Hz. Finally, samples corresponding to very high values of frequency deviation instantaneously following the fault application and clearing were neglected. The reason is that these high values are the result of representing the AC network by algebraic equations

Table 6.1: Coherent groups and the associated buses (Case I)

Area	Coherent Generators	Associated Non-Generator Buses
1	2,3,4,5,6,7	19,20,21,22,23,24,37,52,56,57,58,59,60, 62,63,64,65,66,67,68
2	8,13	25,26,27,55
3	9	28,29
4	1,12	17,34,35,36,39,43,44,45
5	10,11	30,31,32,33,38,40,46,47,48,49,51,53,54, 61
6	15,16	18,42,50
7	14	41

and do not represent actual changes in the system. A large number of case studies were conducted, however, only three case studies which exhibit distinct characteristics, are reported in this section. The coherency is identified based on $\gamma_r = 0.95$ (6.11).

6.3.1 Case I - Fault at Bus-27

Initially the system is under a steady-state condition and at t=0 s is subjected to a 5-cycle, self-cleared three-phase-to-ground fault at Bus-27. This disturbance results in creation of 7 areas as given in Table 6.1. In this case, the system is divided into two large areas (Area 1 and Area 5) and the remaining areas are comparable in terms of their sizes. Figure 6.3 shows the electrical boundaries of the areas. Figure 6.2 shows the frequency deviation signals of the generator buses used to construct the vector subspace ΔF_g (6.7).

The system dynamics during the first 10 seconds of the simulation period is paramount in identifying the coherent groups where the footprints of the system non-linearities are evident. The dynamics are, in general, influenced by the generator models and the interactions among their controllers. For example, since GEN-9 is equipped with a fast acting static exciter and a PSS, it responds actively and differently to the faults as compared to the generators which are equipped with DC exciters or those under constant excitation. This even can result in the separation of GEN-9 into an area on its own, subsequent to a disturbance. However, if the oscillatory mode of GEN-9 is not excited, it tends to merge with GEN-8 and GEN-13 and form one area (as will be further discussed in Case III).

6.3.2 Case II - Fault at Bus-33

The system initial conditions are the same as those of Case I. The same fault as that of Case I is imposed on Bus-33 which results in the formation of 7 areas as given in Table 6.2.

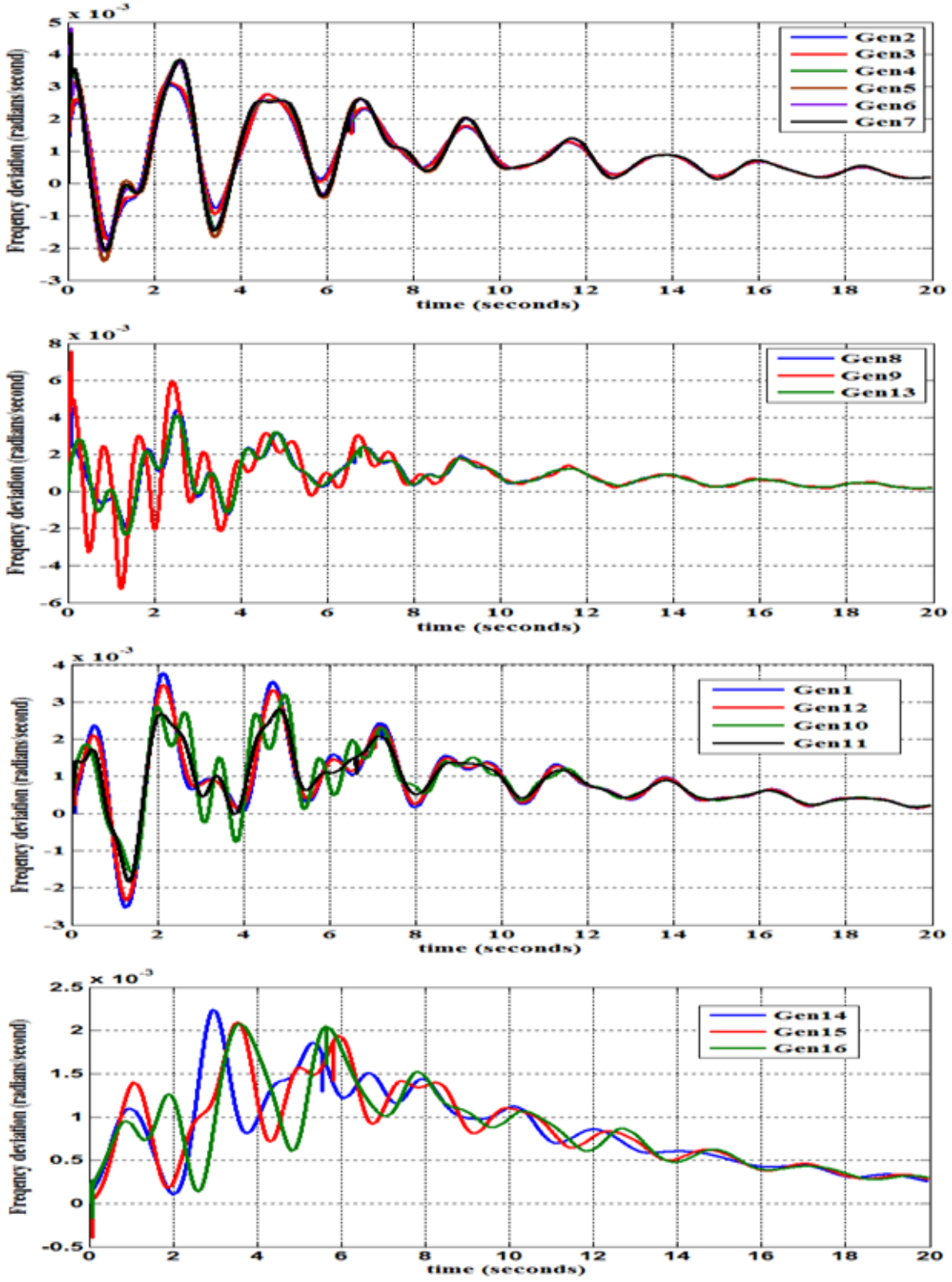

Figure 6.2: Simulated frequency deviation signals of the generator buses for case I

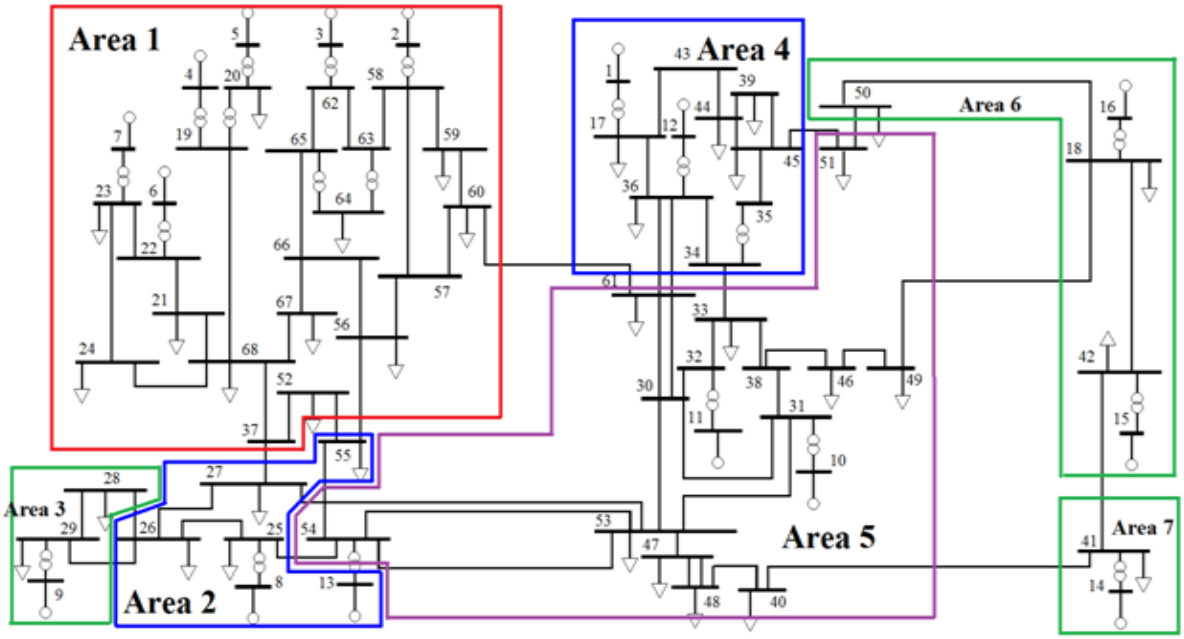

Figure 6.3: Areas corresponding to Case I

Table 6.2: Coherent groups and areas (Case II)

Area	Coherent Generators	Associated Non-Generator buses
1	9	28, 29
2	10	–
3	11	32, 33
4	14	41
5	15	42
6	16	18, 50
7	1, 2, 3, 4, 5, 6, 7, 8, 12, 13	All the remaining buses

Area 7 is a major one and contains 10 generators and 85% of the system non-generator buses. The other areas are smaller. Area 2 is formed only by GEN-10. GEN-14, GEN-15 and GEN-16 form separate areas. Moreover, the fault at Bus-33 results in the formation of Area 3 which is fully encapsulated by Area 7, as shown in Figure 6.4. This reveals that the system is dominated by and practically behaves as a single area and not affected by the fault when compared with Case I (and Case III as will be discussed subsequently). This, in case of the controlled-islanding, would have remained unnoticed in the system analysis process, if a model-based coherency identification method was used.

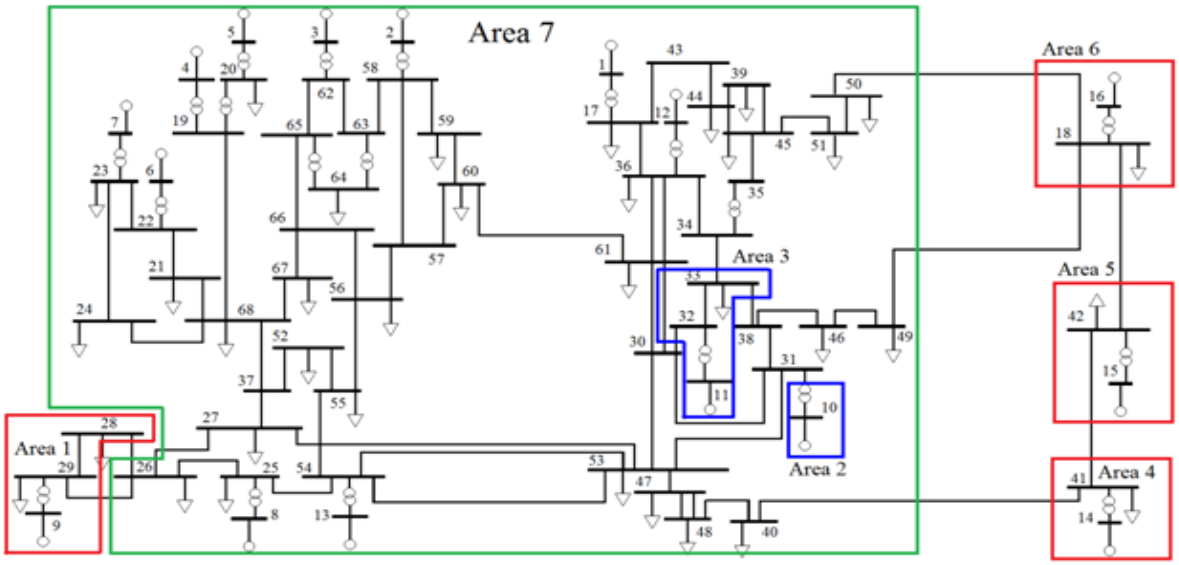

Figure 6.4: Areas corresponding to Case II

6.3.3 Case III - Fault at Bus-53

The system initial operating conditions are the same as those of Case I and Case II; however, the same fault is applied to Bus-53. The fault results in formation of 8 areas, Table 6.3, which is the maximum number of areas observed in all the performed case studies. In this case, GEN-9 merges with GEN-8 and GEN-13 into a single area, Figure 6.5. This is in contrast to the results of Case I and Case II. In this case, a set of non-generator buses (Bus-40, Bus-47, and Bus-48) are appended to an area which they are not directly connected to. Table 6.4 shows the CCs of these buses with respect to the COIFD vectors of areas 1-8. The reason for such a scenario is mainly the system configuration in which the fault at Bus-53 separates Bus-40, Bus-47 and Bus-48 from the rest of the system. This outcome can have ramifications for the currently implemented controlled-islanding schemes, i.e., this set of buses can neither be appended to any of the areas they have electrical connections to, nor can form a separate area as they do not include any generators. This indicates that potentially there is a need for modifications to the current controlled-islanding algorithms to account for such scenarios.

To show the superiority of the developed method, the DCD method is applied to System-1 and the results are compared with those obtained from (i) a model-based slow-coherency identification method and (ii) a measurement-based coherency identification method [3]. The study results demonstrate the degree of noise immunity of the DCD method as compared with those of the ICA and the PCA methods [3]. The results of these comparisons are given in Appendix D.

Table 6.3: Coherent groups and areas (Case III)

Areas	Coherent Generators	Associated Non-Generator buses
1	2,3,4,5,6,7	19,20,21,22,23,24,37,52,56,57, 58,59,60,62,63,64,65,66,67,68
2	8,9,13	25,26,27,28,29,53,54,55
3	1,12	17,30,33,34,35,36,39,40, 43,44,45,47,48,51,61
4	10	31,38,46,49
5	11	32
6	14	41
7	15	42
8	16	18,50

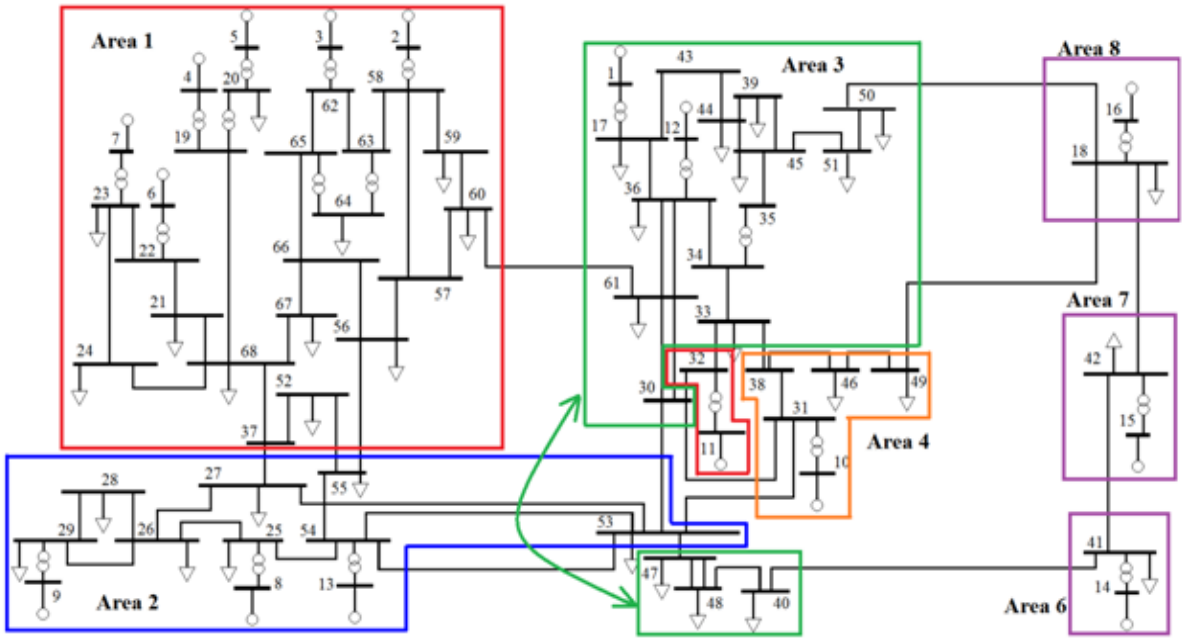

Figure 6.5: Areas corresponding to Case III

Table 6.4: Coherency Coefficients of the separated non-generator buses (Case III)

Areas	Bus 40	Bus 47	Bus 48
1	0.89	0.924	0.914
2	0.914	0.945	0.937
3	0.917	0.949	0.941
4	0.911	0.934	0.929
5	0.883	0.905	0.9
6	0.881	0.804	0.834
7	0.835	0.756	0.786
8	0.818	0.75	0.776

6.4 Wind Power Impacts on System Coherency

This section investigates the impacts of high-depth penetration of wind power on the system coherency. For the reported studies, the DCD method is used for coherency identification with the tight coherency limit of γ_c= 0.99 and the relaxed coherency limit of γ_r = 0.95. All the possible fault locations for the proposed study cases; i.e., Table 2.2, Table 2.3, and Table 2.4, were studied. However, faults at adjacent buses result in similar time-responses, three fault locations at Bus-25, Bus-56 and Bus-39 are selected to show the distinct impacts of wind power on the system coherency. These fault locations have distinct coherency structures at different wind power penetration levels and provide insight into the impacts of high-depth penetration of wind power on the system coherency. For all the selected fault locations, the system is initially at a steady-state condition and at time t=0s is subjected to a 5-cycle, self-cleared, 3-phase-to-ground fault. The simulation time-step is 1.667 ms and each simulation case provides 20 seconds of dynamic response of the system subsequent to the disturbance [68]. The simulated response is sampled at the rate of 120 Hz as encouraged by the IEEE standard for synchrophasor measurements [69].

It should be noted that for all WPPLs and WPP allocation patterns considered, different combinations of Type-3 and Type-4 WPPs resulted in different time-responses, i.e., different frequency deviation vectors. However, the same set of generators is affect for the different combinations of Type-3 and Type-4 WPPs since both types are connected to the same buses (Table 2.2, Table 2.3, and Table 2.4). Therefore, the same coherency structure is obtained independent of the percentage of Type-3 and Type-4 WPPs.

6.4.1 Fault at Bus-25

6.4.1.1 Base Case

This fault results in formation of eight areas in the base case as shown in Figure 6.6. Figure 6.6 shows that each of GEN-8, GEN-9, and GEN-13 forms a separate area. The reasons are that (i) the fault is directly imposed at the terminal of GEN-8 and thus it is the most affected generator and separates into an area without any associated non-generator buses and (ii) the static exciter and PSS (located at GEN-9) result in a time-response dissimilar to that of GEN-13 which is equipped with a DC excitation system. This eliminates the coherency between GEN-9 and GEN-13. GEN-10, in the New York system, forms a separate area due to the excitation of mode 17 of Table 2.1. For this mode, GEN-10 is the only contributing generator from the New York system. Moreover, the fault results in a coherency structure similar to that of Case III in Section 6.3.3 where

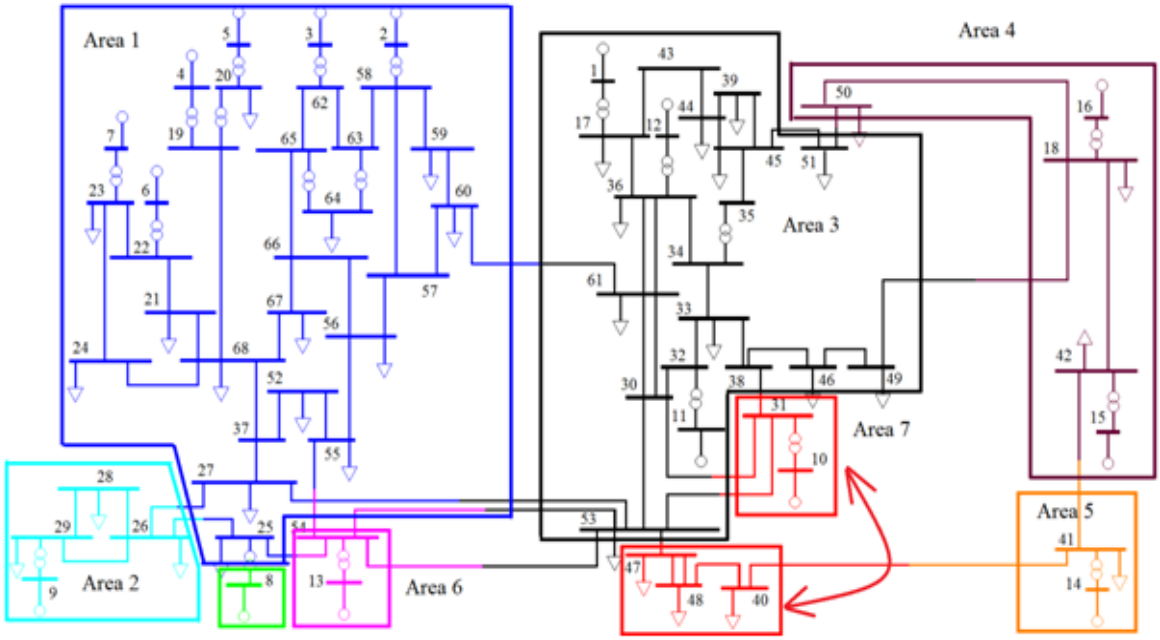

Figure 6.6: Coherency structure due to fault at Bus-25 for the base case

a group of non-generators buses are associated with an area which they are not directly connected to.

6.4.1.2 WPPL=5%

Figure 6.7 shows the coherency structure associated with 5% WPPL and the CD pattern study cases of Table 2.2. Figure 6.7 shows that:

i. The coherency structure corresponding to GEN-8, GEN-9 and GEN-13, as compared with the base case, does not change. The reason is that the WPPs are electrically remote and the depth of wind power penetration is low. Therefore, their impacts on this group of generators are insignificant. Thus, the base case coherency structure is preserved.

ii. The added WPPs divide Area 1 of Figure 6.6 into two areas where GEN-4 – GEN-7 form one area and the added WPPs and GEN-2 and GEN-3 constitute another area. The fast responses of the WPPs affect the time-response of GEN-2 and GEN-3 (the closest units to the added WPPs) and result in eliminating the coherency between GEN-2 and GEN-3 and GEN-4 – GEN-7. However, the sizes of the WPPs are not large enough for the time-responses of the WPPs to be completely distinct from those of GEN-2 and GEN-3 and thus the WPPs separate into a separate area.

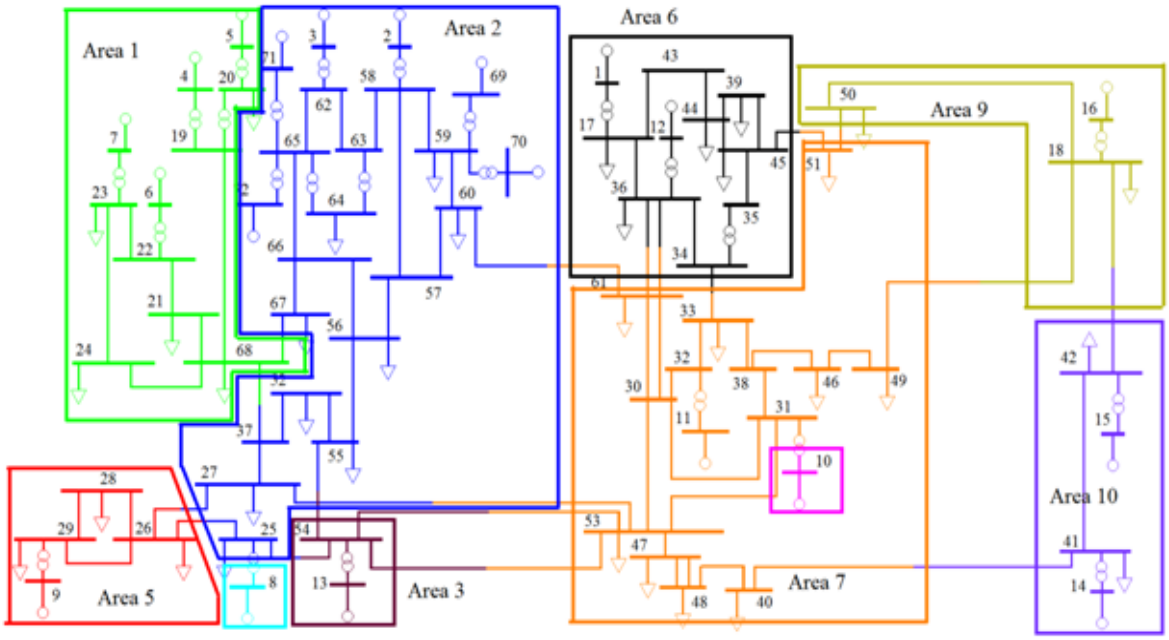

Figure 6.7: Coherency structure due to fault at Bus-25 for 5% WPPL case

iii. The WPPs affect mode 24 and decrease its damping, as discussed in Chapter 5. This effect results in separation of GEN-1 and GEN-12 into one area and GEN-11 forms another one. The reason is that the participation of GEN-1 and GEN-12 to mode 24 is much larger than that of GEN-11 and thus they are the mostly affected units by the decrease in the damping ratio of mode 24.

Changing the allocation pattern of WPPs to UD (Table 2.2) has no noticeable effect on the coherency structure. The reason is that for both patterns, the integration of WPPs is limited to Bus-59 and Bus-65 which are close to each other and remote from the fault location, i.e., Bus-25. Thus, the time-response of System-1 does not significantly change.

6.4.1.3 WPPL=15%

The coherency structure for 15% WPPL and the CD pattern (Table 2.3) is shown in Figure 6.8(a). The integration of WPPs results in formation of 14 areas compared to eight areas in the base case of Figure 6.6. For this WPPL and the WPPs allocation pattern:

i GEN-14, GEN-15 and GEN-16 each forms a separate area. The reason is that the WPPs in the New York system affect the dynamical response of GEN-16 and weaken its coherency with GEN-15.

ii Each of the Northern and Southern WPP groups form a separate area. The reason is that the WPPs are significantly large and their responses are distinct from their nearby generators and thus they form separate areas. In addition, the southern WPP group affects the dynamical responses of GEN-2 and GEN-3 and eliminates their coherency with GEN-4 - GEN-7 (as presented in the base case).

iii With respect to the New York system, even though the fault location is electrically remote from the WPPs, the WPPs are clustered such that their dynamical response is distinct from the synchronous generators of the New York system. Therefore they form a separate area which exhibits no coherency with any synchronous generator.

Figure 6.8(b) shows the coherency structure when the UD pattern is considered (Table 2.3). For the New York system, the WPPs are distributed over the system. Therefore, they do not have the same impact as they did in the CD pattern, Figure 6.8(a). Thus, the New York system preserves a similar coherency structure to that of the 5% WPPL as shown in Figure 6.7 where the WPPs are equally distributed among the different areas. For the Southern WPP group, the WPPs are located at both sides of the area formed by GEN-2 and GEN-3, i.e., Area 2 of Figure 6.8(b). Thus, they dominate the dynamical response of this area and are coherent with GEN-2 and GEN-3. With respect to the Northern WPP group, the WPPs are divided between two areas, Area 5 and Area 6 of Figure 6.8(b). The WPPs of Area 5 have a different time-response compared to those of Area 6 and thus they constitute a separate area. The reason is that GEN-9 and the WPPs of Area 6 are connected to the same bus which results in a "perfect coherency" scenario as discussed in Section 6.2.1. In addition, the response of GEN-9 is relatively fast as compared with those of the WPPs due to its static exciter and the PSS action. Thus, the time-response of Area 6 is not fully dominated by the WPPs dynamical response. This limits the WPPs of Area 6 from being coherent with those of Area 5, even though they are electrically very close.

For the 30% WPPL, the same coherency structure as that of the 15% WPPL is preserved except that the WPPs of the New York system always form separate areas. The reason is that the sizes of the WPPs are large enough such that their time-response is always distinct and dominant larger parts of the power system.

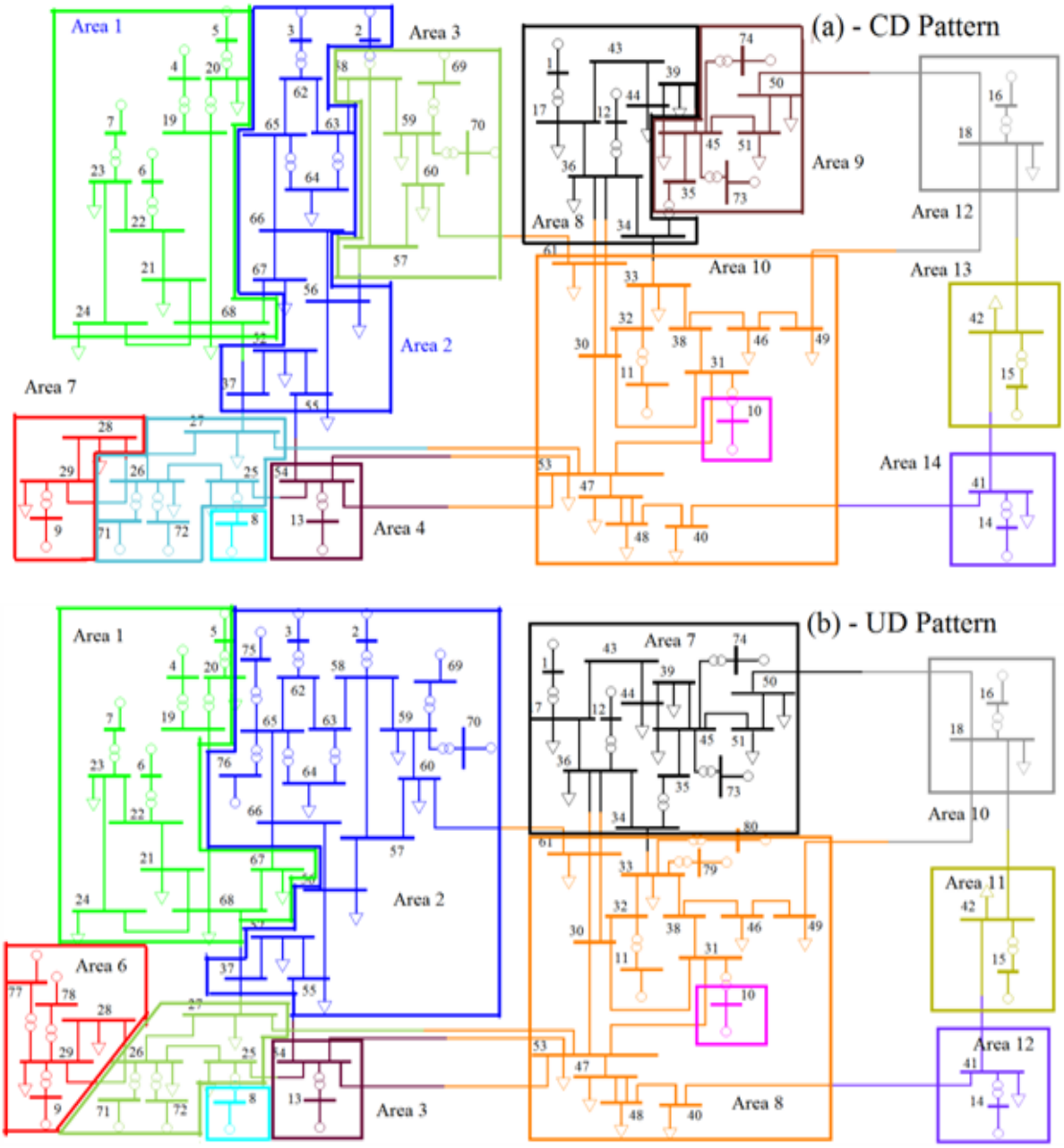

Figure 6.8: Coherency structures due to fault at Bus-25 for 15% WPPL case

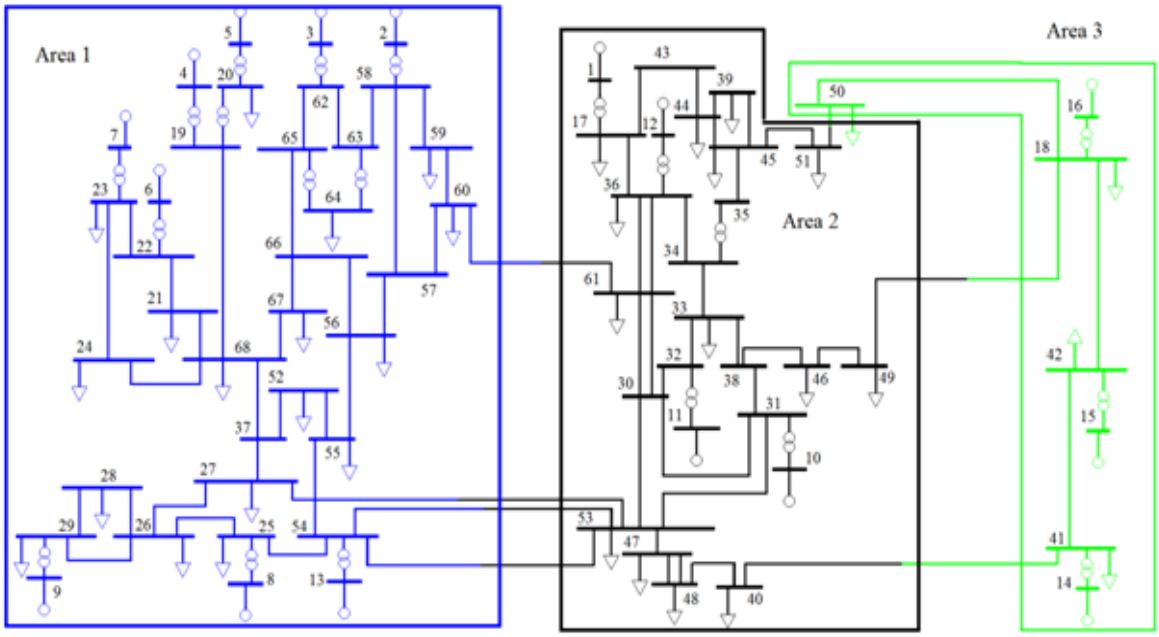

Figure 6.9: Coherency structure due to fault at Bus-56 for the base case

6.4.2 Fault at Bus-56

6.4.2.1 Base Case

This fault location is considered because it is in the middle of the New England system and its effect is equally distributed between the Northern and Southern WPP groups. For the base case, this fault results in forming three areas where the New England and New York systems form separate areas and GEN-14, GEN-15, and GEN-16 form another one as shown in Figure 6.9.

6.4.2.2 WPPL = 5%

For 5% WPPL (Table 2.2), the coherency structures for the CD and UD patterns are shown in Figure 6.10(a) and (b) respectively. For both patterns, the fault separates the New England system into five areas where:

i. The WPPs form separate areas for both CD and UD patterns. For the UD pattern, even though the WPPs are distributed, the fault is electrically close to the WPPs such that their dynamical responses are significantly affected. This prevents the WPPs from being coherent with GEN-2 and GEN-3 as in the case of the fault at Bus-25, Figure 6.7.

ii. GEN-9 separates into an area due to the excitation of its local mode.

iii. The WPPs affect the dynamical response of GEN-2 and GEN-3 and thus eliminate the coherency between GEN-2 - GEN-7 in the base case of Figure 6.9.

With respect of the New York system, the base case coherency structure breaks down into two areas. This is due to the impact on the inter-area oscillatory mode (mode 24 of Table 2.1) between GEN-2 – GEN-7 in the New England system and those of the New York system.

6.4.2.3 WPPL=15%

Figure 6.11(a) shows the coherency structure for 15% WPPL and CD pattern (Table 2.3) where each WPP group forms a separate area and a coherency structure similar to that of Figure 6.10(a) is preserved. However, with the UD pattern, Figure 6.11(b), the impact of the fault on the dynamical response of the New York system is not significant and since most of the wind power is located in the New England system, the WPPs do not form a separate area. Moreover, the Northern WPP group joins GEN-9 to form an area. The reason is that the added WPPs at Bus-29 and Bus-26 significantly change the dynamical response of GEN-9 such that it becomes coherent with them.

For the 30% WPPL, WPPs located in the New York system always form separate areas and the remaining of System-1 preserves the same coherency structure as the one of 15% WPPL. The reason is that more wind power is located in the New York system and thus the impact of the WPPs is significant for both CD and UD patterns.

6.4.3 Fault at Bus-39

This fault location is selected to investigate the impact of the added WPPs on the coherency structure of the New York system. The reason is that this fault location has minimal impact on the New England system. This is evident from studying the impact of the fault on the New England coherency structure. For this fault, the New England system (i) preserves the same coherency structure for all the investigated WPPLs and (ii) is composed of two areas formed by (a) GEN-4 – GEN-7 and (b) the remaining generators and all the added WPPs as shown in Figure 6.12. For the New York system, whenever WPPs are added, they form separate areas and the remaining generators preserve the same coherency structure as the base case of Figure 6.13. This fault case shows that the impact of wind power on the system coherency, in some cases, is limited to the formation of new areas that are totally dominated by the added WPPs and the base case coherency structure of the synchronous generators is preserved.

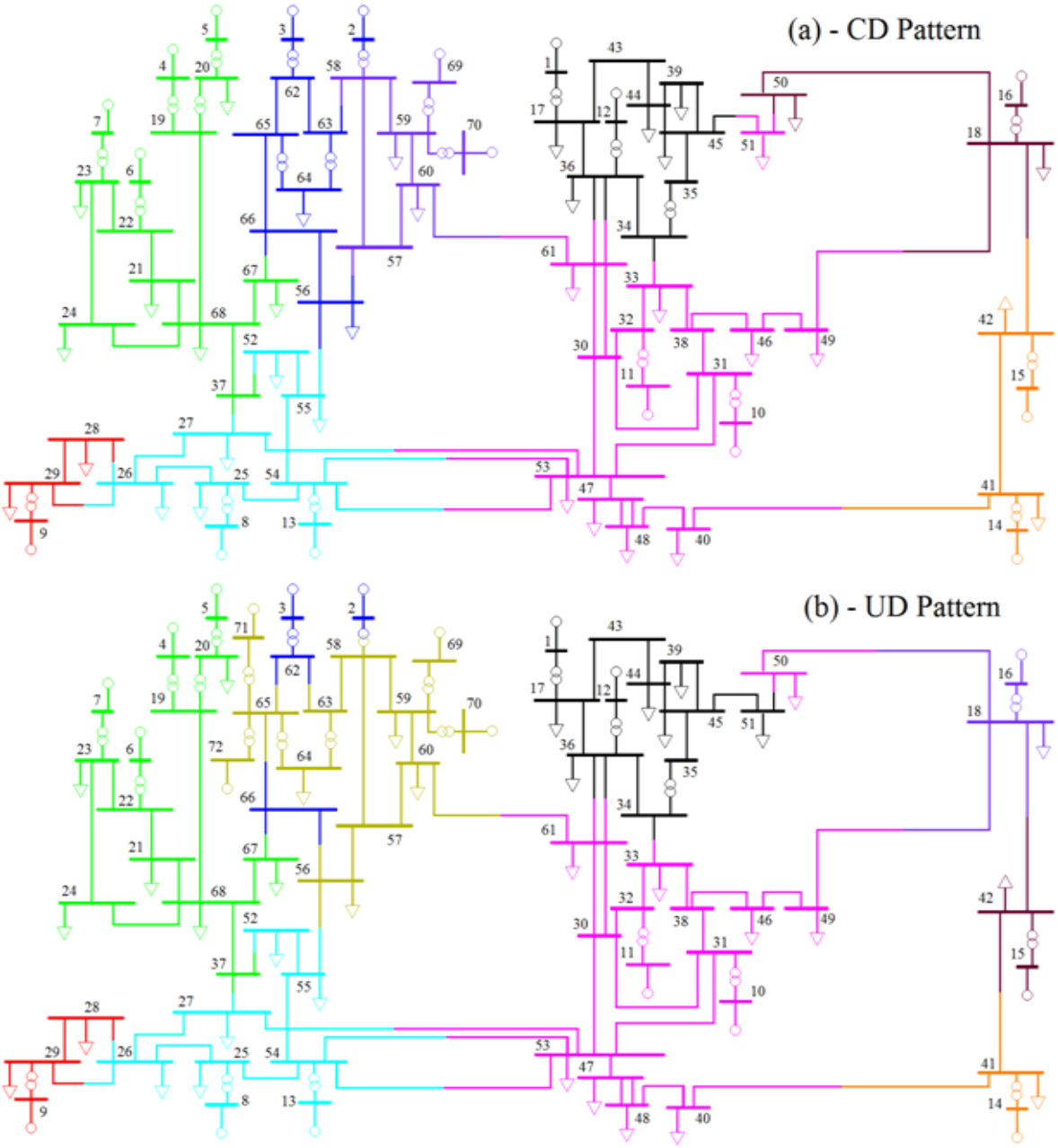

Figure 6.10: Coherency structures due to fault at Bus-56 for 5% WPPL case

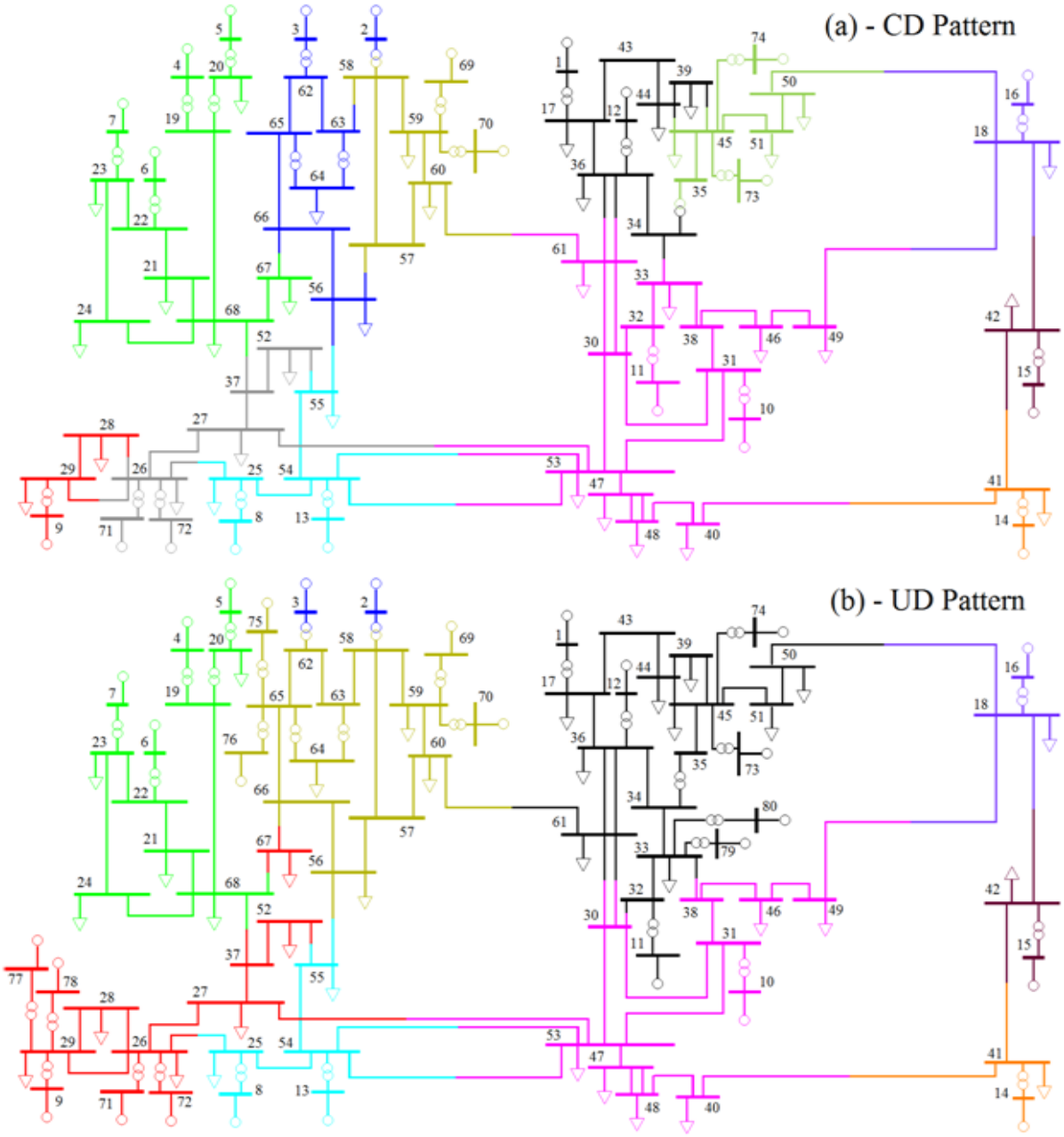

Figure 6.11: Coherency structures due to fault at Bus-56 for 15% WPPL case

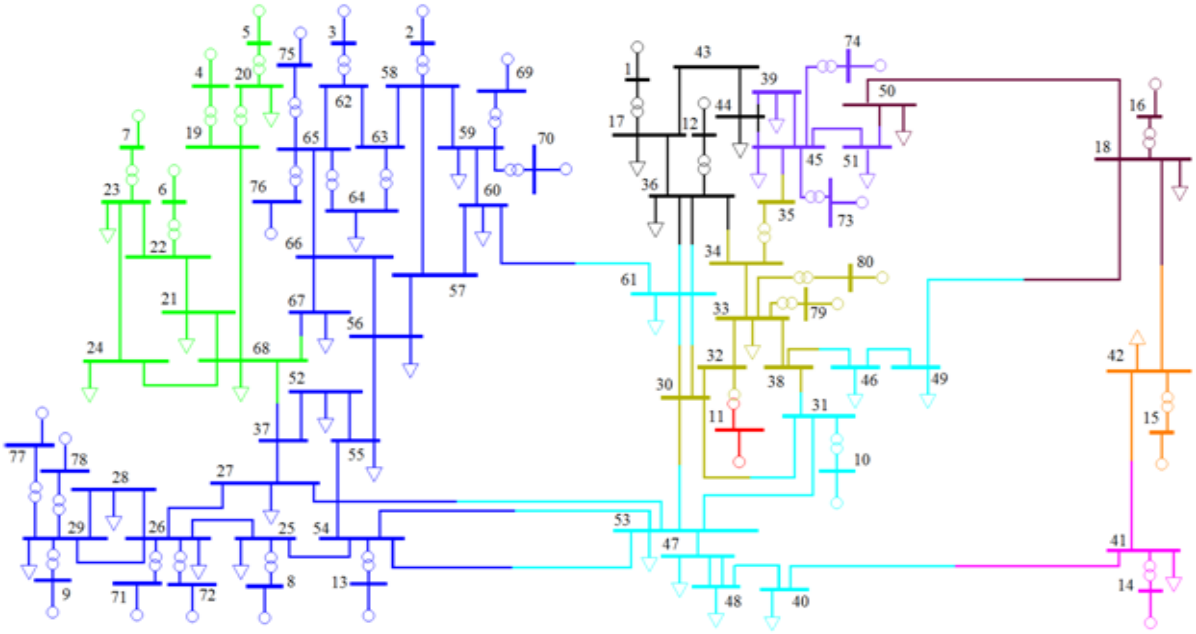

Figure 6.12: Coherency structures due to fault at Bus-39 different WPPLs cases

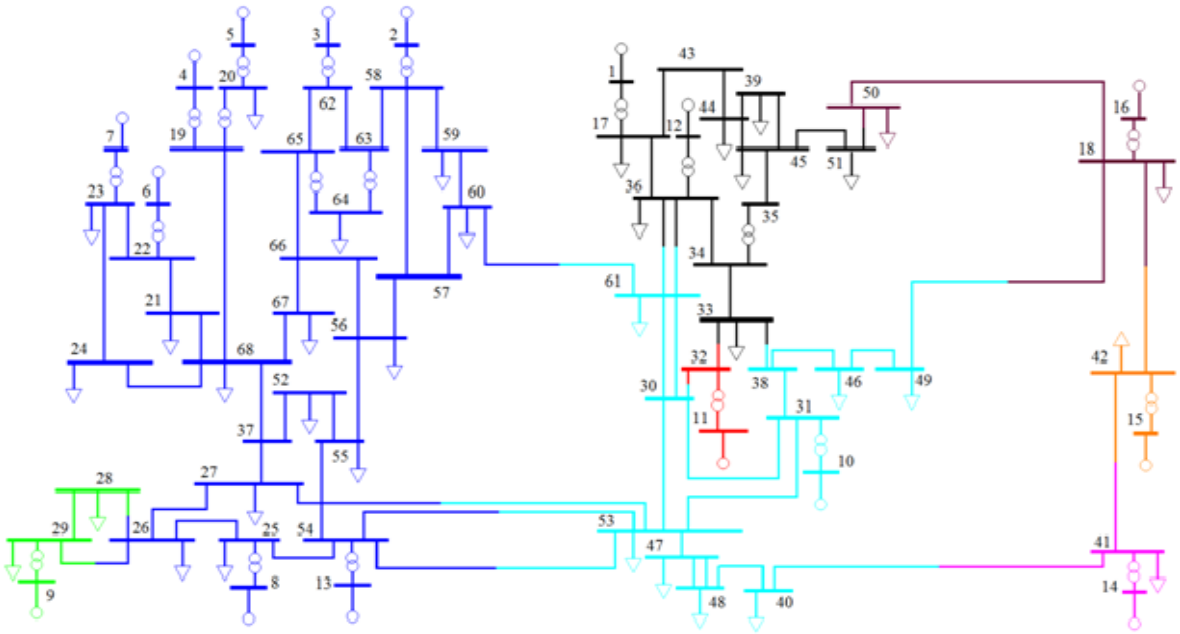

Figure 6.13: Coherency structures due to fault at Bus-39 for the base case

6.5 Conclusions

This chapter presents a new method for identification of the dynamic evolution of coherency in interconnected power systems. The developed DCD method is based on the bus frequency deviation signals which are equally identifiable for WPPs and non-generator buses. The main feature of the developed DCD method is its ability to identify the coherent groups of a power system including WPPs. Other coherency identification methods lack this feature which limited investigation of the impacts of wind power integration on power system coherency. The developed DCD method also includes the procedure for partitioning the system into electrical areas by identifying the associated non-generator buses with each group of coherent generators. Applying the DCD method to System-1 in its base case shows new coherency structures. For example, a group of non-generator buses being appended to an area that they are not directly connected to, nor can form a separate area as they do not include any generators. This outcome can have ramifications for the currently implemented controlled-islanding schemes and indicates that potentially there is a need for modifications to the current controlled-islanding algorithms to account for such scenarios.

This chapter applies the developed DCD method on System-1, based on the study cases presented in Chapter 2, to quantify the impact of high-depth penetration of wind power on the system coherency structure. The study results shows:

- Addition of WPPs to a power system results in altering the coherency structure of the base case to larger number of areas due to the impact of the added WPPs on the time-responses of the system synchronous generators.

- At low WPPLs, the sizes of the WPPs are not large enough for their time-responses to be completely distinct from those of the nearby synchronous generators. Thus, the WPPs are coherent with the synchronous generators. However, if the fault location is electrically close to the WPPs, they will always form separate areas even at low WPPLs.

- As the WPPL increases, the added WPPs will always form separate areas. The reason is that the size of the WPPs will be large enough such that their time-responses are always distinct and dominate larger parts of the power system.

- Based on the WPPs allocation patterns, the impact of wind power on the system coherency is limited to the formation of new areas that are totally dominated by the added WPPs and the base case coherency structure of the synchronous generators is preserved.

Chapter 7

Conclusions, Contributions and Future Work

7.1 Thesis Summary

The objective of this thesis is to investigate the impact of wind power integration on dynamic behavior of large interconnected power systems with respect to transient stability and low-frequency (0.1-2Hz) oscillatory modes. However, due to the lack/inadequacy of the required models, analytical tools and digital time-domain simulation environments, this thesis:

- Developed enhanced nonlinear and linearized models of Wind Power Plants (WPPs) which utilize Type-3 and Type-4 wind generation units.
- Developed an eigen analysis tool and digital time-domain simulation software platform for application to large power systems that include Type-3 and Type-4 WPPs, using the above mentioned models. Both software platforms are MATLAB-based.
- Developed a dynamic coherency identification method that can represent the impact of WPPs in the coherency phenomenon.

Based on the above developments, the thesis conducted a set of comprehensive and systematic studies to evaluate the impacts of (i) depth of penetration of wind power, (ii) locations of WPPs and (iii) type of WPPs on the transient stability, damping ratios of the low-frequency oscillatory modes and the coherency phenomena. The studies were conducted on a test system that represents the New York/New England interconnected power system. The conclusions are as follows.

7.2 Conclusions

This thesis concludes that:

- The documented models of Type-3 and Type-4 WPPs either omit or add parts to the generic models which are not defined as integral parts of these generic models and thus they cannot be used to replicate the time-response of the built-in generic models of the PSS/E software.

- The extracted linearized models of Type-3 and Type-4 WPPs accurately match the time-responses of the non-linear models, when subjected to small-signal disturbances.

- The non-linear model of Type-3 WPP can only be linearized under certain conditions otherwise multiple linear models are required to properly/accurately represent the non-linear model. However, the Type-4 WPP can be represented by a single small-signal (linear) dynamic model.

- Addition of WPPs does not introduce new inter-area oscillatory modes. However, it can impact the existing ones. The reason is that the WPPs do not change the inertia distribution of the system.

- The impact of adding WPPs is limited to changing the damping ratios of inter-area modes while their corresponding oscillation frequencies are insignificantly affected.

- The impact of WPPs on the damping ratio of an inter-area mode is determined based of the location(s) of the added WPP(s) with respect to the power exchange between areas. If the added WPPs increase the power exchange between two areas then the damping of the inter-area mode corresponding to these two areas will decrease.

- The impact on the local plant modes is related to interactions among the reactive power controllers of the WPPs and the excitation systems of the affected generators. With the increase in reactive power injected by the synchronous generators due to addition of WPPs and load increase, the slow response of the DC exciters located at the affected synchronous generators is limiting these generators from coping with the fast response of the reactive power controllers of the nearby WPPs.

- Addition of WPPs to a system introduces new oscillatory modes that are categorized as (i) Type-3 Modes, (ii) Common Modes, and (iii) Mutual Modes. Type-3

modes are associated with the wind turbine of Type-3 WPPs and are neither affected by the WPPL nor the WPP location. This is due to the fast responses of the rotor-connected converter and its controllers. Common modes are associated with the WPP converter and its controllers and exist regardless the WPP type. The reason is that both WPP types adopt nearly the same controller structure. Mutual modes exist when both WPP types exist in the system and result from interactions between the controllers of Type-3 and Type-4 WPPs. Such interactions are due to the difference in the parameters values of the controllers of both WPP types

- As the penetration level of wind power increases, System-1 exhibits higher degree of nonlinearity and the impact of wind power on System-1 transient stability can be determined only from the time-domain simulation of the system nonlinear model. This indicates that the results of the transient stability assessment of System-1 for lower WPPLs cannot be extrapolated to higher WPPLs.

- The developed method for dynamic coherency identification (i) is capable of identify the coherent groups of a power system including WPPs and (ii) includes the procedure for partitioning the system into electrical areas by identifying the associated non-generator buses with each group of coherent generators.

- Addition of WPPs to a power system results in breaking the coherency structure of the base case to larger number of areas due to the impact of the added WPPs on the time-responses of the system synchronous generators.

- At low WPPLs, the sizes of the WPPs are not large enough for their time-responses to be completely distinct from those of the nearby synchronous generators. Thus, the WPPs are coherent with the synchronous generators. However, if the fault location is electrical close to the WPPs, they will always form separate areas even at low WPPLs.

- As the WPPL increases, the added WPPs will always form separate areas even for remote fault locations. The reason is that the size of the WPPs will be large enough such that their time-responses are always distinct and dominate larger parts of the power system.

- Based on the WPPs allocation patterns, the impact of wind power on the system coherency, is limited to the formation of new areas that are totally dominated by the added WPPs and the base case coherency structure of the synchronous generators is preserved

7.3 Original Contributions

The salient contributions of this thesis are:

- Developing and validating enhanced non-linear equivalent models of Type-3 and Type-4 WPPs that are implementable in any digital time-domain simulation platform.
- Developing and validating linearized models of Type-3 and Type-4 WPPs, extracted from their corresponding enhanced, non-linear, equivalent models, for eigen analysis of large power systems including WPPs.
- Introducing and developing a dynamic coherency identification method that can account for the impacts of WPPs.
- Explaining the reasons for the contradicting conclusions, with respect to the impact of wind power on transient stability and low-frequency dynamics of power systems that have been reported in the technical literature.
- Identifying the impacts of wind power on power system coherency which have not been addressed previously in the technical literature.

7.4 Future Work

The proposed further research in continuation of this work can include:

- Implementing the next generation models of Type-3 and Type-4 WPPs which include further details of WPPs, e.g. crowbar protection. The second generation models contain larger number of switching logics.
- Systematic design and performance evaluation of power system controls, e.g., power system stabilizers and automatic generation control, to enhance transient stability and mitigate low-frequency dynamics of the power system in the presence of wind power.
- Development of control strategies for WPPs to participate in the power system transient stability enhancement in coordination with the existing controls, e.g., power system stabilizers and fast valving.

Appendix A

Non-zero Elements of the Linearized Model of Type-3 WPP

The non-zero elements of (3.60) and (3.61) are given by:

$$a_{1,1} = \frac{-1}{T_{iqCMD}}, \quad a_{1,14} = \frac{-1}{T_{iqCMD}X_{eq}}, \quad a_{2,2} = \frac{-1}{T_{ipCMD}}, \quad a_{2,8} = \frac{P_{rated}}{T_{ipCMD}S_{rated}V^{(o)}},$$
$$a_{3,3} = \frac{-1}{T_{LVPL}}, \quad a_{4,4} = \omega_o, \quad a_{4,5} = V^{(o)}K_{PLL}, \quad a_{5,5} = \frac{K_{i_{PLL}}V^{(o)}K_{PLL}}{\omega_o}, \quad a_{6,6} = \frac{-1}{T_{power}},$$
$$a_{6,2} = \frac{1}{T_{power}} \times \frac{\partial f(VI_{P_{LVPL}})}{\partial I_{P_{LVPL}}}, \quad a_{7,6} = -K_{it}, \quad a_{7,15} = K_{it}, \quad a_{8,6} = \frac{-K_{pt}\omega^{(o)}}{T_{fp}},$$
$$a_{8,7} = \frac{\omega^{(o)}}{T_{fp}}, \quad a_{8,8} = \frac{-1}{T_{fp}}, \quad a_{8,15} = \frac{{x_\omega}^{(o)} + 2K_{pt}\omega^{(o)} - K_{pt}{\omega_{ref}}^{(o)}}{T_{fp}}, \quad a_{9,9} = \frac{-1}{T_{RV}},$$
$$a_{10,9} = \frac{-K_{iv}y_{frz}}{f_n}, \quad a_{11,9} = \frac{-K_{pv}y_{frz}}{T_V f_n}, \quad a_{11,11} = \frac{-K_{pv}y_{frz}}{T_V}, \quad a_{12,10} = \frac{1}{T_{fV}},$$
$$a_{12,11} = \frac{1}{T_{fV}}, \quad a_{12,12} = \frac{-1}{T_{fV}}, \quad a_{13,1} = K_{qi}V^{(o)}, \quad a_{13,12} = K_{qi}, \quad a_{14,13} = K_{qv},$$
$$a_{15,2} = \frac{-V^{(o)}}{2H\omega^{(o)}}, \quad a_{16,6} = -K_{ip}y_p, \quad a_{15,15} = \frac{1}{2H(\omega^{(o)})^2}(V^{(o)}{I_{P_{LVPL}}}^{(o)} - P_{m_o}),$$
$$a_{16,15} = K_{ip}y_p, \quad a_{15,18} = \frac{-K_{aero}{\theta_{lim}}^{(o)}}{2H\omega^{(o)}}, \quad a_{17,8} = K_{ic}y_c, \quad a_{18,6} = \frac{-K_{PP}}{T_p},$$
$$a_{18,8} = \frac{K_{PC}}{T_p}, \quad a_{18,15} = \frac{K_{PP}}{T_p}, \quad a_{18,16} = \frac{1}{T_p}, \quad a_{18,17} = \frac{1}{T_p}, \quad a_{18,18} = \frac{-1}{T_p}.$$
$$b_{10,1} = \frac{K_{iv}y_{frz}}{f_n}, \quad b_{11,1} = \frac{K_{pv}y_{frz}}{T_V f_n}, \quad b_{17,2} = -K_{ic}y_c, \quad b_{18,2} = \frac{-K_{pc}}{T_p}.$$
$$h_{2,2} = \frac{-P_{rated}{P_{ord_{lim}}}^{(o)}}{T_{ipCMD}S_{rated}(V^{(o)})^2}, \quad h_{3,2} = \frac{-1}{T_{LVPL}}, \quad h_{4,1} = -V^{(o)}K_{PLL},$$
$$h_{5,1} = \frac{-K_{i_{PLL}}K_{PLL}V^{(o)}}{\omega_o}, \quad h_{9,2} = \frac{1}{T_{RV}}, \quad h_{6,2} = \frac{1}{T_{power}} \times \frac{\partial f(VI_{P_{LVPL}})}{\partial V},$$
$$h_{13,2} = K_{qi}\left({I_Q}^{(o)} + \frac{2V^{(o)}}{X_{eq}}\right), \quad h_{14,2} = -K_{qv}, \quad h_{15,2} = \frac{-{I_{P_{LVPL}}}^{(o)}}{2H\omega^{(o)}}.$$
$$l_{1,2} = \frac{-NS_{rated}}{S_{base}}, \quad l_{2,1} = \frac{-NS_{rated}}{S_{base}}, \quad n_{1,3} = 1, \quad n_{2,2} = \frac{-NS_{rated}}{S_{base}X_{eq}}, \quad n_{2,4} = 1$$

Appendix B

Type-3 and Type-4 WPPs Enhanced Equivalent Models Data

Table B.1: Type-3-E Generator/Converter Data

T_{iqCMD}	X_{eq}	V_{lim}	K_{hv}	I_{lim}	R_{ip}	T_{ipCMD}	G_{LVPL}
0.02	0.8	1.2	0.7	-2	5	0.02	1.11
V_{LVPL1}	V_{LVPL2}	T_{LVPL}	$LVPnT0$	$LVPnT1$	K_{PLL}	K_{iPLL}	PLL_{max}
0.5	0.9	0.02	0.4	0.8	0	0	0.1

Table B.2: Type-3-E Pitch Angle Control Data

K_{ip}	K_{pp}	K_{ic}	K_{pc}	P_{ref}
25	150	30	3	1
RT_{mn}	RT_{mx}	Tp	θ_{min}	θ_{max}
-10	10	0.3	0	27

Table B.3: Type-3-E Converter Control Data

T_{power}	K_{it}	K_{pt}	RP_{mn}	RP_{mx}	T_{fp}	P_{mn}	$\mathrm{P_{mx}}$
5	0.6	3	-0.45	0.45	0.05	0.04	1.12
P_{rated}	S_{rated}	$I_{P_{max}}$	T_{RV}	K_{iv}	f_n	K_{pv}	T_v
1.5	1.67	1.1	0.02	5	1	18	0.05
V_{frz}	Q_{mn}	Q_{mx}	T_{fv}	K_{qi}	$V_{min_{CL}}$	$V_{max_{CL}}$	K_{qv}
0.7	-0.436	0.436	0.15	0.1	0.9	1.1	40
			XIQ_{mn}	XIQ_{mx}			
			0.5	1.45			

Table B.4: Type-3-E Generated Active power – Reference Speed Piece-Wise Linear Characteristics ($f(P_{gen})$)

$\omega_{P_{mn}}$	$\omega_{P_{20\%}}$	$\omega_{P_{40\%}}$	$\omega_{P_{60\%}}$	P_{min}	$\omega_{P_{100\%}}$
0.3	0.69	0.78	0.98	0.74	1.2

Table B.5: Type-3-E Wind Turbine Data

H	D	K_{aero}
4.95	0	0.007

Table B.6: Type-4-E Generator/Converter Data

T_{iqCMD}	V_{lim}	K_{hv}	I_{lim}	R_{ip}	T_{ipCMD}
0.02	1.2	0.7	-2	2	0.02
G_{LVPL}	V_{LVPL1}	V_{LVPL2}	T_{LVPL}	$LVPnT0$	$LVPnT1$
1.11	0.4	0.9	0.02	0.4	0.8

Table B.7: Type-4-E Converter Control Data

T_{power}	K_{it}	K_{pt}	K_f	T_f	P_{mn}	P_{mx}	T_{RV}
0.05	0.1	0.05	0	0.08	-0.5	0.5	0.02
K_{iv}	T_v	K_{pv}	K_{qi}	V_{frz}	Q_{mn}	Q_{mx}	T_{fv}
5	0.05	18	0.1	0.7	0.47	-0.47	0.15
	$V_{min_{CL}}$	$V_{max_{CL}}$	K_{qv}	$I_{P_{hl}}$	$I_{q_{hl}}$	I_{maxTD}	
	0.9	1.1	120	1.11	1.11	1.7	

Appendix C

System-2 Data

Table C.1: System-2 Bus Data

Bus	kV Base	Type	P_G (MW)	P_L (MW)	Q_L (MVAr)	MVA Base
1	345	Swing	-	-	-	100
2	0.575	PV	100	-	-	Rated MVA
3	345	PQ	-	150	12.5	-

The large system is modeled as a constant voltage source behind a reactance of j0.05 pu on the system base.

Table C.2: System-2 Line Data

From Bus	To Bus	R	X	B	Tap Ratio
1	3	0.0013	0.02	0	1
1	3	0.0013	0.02	0	1
3	2	0	0.026	0	1

The values are in pu based on 100 MVA.

Table C.3: Power Flow Data of Type-3 and Type-4 WTG units

	P_{rated} (MW)	S_{rated} (MVA)	P_{min} (MW)	Q_{max} (MVAr)	Q_{min} (MVAr)
Type-3	1.5	1.67	0.07	0.726	-0.726
Type-4	2.5	3	0	1.2	-1.2

Appendix D

Comparisons of the DCD Method with Other Coherency Determination Methods

D.1 Comparison with the Slow-Coherency Method

Applying the slow-coherency method to System-1, using the same initial conditions considered in the reported Case I to Case III, provides the coherent groups and areas as given in Table D.1 [1]. These groups and areas are fixed and remain unchanged based on the definition of the slow-coherency identification method. Therefore, the results of Table D.1 are not necessarily representative of all possible formations of coherent groups after a large-signal dynamic disturbance or a major change in the operational condition. Under large-signal disturbances, the definition of slow-coherency is not necessarily valid and this can be confirmed by comparing the results of Table 6.1 (DCD method) and those of Table D.2 (the classical slow-coherency method). This comparison shows that (i) number of areas, (ii) coherent generators within each area, and (iii) the associated non-generator buses in each area, can be drastically different for the two case studies. The main feature of the developed DCD method is that it captures the impact of system changes and accordingly identifies coherent generators and areas.

Table D.1: Coherent groups and areas (Slow-Coherency method [1, 2])

Areas	Coherent Generators	Associated Non-Generator Buses
1	15	42
2	14	40, 41, 47, 48
3	16	18, 49, 50
4	2, 3, 4, 5, 6, 7, 8, 9, 13	19, 20, 21, 22, 23, 24, 25, 26, 27, 28, 29, 37, 52, 54, 55, 56, 57, 58, 59, 60, 62, 63, 64, 65, 66, 67, 68
5	1, 10, 11, 12	17, 30, 31, 32, 33, 34, 35, 36, 38, 39, 43, 44, 45, 46, 51, 53, 61

D.2 Comparison with Measurements-Based Methods

Reference [3] applies a measurement-based method, based on the Independent Component Analysis approach, to System-1 and the results are reported in Table D.2. Reference [3] assumes DC excitation systems for those generators which are not under constant excitation. The disturbance is due to a 10% increase in the mechanical input power of all generators for 80 ms. Table D.3 shows the results from the developed DCD method when the operating conditions and the disturbance are the same as those of [3]. It should be noted that when GEN-9 in System-1 is equipped with a DC exciter and the PSS is disabled, the DCD method, provides the same results as those of Table D.2. Comparison of Table D.2 and Table D.3 highlights the differences in the corresponding results. In Table D.3, GEN-9 and Bus-28 and Bus-29 form a separate area, and GEN-11 and Bus-32 also form an area. The reason for the differences between the results of the two tables is the presence of the static exciter and PSS at GEN-9.

The above comparison reveals that the proposed DCD method is able to identify the same coherent groups and areas as the ICA method but with the advantage of lower computation burden. Comparing the structures of the proposed DCD and the ICA methods indicates that the DCD method is computationally more efficient than the ICA method. The reason is that the DCD method is based on processing the signals in the time-domain with an iterative loop as explained in Section 6.2. The maximum number of iteration in any case studied did not exceed 6 iterations. However, the ICA method analyzes the measured signals in the frequency-domain, based on Discrete Fourier Transform, in addition to an algorithm that utilizes an iterative technique to obtain the mixing matrix (A) and the ICA matrix (S) [3].

Table D.2: Coherent groups and areas (method of [3])

Areas	Coherent Generators	Associated Non-Generator Buses
1	15	42
2	14	41
3	16	18
4	2, 3, 4, 5, 6, 7, 8, 9, 13	19, 20, 21, 22, 23, 24, 25, 26, 27, 28, 29, 37, 52, 54, 55, 56, 57, 58, 59, 60, 62, 63, 64, 65, 66, 67, 68
5	1, 10, 11, 12	17, 30, 31, 32, 33, 34, 35, 36, 38, 39, 40, 43, 44, 45, 46, 47, 48, 49, 50, 51, 53, 61

Table D.3: Coherent groups and areas (DCD method)

Areas	Coherent Generators	Associated Non-Generator Buses
1	15	42
2	14	41
3	16	18
4	2, 3, 4, 5, 6, 7, 8, 13	19, 20, 21, 22, 23, 24, 25, 26, 27, 37, 52, 54, 55, 56, 57, 58, 59, 60, 62, 63, 64, 65, 66, 67, 68
5	1, 10, 12	17, 30, 31, 33, 34, 35, 36, 38, 39, 40, 43, 44, 45, 46, 47, 48, 49, 50, 51, 53, 61
6	9	28, 29
7	11	32

D.3 Performance under Noise

The performance of the developed DCD method is tested under the presence of white Gaussian noise with the Noise-to-Signal Ratio (SNR) of:

$$SNR_{db} = 20log_{10}\left(\frac{A_{signal}}{A_{noise}}\right), \tag{D.1}$$

where A_{signal} is the root-mean-square value of the noise-free measured signal and A_{noise} is the root-mean-square value of the added noise. Noise-free DCD-based coherency identification results constitute the base case and the SNR value is initially selected at 50db and decreased in steps of 5db until the deviations from the base case is observed. For all the three studied cases, this occurs at SNR value less than 20db and the least coherent generator is the first to separate from its coherent group due to the increased discrepancy in its frequency deviation vector and the COIFD vector of the remaining generators. For Case I, area 6 is divided and GEN-15 and GEN-16 form separate areas. In Case II, GEN-13 is the first generator to form a separate group and this is followed by GEN-1 and GEN-12 at lower value of SNR (15db). In Case III, GEN-9 separates from area 2

and forms a new area.

To compare the developed DCD method with the PCA and ICA methods, the same system and disturbance that have been reported in [3] are considered. The developed DCD method is capable to identify the same coherent groups at noise levels higher than SNR = 20db. At this noise level, based on the DCD method, area 5 of Table D.3 breaks down into 4 separate areas. Comparing the results to those of the PCA and ICA methods [3], indicates that the noise immunity of the proposed DCD method is valid for SNR values as low as 20db while those of the PCA and ICA methods are limited to 50db and 25db, respectively. Since the slow coherency methods are not data-driven methods, noise sensitivity analysis does not apply.

Bibliography

[1] S. Yusof, G. Rogers, and R. Alden, "Slow coherency based network partitioning including load buses," *Power Systems, IEEE Transactions on*, vol. 8, no. 3, pp. 1375–1382, 1993.

[2] G. Rogers, *Power Systems Oscillations*. Kluwer, 2000.

[3] M. A. M. Ariff and B. C. Pal, "Coherency identification in interconnected power system-an independent component analysis approach," *Power Systems, IEEE Transactions on*, vol. 28, no. 2, pp. 1747–1755, 2013.

[4] I. A. Hiskens, "Dynamics of type-3 wind turbine generator models," *Power Systems, IEEE Transactions on*, vol. 27, no. 1, pp. 465–474, 2012.

[5] Global Wind Energy Council, "Annual market update 2013: Global wind report," *GWEC, Brussels*, 2014. [Online]. Available: http://www.gwec.net/wp-content/uploads/2014/04/GWEC-Global-Wind-Report_9-April-2014.pdf

[6] Global Wind Energy Council, "Annual market update 2014: Global wind report," *GWEC, Brussels*, 2015. [Online]. Available: http://www.gwec.net/wp-content/uploads/2015/03/GWEC_Global_Wind_2014_Report_LR.pdf

[7] California Energy Commission, "Alta wind energy center is the nation's largest wind facility." [Online]. Available: http://www.energy.ca.gov/tour/alta/

[8] Working Group 8 of Study Committee C6, "Grid integration of wind generation," CIGRE, Tech. Rep., February 2011.

[9] Study Committee C1, Study Committee C2, and Working Group 18 of Study Committee C6, "Coping with limits for very high penetration of renewable energy," CIGRE, Tech. Rep., February 2013.

[10] A. El-Klhy and R. Iravani, "A review of the impacts of multiple wind power plants on large power systems dynamics," in *Electrical Power & Energy Conference (EPEC), 2013 IEEE*. IEEE, 2013, pp. 1–6.

[11] Y. Lei, A. Mullane, G. Lightbody, and R. Yacamini, "Modeling of the wind turbine with a doubly fed induction generator for grid integration studies," *Energy Conversion, IEEE Transactions on*, vol. 21, no. 1, pp. 257–264, 2006.

[12] J. Hu, H. Nian, H. Xu, and Y. He, "Dynamic modeling and improved control of DFIG under distorted grid voltage conditions," *Energy Conversion, IEEE Transactions on*, vol. 26, no. 1, pp. 163–175, 2011.

[13] H. Xu, J. Hu, and Y. He, "Integrated modeling and enhanced control of DFIG under unbalanced and distorted grid voltage conditions," *Energy Conversion, IEEE Transactions on*, vol. 27, no. 3, pp. 725–736, 2012.

[14] F. Wu, X.-P. Zhang, and P. Ju, "Small signal stability analysis and control of the wind turbine with the direct-drive permanent magnet generator integrated to the grid," *Electric Power Systems Research*, vol. 79, no. 12, pp. 1661–1667, 2009.

[15] A. Abedini and H. Nikkhajoei, "Dynamic model and control of a wind-turbine generator with energy storage," *Renewable Power Generation, IET*, vol. 5, no. 1, pp. 67–78, 2011.

[16] H. Huang, C. Mao, J. Lu, and D. Wang, "Small-signal modelling and analysis of wind turbine with direct drive permanent magnet synchronous generator connected to power grid," *Renewable Power Generation, IET*, vol. 6, no. 1, pp. 48–58, 2012.

[17] F. Wu, X.-P. Zhang, K. Godfrey, and P. Ju, "Modeling and control of wind turbine with doubly fed induction generator," in *Power Systems Conference and Exposition, 2006. PSCE'06. 2006 IEEE PES*. IEEE, 2006, pp. 1404–1409.

[18] F. Mei and B. C. Pal, "Modelling of doubly-fed induction generator for power system stability study," in *Power and Energy Society General Meeting-Conversion and Delivery of Electrical Energy in the 21st Century, 2008 IEEE*. IEEE, 2008, pp. 1–8.

[19] Z. Wu, W. Gao, D. Yang, and Y. Shi, "Comprehensive modeling and analysis of permanent magnet synchronous generator-wind turbine system with enhanced low voltage ride through capability," in *Energy Conversion Congress and Exposition (ECCE), 2012 IEEE*. IEEE, 2012, pp. 2091–2098.

[20] A. Mendonca and J. Lopes, "Impact of large scale wind power integration on small signal stability," in *Future Power Systems, 2005 International Conference on*. IEEE, 2005, pp. 5–pp.

[21] H.-W. Kim, S.-S. Kim, and H.-S. Ko, "Modeling and control of PMSG-based variable-speed wind turbine," *Electric Power Systems Research*, vol. 80, no. 1, pp. 46–52, 2010.

[22] P. Pourbeik, "WECC Type–3 wind turbine generator model – phase II," WECC, Tech. Rep., January 23, 2013. [Online]. Available: https://www.wecc.biz/Reliability/WECC%20Type%203%20Wind%20Turbine%20Generator%20Model%20-%20Phase%20II%20012313.pdf

[23] P. Pourbeik, "WECC Type–4 wind turbine generator model – phase II," WECC, Tech. Rep., January 23, 2013. [Online]. Available: https://www.wecc.biz/Reliability/WECC%20Type%204%20Wind%20Turbine%20Generator%20Model%20-%20Phase%20II%20012313.pdf

[24] K. Clark, N. W. Miller, and J. J. Sanchez-Gasca, "Modeling of GE wind turbine-generators for grid studies," *GE Energy*, vol. 4, 2010.

[25] A. Ellis, Y. Kazachkov, E. Muljadi, P. Pourbeik, and J. Sanchez-Gasca, "Description and technical specifications for generic WTG models — A status report," in *2011 IEEE/PES Power Systems Conference and Exposition*, 2011.

[26] A. Ellis, E. Muljadi, J. Sanchez-Gasca, and Y. Kazachkov, "Generic models for simulation of wind power plants in bulk system planning studies," in *Power and Energy Society General Meeting, 2011 IEEE*. IEEE, 2011, pp. 1–8.

[27] WECC Renewable Energy Modeling Task Force, "WECC wind power plant dynamic modeling guide," *Western Electricity Coordinating Council Modeling and Validation Work Group*, 2010. [Online]. Available: https://www.wecc.biz/Reliability/WECC%20Wind%20Plant%20Dynamic%20Modeling%20Guide.pdf

[28] PTI, *PSS®E 33.4, Program Application Guide —Volume 2*, Siemens Industry Inc., New York, March 2013.

[29] L. Yang, Z. Xu, J. Østergaard, Z. Y. Dong, K. P. Wong, and X. Ma, "Oscillatory stability and eigenvalue sensitivity analysis of a DFIG wind turbine system," *Energy Conversion, IEEE Transactions on*, vol. 26, no. 1, pp. 328–339, 2011.

[30] J. H. Chow, *Power System Coherency and Model Reduction*. Springer, 2013, ch. Introduction, pp. 1–14.

[31] B. Spalding, H. Yee, and D. Goudie, "Coherency recognition for transient stability studies using singular points," *Power Apparatus and Systems, IEEE Transactions on*, vol. 96, no. 4, pp. 1368–1375, 1977.

[32] R. Podmore, "Identification of coherent generators for dynamic equivalents," *IEEE Transactions on Power Apparatus and Systems*, vol. 4, no. PAS-97, pp. 1344–1354, 1978.

[33] B. Avramovic, P. V. Kokotovic, J. R. Winkelman, and J. H. Chow, "Area decomposition for electromechanical models of power systems," *Automatica*, vol. 16, no. 6, pp. 637–648, 1980.

[34] J. Winkelman, J. Chow, B. Bowler, B. Avramovic, and P. Kokotovic, "An analysis of interarea dynamics of multi-machine systems," *Power Apparatus and Systems, IEEE Transactions on*, no. 2, pp. 754–763, 1981.

[35] H. Kim, G. Jang, and K. Song, "Dynamic reduction of the large-scale power systems using relation factor," *Power Systems, IEEE Transactions on*, vol. 19, no. 3, pp. 1696–1699, 2004.

[36] K. Mei, S. M. Rovnyak, and C.-M. Ong, "Clustering-based dynamic event location using wide-area phasor measurements," *Power Systems, IEEE Transactions on*, vol. 23, no. 2, pp. 673–679, 2008.

[37] R. Singh, M. Elizondo, and S. Lu, "A review of dynamic generator reduction methods for transient stability studies," in *Power and Energy Society General Meeting, 2011 IEEE*. IEEE, 2011, pp. 1–8.

[38] A. M. Khalil and R. Iravani, "A dynamic coherency identification method based on frequency deviation signals," *Power Systems, IEEE Transactions on*, vol. PP, no. 99, pp. 1–9, 2015.

[39] R. Podmore, *Power System Coherency and Model Reduction*. Springer, 2013, ch. Coherency in Power Systems, p. 18.

[40] J. Slootweg and W. Kling, "The impact of large scale wind power generation on power system oscillations," *Electric Power Systems Research*, vol. 67, no. 1, pp. 9–20, 2003.

[41] E. Vittal, M. O. Malley, and A. Keane, "Rotor angle stability with high penetrations of wind generation," *Power Systems, IEEE Transactions on*, vol. 27, no. 1, pp. 353–362, 2012.

[42] M. H. Nguyen, T. K. Saha, and M. Eghbal, "Impact of high level of renewable energy penetration on inter-area oscillation," in *Universities Power Engineering Conference (AUPEC), 2011 21st Australasian*. IEEE, 2011, pp. 1–6.

[43] L. Fan, Z. Miao, and D. Osborn, "Impact of doubly fed wind turbine generation on inter-area oscillation damping," in *Power and Energy Society General Meeting-Conversion and Delivery of Electrical Energy in the 21st Century, 2008 IEEE*. IEEE, 2008, pp. 1–8.

[44] W. Qiao and R. G. Harley, "Effect of grid-connected DFIG wind turbines on power system transient stability," in *Power and Energy Society General Meeting-Conversion and Delivery of Electrical Energy in the 21st Century, 2008 IEEE*. IEEE, 2008, pp. 1–7.

[45] G. Tsourakis, B. Nomikos, and C. Vournas, "Effect of wind parks with doubly fed asynchronous generators on small-signal stability," *Electric Power Systems Research*, vol. 79, no. 1, pp. 190–200, 2009.

[46] L. Meegahapola and D. Flynn, "Impact on transient and frequency stability for a power system at very high wind penetration," in *Power and Energy Society General Meeting, 2010 IEEE*. IEEE, 2010, pp. 1–8.

[47] N. R. Chaudhuri and B. Chaudhuri, "Impact of wind penetration and HVDC upgrades on dynamic performance of future grids," in *Power and Energy Society General Meeting, 2011 IEEE*. IEEE, 2011, pp. 1–8.

[48] G. Tsourakis, B. M. Nomikos, and C. D. Vournas, "Contribution of doubly fed wind generators to oscillation damping," *Energy Conversion, IEEE Transactions on*, vol. 24, no. 3, pp. 783–791, 2009.

[49] F. Shewarega, I. Erlich, and J. L. Rueda, "Impact of large offshore wind farms on power system transient stability," in *Power Systems Conference and Exposition, 2009. PSCE'09. IEEE/PES*. IEEE, 2009, pp. 1–8.

[50] E. Hagstrøm, I. Norheim, and K. Uhlen, "Large-scale wind power integration in norway and impact on damping in the nordic grid," *Wind Energy*, vol. 8, no. 3, pp. 375–384, 2005.

[51] A. Mendonca and J. Lopes, "Impact of large scale wind power integration on small signal stability," in *Future Power Systems, 2005 International Conference on*. IEEE, 2005, pp. 5–pp.

[52] T. Knuppel, J. N. Nielsen, K. H. Jensen, A. Dixon, and J. Ostergaard, "Small-signal stability of wind power system with full-load converter interfaced wind turbines," *Renewable Power Generation, IET*, vol. 6, no. 2, pp. 79–91, 2012.

[53] L. Shi, S. Dai, Y. Ni, L. Yao, and M. Bazargan, "Transient stability of power systems with high penetration of DFIG based wind farms," in *Power & Energy Society General Meeting, 2009. PES'09. IEEE*. IEEE, 2009, pp. 1–6.

[54] Y. Mishra, S. Mishra, F. Li, Z. Y. Dong, and R. C. Bansal, "Small-signal stability analysis of a DFIG-based wind power system under different modes of operation," *Energy Conversion, IEEE Transactions on*, vol. 24, no. 4, pp. 972–982, 2009.

[55] C. Yu, G. James, Y. Xue, and F. Xue, "Impacts of large scale wind power on power system transient stability," in *Electric Utility Deregulation and Restructuring and Power Technologies (DRPT), 2011 4th International Conference on*. IEEE, 2011, pp. 277–283.

[56] N. R. Ullah and T. Thiringer, "Effect of operational modes of a wind farm on the transient stability of nearby generators and on power oscillations: a nordic grid study," *Wind Energy*, vol. 11, no. 1, pp. 63–73, 2008.

[57] D. Gautam and V. Vittal, "Impact of DFIG based wind turbine generators on transient and small signal stability of power systems," in *Power & Energy Society General Meeting, 2009. PES'09. IEEE*. IEEE, 2009, pp. 1–6.

[58] J. L. Rueda and I. Erlich, "Impacts of large scale integration of wind power on power system small-signal stability," in *Electric Utility Deregulation and Restructuring and Power Technologies (DRPT), 2011 4th International Conference on*. IEEE, 2011, pp. 673–681.

[59] E. Vittal and A. Keane, "Identification of critical wind farm locations for improved stability and system planning," *Power Systems, IEEE Transactions on*, vol. 28, no. 3, pp. 2950–2958, 2013.

[60] B. Pal and B. Chaudhuri, *Robust Control in Power Systems*. Springer, 2005, ch. Test System Model, pp. 39–44.

[61] P. L. Dandeno, P. S. Kundur, S. D. Umans, I. Kamwa, H. Karmaker, S. Salon, M. Shah, and A. El-Serafi, "IEEE guide for synchronous generator modeling practices and applications in power system stability analyses," *IEEE Std 1110-2002 (Revision of IEEE Std 1110-1991)*, pp. 1–72, 2003.

[62] P. W. Sauer and M. A. Pai, *Power System Dynamics and Stability.* Prentice-Hall, 1998.

[63] EnerNex Corporation, "Eastern wind integration and transmission study," The National Renewable Energy Laboratory, Tech. Rep., February 2011. [Online]. Available: http://www.nrel.gov/docs/fy11osti/47078.pdf

[64] S. G. Ghiocel and J. H. Chow, "Measurement-based voltage stability application: Methodology and experience," *CURENT*, January 2014. [Online]. Available: https://www.wecc.biz/_layouts/15/WopiFrame.aspx?sourcedoc=%2FReliability%2F2014_0118_Ghiocel_Chow_MeasurementBasedVoltageStability%2Epdf&action=view

[65] J. Qi, K. Sun, and W. Kang, "Optimal PMU placement for power system dynamic state estimation by using empirical observability gramian," *Power Systems, IEEE Transactions on*, vol. 30, no. 4, pp. 2041–2054, 2015.

[66] A. Ellis, Y. Kazachkov, J. Sanchez-Gasca, P. Pourbeik, E. Muljadi, M. Behnke, J. Fortmann, and S. Seman, *Wind Power in Power Systems, Second Edition.* John Wiley & Sons Ltd, 2012, ch. A Generic Wind Power Plant Model, pp. 799–801.

[67] W. Price and J. Sanchez-Gasca, "Simplified wind turbine generator aerodynamic models for transient stability studies," in *Power Systems Conference and Exposition, 2006. PSCE'06. 2006 IEEE PES.* IEEE, 2006, pp. 986–992.

[68] P. Kundur, J. Paserba, V. Ajjarapu, G. Andersson, A. Bose, C. Canizares, N. Hatziargyriou, D. Hill, A. Stankovic, C. Taylor *et al.*, "Definition and classification of power system stability IEEE/CIGRE joint task force on stability terms and definitions," *Power Systems, IEEE Transactions on*, vol. 19, no. 3, pp. 1387–1401, 2004.

[69] Synchrophasor Measurements for Power Systems Working Group, "IEEE standard for synchrophasor measurements for power systems," *IEEE Std C37.118.1-2011 (Revision of IEEE Std C37.118-2005)*, pp. 1–61, Dec 2011.